



저작자표시-비영리-변경금지 2.0 대한민국

이용자는 아래의 조건을 따르는 경우에 한하여 자유롭게

- 이 저작물을 복제, 배포, 전송, 전시, 공연 및 방송할 수 있습니다.

다음과 같은 조건을 따라야 합니다:



저작자표시. 귀하는 원저작자를 표시하여야 합니다.



비영리. 귀하는 이 저작물을 영리 목적으로 이용할 수 없습니다.



변경금지. 귀하는 이 저작물을 개작, 변형 또는 가공할 수 없습니다.

- 귀하는, 이 저작물의 재이용이나 배포의 경우, 이 저작물에 적용된 이용허락조건을 명확하게 나타내어야 합니다.
- 저작권자로부터 별도의 허가를 받으면 이러한 조건들은 적용되지 않습니다.

저작권법에 따른 이용자의 권리는 위의 내용에 의하여 영향을 받지 않습니다.

이것은 [이용허락규약\(Legal Code\)](#)을 이해하기 쉽게 요약한 것입니다.

[Disclaimer](#)

이학박사학위논문

**Local Circulations in
Mountainous Urban Areas**

산악 도시 지역의 국지 순환

2015년 2월

서울대학교 대학원

지구환경과학부

Gantuya Ganbat

Local Circulations in Mountainous Urban Areas

산악 도시 지역의 국지 순환

지도교수 백종진

이 논문을 이학박사 학위논문으로 제출함
2014년 10월

서울대학교 대학원
지구환경과학부
Gantuya Ganbat

Gantuya Ganbat의 이학박사 학위논문을 인준함
2014년 12월

위원장 _____ (인)

부위원장 _____ (인)

위원 _____ (인)

위원 _____ (인)

위원 _____ (인)

Local Circulations in Mountainous Urban Areas

By

Gantuya Ganbat

**A Dissertation Submitted to the Faculty of the
Graduate School of Seoul National University in
Partial Fulfillment of the Requirements for the
Degree of Doctor of Philosophy**

February 2015

Advisory Committee:

Professor Gyu-Ho Lim, Chair

Professor Jong-Jin Baik, Advisor

Professor Sang-Woo Kim

Professor Sang-Hyun Lee

Doctor Young-San Park

Abstract

Numerical modeling and theoretical approaches are applied to study local circulations in mountainous urban areas, the interactions of the local circulations, and the dependences of the local circulations to several factors. Also, the local circulations in the presence of temperature inversion, an important aspect for air pollution in mountainous urban areas, are studied.

Characteristics of urban heat island intensity in Ulaanbaatar city, Mongolia, are investigated for the first time using data for the 31-year period 1980-2010 from two meteorological stations, an urban and a rural site. The UHI intensity and maximum UHI intensity are studied. Daily, monthly, seasonal, and yearly characteristics of the UHI intensity are documented. The analysis shows that the UHI intensity exhibits a large seasonal dependence, being strongest in winter (nighttime), weakest in summer (daytime). The daily maximum UHI is found to be stronger in winter than in summer and frequently occurs in the nighttime. A multiple linear regression analysis is undertaken to examine the relative importance of various meteorological parameters (previous-day maximum UHI intensity, wind speed, cloudiness, and relative humidity) that affect the daily maximum UHI intensity. The previous-day maximum UHI intensity is the most important parameter and is positively correlated with the daily maximum UHI intensity.

The interactions of urban breeze circulation with mountain slope winds in two dimensions are investigated using the Weather Research and Forecasting (WRF) model coupled with the Seoul National University Urban Canopy Model (SNUUCM). A city is located near an isolated mountain, and there is no basic-state wind. Circulation over the urban area is asymmetric and characterized by the weakened mountain-side urban wind due to the opposing upslope wind and the strengthened plain-side urban wind in the daytime. The transition from upslope wind to downslope wind on the urban-side slope starts earlier than that on the mountain slope in a simulation only with an isolated mountain. A hydraulic jump occurs in the late afternoon when the strong downslope wind merges with weaker mountain-side urban wind and stagnates until the late evening. Sensitivities of the interactions of urban breeze circulation with mountain slope winds and the urban heat island intensity to the mountain height and urban fraction are examined. As the mountain height decreases and the urban fraction increases, the transition from the urban-side upslope wind to downslope wind starts earlier and the urban-side downslope wind persists longer. The change in transition time from the urban-side upslope wind to downslope wind results in changes in interactions between urban breeze circulation and mountain slope winds. The urban heat island intensity is more sensitive to the urban fraction than to the mountain height. An increase in urban fraction

by every 0.1 results in an average increase of 0.17°C (1.27°C) in the daytime (nighttime) urban heat island intensity. A simulation case in which a city is located in a basin is tested and the results show that the urban-side downslope wind develops earlier and persists longer and the plain-to-basin wind is stronger than in the simulation with a city and an isolated mountain.

The interactions of urban breeze circulation with mountain slope winds are investigated theoretically in the context of the response of the atmosphere to specified thermal forcing. Starting from linearized governing equations in two dimensions, analytical solutions for perturbation vertical velocity, horizontal velocity, buoyancy, and kinematic pressure are obtained. Then, the analytical solutions are used to examine the interactions. Urban breeze circulation and mountain slope winds are, respectively, evolved with time due to respective time-varying thermal forcing that has steady and diurnal components, and they linearly interact with each other. Asymmetric flows are developed over the urban and mountain areas. In the daytime, low-level converging flows induced by urban heating (urban breeze) and those induced by mountain heating (upslope winds) effectively interfere with each other, resulting in weakened flows over the mountain-side urban area and the urban-side mountain slope. The transition from upslope wind to downslope wind on the urban-side mountain slope occurs earlier and thus the downslope wind persists longer when compared with the case that has

mountain thermal forcing only. In the nighttime, flows become strong in the region between the urban center and the mountain center due to the additive interaction of the downslope wind with the urban breeze, but the flow intensity weakens with time because of weak nighttime urban heating. In the nighttime, the downslope wind on the rural-side mountain slope and converging flows on the plain-side urban area are weakened. Sensitivities of the interactions of urban breeze circulation with mountain slope winds on the intensities of urban and mountain thermal forcings are examined. Both in the daytime and nighttime, the degree of the interactions of urban breeze circulation with mountain slope winds are shown to depend on the intensities of urban and mountain thermal forcings.

The local circulations in and around the Ulaanbaatar, Mongolia, metropolitan area are examined numerically by using the WRF model coupled with the SNUUCM. Considering an idealized summertime fair-weather conditions with no synoptic winds, three-dimensional simulations are conducted. In the daytime, mountain upslope winds, up-valley winds, and urban breeze circulation appear and interact with each other. Mountain upslope winds precede up-valley winds. It is found that the transition of upslope winds to downslope winds on the urban-side slope of Mt. Bogd Khan occurs and the downslope winds in the afternoon strengthen due to urban breezes. In the nighttime, mountain downslope winds and down-

valley winds are prominent and strong channeling flows form over the city. The sensitivities of local circulations to urban fraction, atmospheric stability, and soil water content are examined. As urban fraction increases, daytime up-valley winds over the city and daytime downslope winds on the urban-side slope of Mt. Bogd Khan strengthen. Daytime near-surface up-valley winds in the city strengthen with increasing atmospheric stability. As soil water content decreases, daytime near-surface up-valley winds in the city weaken. The daytime urban atmospheric boundary-layer height is found to be sensitive to atmospheric stability and soil water content. This study is a first attempt to examine local circulations in and around the Ulaanbaatar metropolitan area and demonstrates that the city alters mountain slope winds and up-/down-valley winds.

The wintertime local circulations in and around the Ulaanbaatar area in the presence of temperature inversion are investigated through WRF-SNUUCM. The simulated air temperature and winds near the surface are validated against the observed one. A wintertime scenario with clear skies, weak synoptic winds, and temperature inversion under the influence of a Siberian high-pressure system is selected. It is found that the thickness and strength of temperature inversion layer are associated with the terrain. The temperature inversion layer is deeper and stronger in the valleys than over the mountain slopes, and its top height is typically lower than the maximum

ridge top height of the surrounding mountains but higher than the top of the boundary layer. Weak local circulations develop in the presence of temperature inversion. In the daytime, weak mountain upslope winds develop, up-valley winds appear to be stronger in the urban area than in the surrounding areas, and channeling winds are produced in the narrow valleys. The bottom of temperature inversion layer rises up in the urban area, and winds below the bottom of temperature inversion layer strengthen. In the nighttime, mountain downslope winds and down-valley winds develop with a lifted daytime residual layer. Urban effects in the presence of temperature inversion are examined by comparing simulation cases with and without the city. It is shown that in the daytime the urban area acts to elevate the bottom of temperature inversion layer and weaken the strength of temperature inversion layer. Compared to the simulation case without the city, the simulation case with the city shows that winds east of the city weaken in the afternoon and that down-valley winds develop later. These result from the interactions of urban breezes with valley winds.

Keywords: local circulation, urban heat island, urban breeze circulation, mountain slope winds, atmospheric modeling, urban canopy model, Ulaanbaatar, Mongolia

Student Number: 2010-30765

Contents

Abstract

Contents

List of Figures

List of Tables

1 Introduction	
1.1 Review of previous studies	1
1.1.1 Urban heat island.....	1
1.1.2 Urban breeze circulation.....	5
1.1.3 Local circulation over mountainous terrain.....	6
1.2 Objectives of this study	12
2 Characteristics of the Ulaanbaatar urban heat island	
2.1 Study area.....	15
2.2 Measurement sites and data	19
2.3 Data analysis	21
2.3.1 Characteristics of the temporal urban heat island.....	21

2.3.2	Characteristics of the daily maximum urban heat island intensity	27
2.3.3	Effects of meteorological parameters on the daily maximum urban heat island intensity	33
3	Interactions of urban breeze circulation with mountain slope winds: A numerical study	
3.1	Experimental design	39
3.2	Results and discussions	41
3.2.1	Urban breeze circulation and mountain slope winds	41
3.2.2	Interactions of urban breeze circulation with mountain slope winds	50
3.2.3	Sensitivity to mountain height and urban fraction	66
3.3	A city in a basin	78
4	Interactions of urban breeze circulation with mountain slope winds: A theoretical study	
4.1	Governing equations, solutions, and experimental settings	84
4.1.1	Governing equations and solutions	84
4.1.2	Parameter settings	91
4.2	Results and discussion	99
4.2.1	Urban breeze circulation and mountain slope winds	99

4.2.2 Interactions of urban breeze circulation with mountain slope winds	106
4.2.3 Sensitivities to thermal forcing intensities	111
5 Local circulations in the Ulaanbaatar area: Idealized simulations	
5.1 Experimental design	120
5.2 Results and discussions.....	125
5.2.1 Control simulation	125
5.2.2 Sensitivity experiments	137
6 Local circulations in the Ulaanbaatar area: A case study	153
6.1 Experimental design	153
6.2 Synoptic weather and model validation.....	154
6.3 Results and discussions.....	161
7 Summary and conclusions	

List of Figures

1.1. Urban heat island profile (from http://landsat.gsfc.nasa.gov).....	3
1.2. Diurnal mountain wind system (after Defant 1951).....	9
2.1. Locations of Ulaanbaatar and Buyant-Ukhaa stations that are marked by circle and triangle (also marked by circle and triangle (also marked in (b) and (c)), respectively, and topography. The topographic elevation is derived from the Shuttle Radar Topography Mission (SRTM) database with a spatial resolution of 90 m (Jarvis et al. 2008). The solid line indicates the Ulaanbaatar city boundary. Surroundings of (b) Ulaanbaatar and (c) Buyant-Ukhaa stations from Google Inc. (2011).....	17
2.2. Time series of (a) annually averaged daily mean temperature and (b) annually averaged daily minimum temperature at Ulaanbaatar and Buyant-Ukhaa stations.	18
2.3. (a) Monthly and (b) diurnal variations of the UHI intensity.....	23
2.4. Diurnal variation of the UHI intensity in each season.....	24
2.5. Time series of annually and seasonally averaged daily maximum UHI intensities.....	29
2.6. Histogram of the frequency distribution (in fraction) of the daily maximum UHI intensity as a function of the time of day in (a) spring, (b) summer, (c) autumn, and (d) winter.....	30

2.7.	Histogram of the frequency distribution (in fraction) of the daily maximum UHI intensity as a function of the time of day.	31
3.1.	Horizontal velocity (shading), vertical velocity (contour), and velocity vector fields at (a) 0900, (b) 1300, (c) 1900, and (d) 2300 LST and corresponding potential temperature anomaly field (shading) at (e) 0900, (f) 1300, (g) 1900, and (h) 2300 LST in the URBAN simulation. The gray box on the x -axis (also in Figs. 3.3, 3.4, 3.7, 3.8, 3.11) indicates the urban area. The contour levels of vertical velocity are 0.5, 1, and 2 m s ⁻¹	44
3.2.	Same as in Fig. 3.1 but for the MOUNT simulation. The contour levels of vertical velocity are 0.5 and 1 m s ⁻¹	48
3.3.	Horizontal velocity (shading), vertical velocity (contour), and velocity vector fields at (a) 1300, (b) 1500, (c) 1600, (d) 1900, and (e) 2300 LST and corresponding potential temperature anomaly field (shading) at (f) 1300, (g) 1500, (h) 1600, (i) 1900, and (j) 2300 LST in the URBAN-MOUNT simulation. The gray box on the x -axis indicates the urban area. The contour levels of vertical velocity are – 0.5 (dashed line, Fig. 3.3d), 0.5, 1, and 2 m s ⁻¹	52
3.4.	Distance-time section of horizontal wind at 10 m above the surface in the (a) URBAN, (b) MOUNT, and (c) URBAN-MOUNT simulations. The gray box on the x -axis indicates the urban area. The	

	mountain is located in the region from $x = 80$ to 100 km in (b) and (c). The contour intervals are 0.5 m s^{-1}	57
3.5.	Vertical profiles of potential temperature at $x = 110$ km and $t = 1600$ LST in the URBAN (dashed), MOUNT (dotted), and URBAN-MOUNT (solid) simulations.	59
3.6.	Horizontal velocity (shading), vertical velocity (contour), and velocity vector fields at 1500 LST in the simulations with maximum mountain heights of (a) 300, (b) 500, (c) 700, and (d) 900 m. The contour levels of vertical velocity are 0.5 and 1 m s^{-1}	63
3.7.	Same as in Fig. 3.6 but for the simulations with urban fractions of (a) 0.2, (b) 0.4, (c) 0.6, and (d) 0.8.	69
3.8.	Transition time from upslope wind to downslope wind (at 10 m above the slope) at the urban-side mid-slope location ($x = 95$ km), (b) percentage of the occurrence frequency of downslope wind (at 10 m above the slope) at the urban-side mid-slope location, and 10-m horizontal wind at (c) the mountain–urban edge ($x = 100$ km) and (d) the urban–rural edge ($x = 120$ km) as a function of maximum mountain height and urban fraction. (c) and (d) are averaged over the period 0800–2000 LST, and (b) is for the one-day period 0800–0800 LST. The contour intervals in (a), (b), (c), and (d) are 1 h, 2.5%, 0.2 m s^{-1} , and 0.2 m s^{-1} , respectively.	70

3.9. (a) Daytime (1200–1700 LST) and (b) nighttime (0000–0500 LST) averaged urban heat island intensities as a function of maximum mountain height and urban fraction.....	75
3.10. Horizontal velocity (shading), vertical velocity (contour), and velocity vector fields at (a) 1200, (b) 1500, (c) 1600, (d) 1900, and (e) 2300 LST in the BASIN simulation. The gray box on the x -axis indicates the urban area. The contour levels of vertical velocity are -0.5 (dashed line, Fig. 3.10d), 0.5 , 1 , and 2 m s^{-1}	81
4.1. Temporal variations of urban thermal forcing at $x = c_u$ and $z = 0 \text{ km}$ (solid line) and mountain thermal forcing at $x = c_m$ and $z = 0 \text{ km}$ (dashed line).....	95
4.2. Kinematic pressure (gray dashed contour), buoyancy (shaded), vertical velocity (black contour), and velocity vector fields at (a) and (f) 0200, (b) and (g) 0800, (c) and (h) 1400, (d) and (i) 1700, and (e) and (j) 2000 LT in the URBAN (left) and MOUNT (right) cases. The dark gray (gray) box on the x -axis (also, in Figs. 4.4–4.6) indicates the urban (mountain) area.....	97
4.3. Temporal variations of (a) the maximum horizontal velocity in the entire domain and w_m in (b) $0 \text{ km} \leq x \leq 20 \text{ km}$ and (c) $-20 \text{ km} \leq x \leq 0 \text{ km}$ in the URBAN (short-dashed lines), MOUNT (dashed lines), URBAN-MOUNT (solid lines) cases.....	102

4.4.	Distance-time sections of the horizontal velocity (shaded) at the surface and the vertical velocity (solid and dashed lines) at $z = 200$ m in the (a) URBAN, (b) MOUNT, and (c) URBAN-MOUNT cases. Dashed lines indicate the negative vertical velocity. Bold solid and dashed-short dashed lines indicate the zero vertical and horizontal velocity, respectively.	105
4.5.	Kinematic pressure (gray lines), buoyancy (shaded), vertical velocity (black lines), and velocity vector fields at (a) 0200, (b) 0800, (c) 1100, (d) 1400, (e) 1700, and (f) 2000 LT in the URBAN-MOUNT case.	108
4.6.	Kinematic pressure (gray lines), buoyancy (shaded), vertical velocity (black lines), and velocity vector fields at (a)–(d) 0200 and (e)–(h) 1700 LT in the URBAN+ (a and e), URBAN– (b and f), MOUNT+ (c and g), and MOUNT– (d and h) cases.	114
4.7.	Maximum intensities of the horizontal velocity (m s^{-1}) at the (a) mountain–urban edge and (b) urban–rural edge, (c) the transition time (LT) from the upslope wind to downslope wind, and (d) the percentage of the occurrence frequency of downslope wind during the 24-h period as a function of the ratios of thermal forcing magnitudes. (c) and (d) are at the urban-side mid-slope location. The dotted area in (c) indicates that the upslope wind does not occur. The	

dotted area in (d) indicates 100% of the frequency of downslope wind.....	119
5.1. Terrain height of the (a) domain and (b) analysis area. The inner rectangle in (a) is the analysis domain. The gray lines indicate the Ulaanbaatar city boundary. The dotted boxes in (a) indicate the rural areas.....	123
5.2. Diurnal variations of (a) surface sensible heat flux, (b) surface latent heat flux, (c) air temperature at 2 m, and (d) atmospheric boundary-layer height averaged over the urban and rural areas in the control simulation.....	127
5.3. Fields of air temperature at 2 m and wind vector at 10 m at (a) 0300, (b) 0600, (c) 0900, (d) 1200, (e) 1600, and (f) 2100 LST in the control simulation. The dark gray line indicates the urban boundary. Light gray lines indicate the terrain height (from 1300 to 2100 m with intervals of 200 m).....	131
5.4. Vertical cross-sections of wind vector and vertical velocity (contours) along the south-north direction through the center of the analysis domain at (a) 0300, (b) 0600, (c) 0900, (d) 1200, (e) 1600, and (f) 2100 LST in the control simulation. The contour levels of vertical velocity are 0.5 and 1 m s ⁻¹ . The dark gray bar on the horizontal axis indicates the urban area.....	132

5.5.	Same as in Fig. 5.4 but for the east-west direction. The contour levels of vertical velocity are 0.5, 1, and 2 m s ⁻¹	134
5.6.	Diurnal variations of (a) surface sensible heat flux, (b) surface latent heat flux, (c) air temperature at 2 m, and (d) atmospheric boundary-layer height averaged over the urban area in the UF05 (dashed), UF07 (solid), and UF09 (dot-dashed) simulations.....	138
5.7.	Fields of air temperature at 2 m and wind vector at 10 m in the (a) UF05 and (b) UF09 simulations and the vertical cross-sections of wind vector and vertical velocity (contours) along the south-north direction through the center of the analysis domain in the (e) UF05 and (f) UF09 simulations at 1600 LST. The dark gray line in (a) and (b) indicates the urban boundary. Light gray contours in (a) and (b) indicate the terrain height (from 1300 to 2100 m with intervals of 200 m). The dark gray bar on the horizontal axis in (c)–(f) indicates the urban area. The contour levels of vertical velocity in (c)–(f) are 0.5 and 1 m s ⁻¹	141
5.8.	Same as in Fig. 5.6 but for the AS4 (dashed), AS5 (solid), and AS6 (dot-dashed) simulations.....	144
5.9.	Figure 5.9. Same as in Fig. 5.7 but for the AS4 and AS6 simulations. The contour levels of vertical velocity in (c)–(f) are 0.5, 1, and 2 m s ⁻¹	145

5.10. Same as in Fig. 5.6 but for the SW009 and SW025 simulations. . .	149
5.11. Same as in Fig. 5.7 but for the SW009 and SW025 simulations. The contour levels of vertical velocity in (c)–(f) are 0.5, 1, and 2 m s ⁻¹	150
6.1. Terrain height in the (a) five computational domains and (b) innermost domain. The white rectangle in (b) indicates the analysis area. 26 meteorological stations are indicated by the black dots in (a). The urban boundary is indicated by the gray line in (b).....	156
6.2. (a) Surface and (b) 850 hPa weather maps at 0000 UTC (0800 LST) 19 December 2013. Ulaanbaatar is indicated by the blue circle. (after courtesy of the Korea Meteorological Administration.).....	158
6.3. Diurnal variations of observed and simulated (a) 2-m temperature, (b) 10-m wind speed, (c) 10-m wind direction, and (d) scatterplot of 2-m temperatures observed at 26 meteorological stations and simulated. Observations are made at 3-h intervals.....	159
6.4. Skew T -log p diagrams at Ulaanbaatar station for observations (black) and simulations (red) valid at (a) 0800 and (b) 2000 LST 19 December 2013.....	160
6.5. Diurnal variations of (a) surface sensible heat flux, (b) surface latent heat flux, (c) 2-m temperature, and (d) boundary layer height averaged over the urban area.....	162

6.6.	Fields of the thickness (left) and strength (right) of temperature inversion layer at (a), (e) 0300, (b), (f) 1000, (c), (g) 1400, and (d), (h) 2000 LST. The light gray lines (also in Figs. 6.8, 6.11, 6.12) indicate terrain height contours (from 1400 to 2200 m with intervals of 200 m). The urban boundary is indicated by the dark gray line (also in Figs. 6.8, 6.11, 6.12). The area without no inversion layer is shaded in white color (also in Fig. 6.10).....	164
6.7.	Diurnal variations of (a) top and bottom heights of temperature inversion layer, (b) its strength, and (c) temperatures at the inversion top and bottom averaged over the urban area.	165
6.8.	Fields of 2-m temperature and 10-m wind vector at (a) 0300, (b) 0800, (c) 1000, (d) 1400, (e) 1800, and (f) 2000 LST.....	168
6.9.	Vertical cross-sections of temperature and wind vector along the north-south direction at $x = 0$ km at (a) 0300, (b) 0800, (c) 1000, (d) 1400, (e) 1800, and (f) 2000 LST. The gray boxes on the horizontal axis indicate the urban area, and pink lines indicate the boundary where the vertical temperature gradient changes its sign (also in Fig. 6.10).....	169
6.10.	Vertical cross-sections of temperature and wind vector along the east-west direction at $y = 0$ km at (a) 0300, (b) 0800, (c) 1000, (d) 1400, (e) 1800, and (f) 2000 LST.....	170

6.11. (a) Thickness and (b) strength of inversion layer at 1400 LST in the no-urban simulation.....	174
6.12. Same as in Fig. 6.8 but for the simulation with the urban area being replaced by the grassland land-use type.	175

List of Tables

2.1. Normalized regression coefficients of the four meteorological parameters (PER, maximum UHI intensity for the previous day; WS, wind speed; CL, cloudiness; RH, relative humidity). r^2 is the percentage of the total variance explained by the regression model, and n is the sample size.	36
4.1. Names and thermal forcing magnitudes for eight cases (unit: $\text{J kg}^{-1} \text{s}^{-1}$)	96

1 Introduction

1.1 Review of previous studies

1.1.1 Urban heat island

The near-surface air temperature can be higher in an urban area than in its surrounding rural areas. This phenomenon is known as the urban heat island (UHI). Figure 1.1 illustrates the typical horizontal temperature distribution. The causative factors and their relative importance for the UHI are well known. These include anthropogenic heat, impervious surfaces, and three-dimensional urban geometry (Ryu and Baik 2012). Anthropogenic heat is an important causative factor, especially in the nighttime (Fan and Sailor 2005). Artificial surfaces such as paved roads and buildings lead to a surface energy balance different from the surface energy balance for natural rural surfaces (Oke 1982; Taha 1997). Owing to the high heat storage capacity of urban surfaces and the low surface moisture availability of less vegetated urban surfaces, the sensible heat flux is larger and the latent heat flux is smaller in urban areas than in rural areas.

A number of studies have investigated the relationships between meteorological parameters/weather conditions and UHI intensity (e.g.,

Unger 1996; Kim and Baik 2002; Hinkel et al. 2003; Lee and Baik 2010). It
is a fact

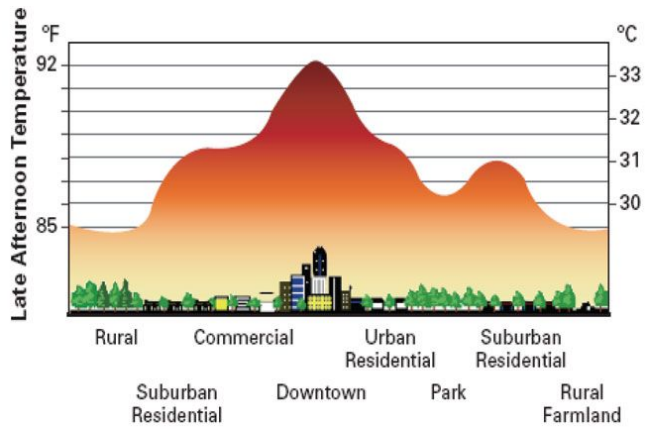


Figure 1.1. Urban heat island profile (from <http://landsat.gsfc.nasa.gov>).

that an ideal meteorological condition for UHI development is a stable, calm, and clear sky condition (Oke 1982). Under clear nighttime skies, rural surfaces tend to cool off faster than urban surfaces. Clouds and strong winds reduce the UHI intensity (Figuerola and Mazzeo 1998; Morris et al. 2001).

It is well known that the UHI intensity depends on the time of day and the season. The UHI intensity is stronger in the nighttime than in the daytime (e.g., Magee et al. 1999; Liu et al. 2007). In many cities around the world, the strong UHI intensity appears frequently in winter (e.g., Jauregui et al. 1992; Figuerola and Mazzeo 1998; Montávez et al. 2000; Kim and Baik 2002; Liu et al. 2007). For example, in Fairbanks, Alaska, USA, stronger UHIs occurred in winter than in other seasons under calm and clear sky conditions (Magee et al. 1999).

The near-surface air temperature in urban areas is at times or often can be lower than that of surrounding rural areas. This phenomenon is called the urban cool island. Granada, Spain, often experiences a lower air temperature in the urban area than in its surroundings, and the city's urban cool island intensity was reported to reach up to 2°C (Montávez et al. 2000). Kim and Baik (2004) reported daytime urban cool islands in Seoul, South Korea.

1.1.2 Urban breeze circulation

Many interesting thermally-induced wind systems occur locally, including sea/land breezes, mountain/valley winds (or downslope/upslope winds), lake breezes, and urban breezes. Of these local wind systems, sea/land breezes, mountain/valley winds, and lake breezes have been investigated extensively through observational, theoretical, and numerical modeling studies (e.g., Simpson 1994; Pielke 2002). Urban breezes are interesting phenomenon and worthwhile to investigate as they play important roles in local weather and air quality.

Urban breeze circulation (also known as urban heat island circulation) is induced by the difference in near-surface air temperature between the urban area and its surrounding rural area, that is, the urban heat island. Combined circulations, which consist of inward flow toward the city center in the lower boundary layer, upward motion near the city center, outward flow toward the surrounding rural area in the upper boundary layer, and weak downward motion outside, characterize the urban breeze circulation. Urban breeze circulation is stronger in the daytime than in the nighttime related with atmospheric stability. Urban breeze circulation has been observed in many cities (e.g., Wong and Dirks 1978; Hidalgo et al. 2008b) and the numerical simulations enable to investigate it in depth (Lemonsu and Masson 2002; Hidalgo et al. 2008a; Ryu and Baik 2013a).

Based on temperature and wind measurements over St. Louis area, it was shown that winds were converged into the elevated heat island under undisturbed weather conditions (Wong and Dirks 1978). The boundary layer simulated over the Paris area in France was deeper in the daytime than in the nighttime, with converging (diverging) flow of $5\text{--}7\text{ m s}^{-1}$ at lower (upper) levels and upward vertical velocities of $\sim 1\text{ m s}^{-1}$ (Lemonsu and Masson 2002). Also, numerical investigations of the local circulations in the Seoul, Korea, metropolitan area by Ryu and Baik (2013a) showed that the convergence zone and upward motion are developed over the urban area in the daytime associated with the urban breeze circulation effectively interacts with other local circulations, such as sea-breeze, cross-valley, and river-breeze circulations.

1.1.3 Local circulation over mountainous terrain

Over uneven mountainous terrain, from small hills to large mountain ranges, two types of diurnal winds that are generated by pressure gradient due to differential heating are generally developed – slope and valley winds (Whiteman 1990). Other winds, such as plain-to-basin wind and tributary flows, related to complex terrain can be present over mountain ranges. A well-known schematic model of a diurnal mountain wind system is defined by Defant (1951), which is illustrated in Fig. 1.2. After sunrise, upslope

winds develop over mountain slopes while valley winds blow down along the valley axis (Fig. 1.2a). Later, down-valley wind ceases reversing to up-valley direction and upslope winds continue to accelerate (Figs. 1.2b,c). In the afternoon, when solar radiation decreases, upslope winds cease (Fig. 1.2d) and turn downslope (Fig. 1.2e). After sunset, up-valley wind ceases (Fig. 1.2f) and transits back to down-valley direction (Fig. 1.2g). Down-valley winds exist late at night until morning (Fig. 1.2h).

When a city is located near mountainous area, both the urban breeze and upslope/downslope winds are thermally induced and can interact with each other. Previous numerical modeling studies have investigated alteration in local circulations in the presence of urban areas and topography or interactions between the urban breeze and upslope/downslope winds (e.g., Ohashi and Kida 2002; Lee and Kim 2010; Ryu and Baik 2013a; Giovannini et al. 2014). It was demonstrated that the urban breeze circulation alters the upslope/downslope winds counteracting the mountain upslope winds in the daytime and enhancing downslope winds in the nighttime. Lee and Kim (2010) performed idealized two-dimensional simulations and showed that the urban sensible heat flux acts to accelerate nocturnal drainage flow, which tends to increase the return flow above. Ryu and Baik (2013a) simulated local circulations in the Seoul metropolitan area in South Korea and demonstrated that the upslope wind turns to downslope

wind and the downslope wind strengthens with gradual strengthening of the urban breeze circulation in the

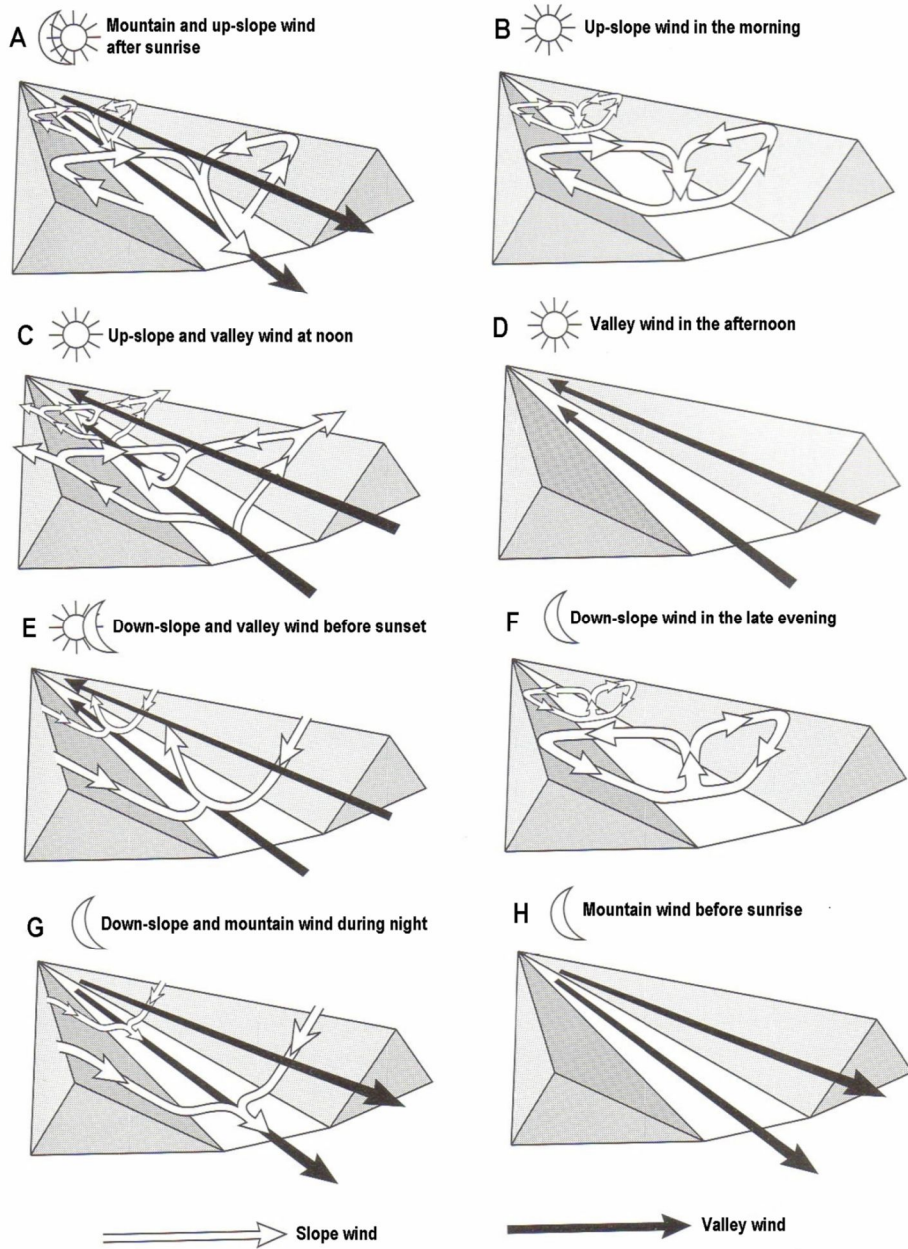


Figure 1.2. Diurnal mountain wind system (after Defant 1951).

daytime. Giovannini et al. (2014) examined boundary-layer processes and urban-induced alterations in an Alpine valley and showed that valley winds are effectively altered due to the presence of Trento city, Italy. These modeling studies provide valuable insights into interactions between urban breeze circulation and upslope/downslope winds.

A number of theoretical investigations are focused on the thermally forced urban breeze circulation or the mountain slope winds (e.g., Olfe and Lee 1971; Lin and Smith 1986; Baik 1992; Han and Baik 2008; Kirshbaum 2013). In the theoretical studies, the urban heat island, which is represented by a time-independent surface or low-level heat source, induces flows/circulation. Flows/circulation induced by thermal forcing over flat terrain, which were conceptually represented an isolated mountain-like heat source, were studied in linear, theoretical system (Kirshbaum 2013). However, study on the interactions between urban breeze circulation and mountain slope winds has not been theoretically attempted yet.

Many factors, including urban fraction and urban surface roughness, affect the intensity of urban breeze circulation, and mountain shape and height influence upslope/downslope winds. Also, environmental (e.g., atmospheric boundary-layer stability) and land-surface (e.g., soil water content) parameters are important factors to the development of the local circulations. The stability of the atmospheric boundary layer greatly affects

the urban heat island circulation (e.g., Vukovich and Dunn 1978; Richiardone and Brusasca 1989; Baik et al. 2007). Baik et al. (2007) numerically and theoretically investigated the effects of atmospheric boundary-layer stability on the urban heat island circulation, showing that the boundary-layer flow becomes strong as atmospheric boundary-layer stability decreases. Through idealized numerical simulations, Martilli (2003) showed that the daytime urban atmospheric boundary layer is very sensitive to rural soil water content. Thus, the degree of interactions between urban breeze circulation and upslope/downslope winds depends on several factors.

Ulaanbaatar, the capital city of Mongolia, with a population of 1.1 million (at the end of 2009) is located at an altitude of about 1350 m. Topography in the Ulaanbaatar area is complex. Ulaanbaatar lies in a nearly east-west oriented valley between the southern base of branches of the Khentiin Nuruu mountain range (with a maximum height of approximately 2800 m) and the northern base of Mt. Bogd Khan (with a maximum height of approximately 2200 m). The valley terrain height decreases from east (valley mouth) to west (valley exit). The valley exit is connected to a wide basin. Several tributaries join in the valley. Thus, if a favorable condition is met, several local circulations can develop in and around Ulaanbaatar and they can interact with each other in a complex way. In wintertime, Ulaanbaatar is frequently governed by a Siberian high pressure with

corresponding temperature inversion which leads to a stagnation of air pollutants in the valley. Thus, the local circulations in and around the Ulaanbaatar metropolitan area under favorable or temperature inversion conditions and the interactions of the local circulations need to be investigated.

1.2 Objectives of this study

The characteristics of urban heat islands (UHI) in Ulaanbaatar, Mongolia, are investigated using the data from two meteorological stations. Temporal patterns of the UHI intensity including daily, monthly, and yearly UHI intensities are studied. Daily maximum UHI intensity is investigated. Multiple linear regression analysis is undertaken to examine the relative importance of meteorological parameters that affect the UHI intensity. The meteorological parameters include previous-day maximum UHI intensity, wind speed, cloudiness, and relative humidity (Section 2).

Interactions of urban breeze circulation with mountain slope winds in an idealized two-dimensional environment are investigated using a WRF model coupled with an advanced urban canopy model (WRF-SNUUCM). Temporal and spatial patterns are introduced. Results from simulations of circulations developed over a city, mountain, and a city near an isolated mountain area are compared. Sensitivities of the interactions of urban breeze

circulation with mountain slope winds and the UHI intensity to the urban fraction and mountain height are examined. A simulation case in which a city is located in a basin is investigated (Section 3).

To understand the interactions of urban breeze circulation with mountain slope winds, theoretical investigations are performed in the context of the atmosphere to specified thermal forcing. Analytical solutions are obtained from linearized governing equations in two dimensions and used to investigate the interactions. The dependencies of the interactions of urban breeze circulation with mountain slope winds on the intensities of urban and mountain thermal forcings are examined (Section 4).

The first attempt on investigations of the local circulations in and around the Ulaanbaatar metropolitan area is done using three-dimensional idealized simulations with real topography and land-use data using the WRF-SNUUCM. For the purpose, topography and land use dataset are prepared with fine resolution and accurate representation for the simulations. The diurnal variations of the local circulations are revealed. Sensitivities of the local circulations to urban fraction, atmospheric stability, and soil water content are examined (Section 5).

Based on the understanding of the local circulations in and around the Ulaanbaatar metropolitan area, the wintertime local circulations in the presence of temperature inversion are investigated numerically using the

real-data simulations. Urban effects in the presence of temperature inversion on the local circulations are examined (Section 6).

2 Characteristics of the Ulaanbaatar urban heat island

The characteristics of the urban heat island (UHI) in a high-altitude city, Ulaanbaatar, the capital of Mongolia, are investigated in this section. The study is motivated by the absence of research on the Ulaanbaatar UHI. The study area is characterized by unique geographical features and weather conditions.

2.1 Study area

A topography of Ulaanbaatar area is very complex. The city is located in a northern valley of the Bogd Khan mountain which is the southernmost limit of the Khentiin Nuruu mountain range (Fig. 2.1a). The highest peak of the Bogd Khan mountain reaches as much as around 2210 m above the valley floor of nearly 1300 m ASL. The northern slopes of the mountains are covered by evergreen coniferous forest and the southern slopes by bare rocks. The valley axis is oriented in the east-west direction, and its topography favors a channeling of easterly or westerly winds with complex terrain, such as bends in the valley, ridgelines due to tributaries, and high-lying alpine plateaus that are part of the surrounding mountains.

The area belongs to a cold semi-arid climate (Bsk) according to the Köppen-Geiger climate classification (Kottek



Figure 2.1. Locations of Ulaanbaatar and Buyant-Ukhaa stations that are marked by circle and tri-angle (also marked by circle and triangle (also marked in (b) and (c)), respectively, and topography. The topographic elevation is derived from the Shuttle Radar Topography Mission (SRTM) database with a spatial resolution of 90 m (Jarvis et al. 2008). The solid line indicates the Ulaanbaatar city boundary. Surroundings of (b) Ulaanbaatar and (c) Buyant-Ukhaa stations from Google Inc. (2011).

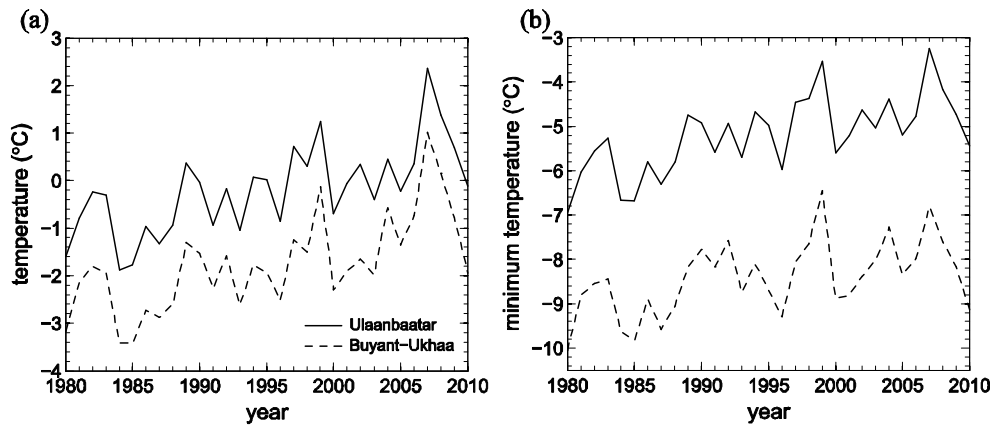


Figure 2.2. Time series of (a) annually averaged daily mean temperature and (b) annually averaged daily minimum temperature at Ulaanbaatar and Buyant-Ukhaa stations.

et al. 2006). Ulaanbaatar is known as the coldest capital city in the world because of its geographic features such as high altitude and landlocked location and the effects of wintertime Siberian high. Spring is dry and windy; summer is short; and winter is long and cold. The monthly average temperature for each month from October to March is below 0°C, and the average temperature in winter is -19°C. The annual precipitation amount is about 270 mm, and most precipitation occurs in summer. The population of Ulaanbaatar reached 0.8 (at the end of 1999) and 1.1 million (at the end of 2009), constituting 32% and 41% of the total population of Mongolia, respectively, and the increase is mostly because of rural-to-urban migration. And this proportion continues to grow. The city area has almost doubled since 1974 (Amarsaikhan et al. 2009).

2.2 Measurement sites and data

Ulaanbaatar station (Fig. 2.1b), located in a residential area that consists of ger-houses (traditional living houses known as yurts) and apartment buildings, represents an urban station. The station is located on a south-facing slope of the hill which lies in a narrow east-west directed valley region and is surrounded by up to 9-floor apartment buildings from the southern and dense ger-houses from the other sides. Ground surface is mostly paved or consists of soil with sparse grassland. Heating in apartment

buildings is distributed from central power station while ger-houses are heated by individual stoves which use coal and wood. Pollutant sources take place in every ger-houses. Buyant-Ukhaa airport station (Fig. 2.1c), located to the southwest of the city, represents a rural station. The station is located in a relatively flat and open terrain at the exit of the valley. The ground surface type at the station is grassland. The station is located ~100 m from the aerodrome runway. Paved surface and buildings are located at least ~500 m away from the station. The Ulaanbaatar and Buyant-Ukhaa airport stations are chosen for the analysis of the characteristics of the urban heat island in this study because the other urban station has a gap in the measurement period and the other meteorological stations/posts outside the city have short data records.

The distance between Ulaanbaatar station and Buyant-Ukhaa station is 10 km. Figures 2.1b and 2.1c show the surroundings of Ulaanbaatar and Buyant-Ukhaa stations, respectively. The altitudes of Ulaanbaatar and Buyant-Ukhaa stations are 1306 and 1286 m, respectively. The altitude difference between the two stations is very small. Thus, the altitude difference would have very little influence on the difference in air temperature between the two stations.

Data recorded in 3-h intervals from 1980 to 2010 are used in this study. Data are obtained from the State Archive and Database Center of the

National Agency for Meteorology and Environmental Monitoring (NAMEM), Mongolia. Only 85% of the original data are used for UHI analysis; the rest of the original data (15%) are not used because of missing data and/or poor decoding.

2.3 Data analysis

2.3.1 Characteristics of the temporal urban heat island

The UHI intensity is defined as the difference in air temperature between Ulaanbaatar and Buyant-Ukhaa stations. Time series of annually averaged daily mean temperature at Ulaanbaatar (urban) and Buyant-Ukhaa (rural) stations are shown in Fig. 2.2a. Both time series exhibit a similar fluctuation pattern with an increasing temperature trend. It is clearly seen that the annually averaged daily mean temperature at Ulaanbaatar station is higher than that at Buyant-Ukhaa station. The difference in annually averaged daily mean temperature between the two stations, that is, the average UHI intensity, is 1.6°C for the period of 1980–2010. Figure 2.2b depicts the time series of annually averaged daily minimum temperature at the two stations. The difference in annually averaged daily minimum temperature between the two stations is 3.2°C for the period of 1980–2010.

The linear increasing trend of the annually averaged daily minimum temperature at Ulaanbaatar station

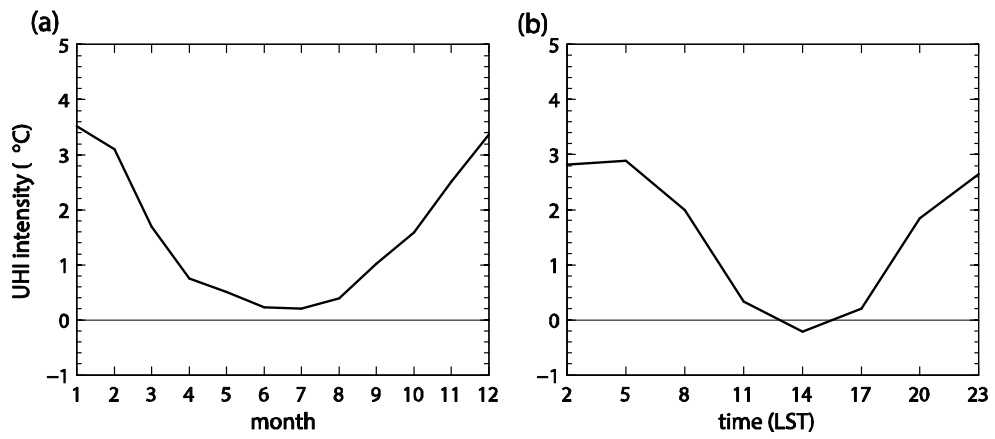


Figure 2.3. (a) Monthly and (b) diurnal variations of the UHI intensity.

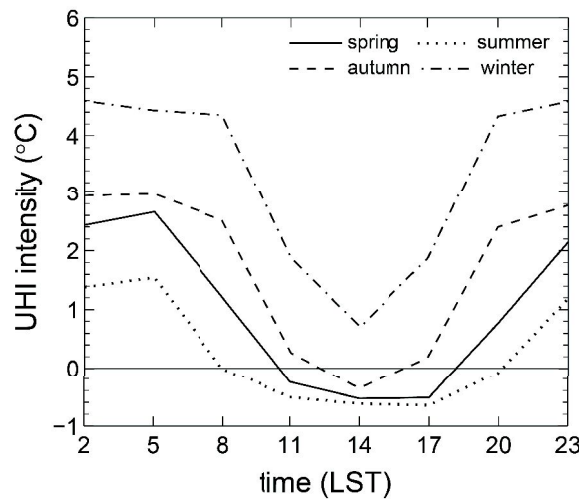


Figure 2.4. Diurnal variation of the UHI intensity in each season.

(0.6°C per decade) is larger than that at Buyant-Ukhaa station (0.5°C per decade). That is, the annually averaged daily minimum temperature has increased more at the urban station than at the rural station. The time series of annually averaged daily maximum temperature at Ulaanbaatar and Buyant-Ukhaa stations were also examined. The annually averaged daily maximum temperature at Ulaanbaatar station is similar to that at Buyant-Ukhaa station in its magnitude and its fluctuation pattern with an increasing temperature trend. The results indicate that the difference in daily minimum temperature between the urban and rural stations is pronounced compared to that in daily maximum temperature. Figure 2.3a shows the monthly variation of the UHI intensity. The UHI intensity is strongest in winter (3.3°C) and weakest in summer (0.3°C). The UHI intensity in winter in Ulaanbaatar is stronger than that (2.2°C) in Barrow, Alaska, USA (Hinkel et al. 2003). As pointed out by Goldreich (1984), the stronger UHI intensity is expected in high-altitude cities owing to inevitable space heating demand under cold conditions.

The diurnal variation of the UHI intensity is depicted in Fig. 2.3b. The UHI intensity is stronger in the nighttime than in the daytime. This is a typical feature observed in cities (e.g., Magee et al. 1999). The UHI intensity is shown to be strongest at 0500 LST (2.9°C). Note that in this study the data at 0200, 0500, 2000, and 2300 LST are used as nighttime data

and the data at 0800, 1100, 1400, and 1700 LST are used as daytime data. Around 1400 LST, the temperature at the urban station is lower by 0.2°C than that at the rural station. In other words, the urban cool island appears. However, the urban cool island intensity is weak.

The air temperature in urban areas can be lower than that in surroundings. One of the possible reasons for the lower temperature in urban areas is the large thermal inertia of urban surface materials. Because of the large thermal inertia, urban surface materials store a large amount of heat and hence urban areas can warm up more slowly than rural areas do, resulting in a lower temperature in urban areas (Oke 1987; Giovannini et al. 2011). This can lead to the urban cool island.

Figure 2.4 shows the diurnal variation of the UHI intensity in each season. The average UHI intensity is strongest in winter and weakest in summer throughout a whole day. The average UHI intensity is 1°C in spring, 0.3°C in summer, 1.7°C in autumn, and 3.3°C in winter. In the daytime, the urban cool island occurs more frequently for more extended times with stronger intensity in summer than in spring and autumn. The average intensity of the urban cool island in summer is 0.4°C . Similarly, the urban cool island with an average intensity of 0.6°C occurred in summer in Birmingham, U.K. (Unwin 1980).

In each season, the UHI is stronger in the nighttime than in the daytime. According to Ryu and Baik (2012), in the nighttime anthropogenic heat contributes greatly to the UHI intensity. In the nighttime, coal and wood burning in the traditional ger-houses for heating and cooking purposes likely contributes to increasing temperature in the urban area, especially in cold months.

2.3.2 Characteristics of the daily maximum urban heat island intensity

Figure 2.5 shows the time series of annually and seasonally averaged daily maximum UHI intensities. The annually averaged daily maximum UHI intensity exhibits an increasing trend for the period of 1980–2010. The increasing trend seems closely related to urbanization. Such an increasing trend in daily maximum UHI intensity was also observed in the six largest cities of South Korea (Kim and Baik 2004) but with different rates because of the differences in the degree of urbanization and local geographical features. The average daily maximum UHI intensity for the period of 1980–2010 is 4.3°C, 2.7 times the average UHI intensity for the same period (1.6°C). The strongest daily maximum UHI intensity occurs in winter with an average intensity of 6.4°C, and the weakest daily maximum UHI

intensity occurs in summer with an average intensity of 2.5°C. The average daily maximum UHI intensity is 3.8°C in spring and 4.5°C in autumn. The

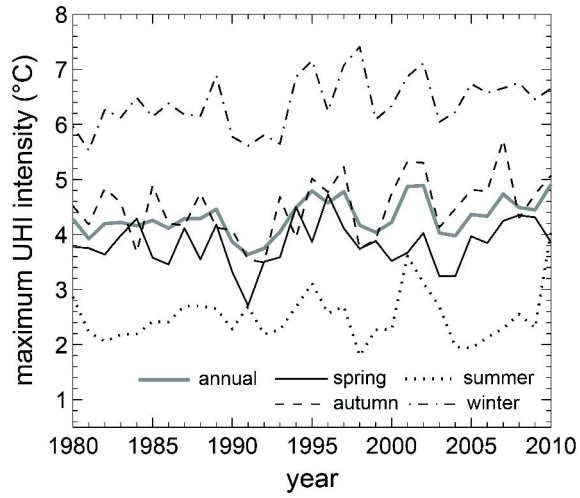


Figure 2.5. Time series of annually and seasonally averaged daily maximum UHI intensities.

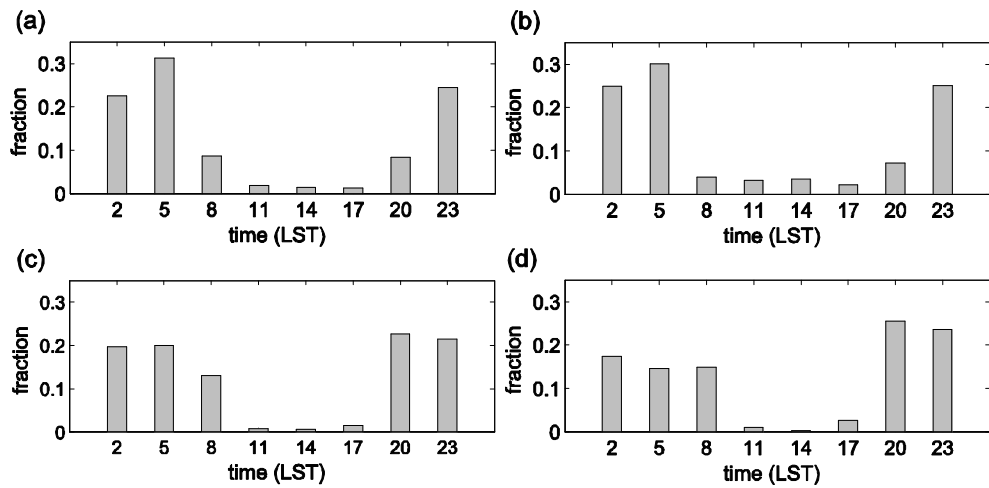


Figure 2.6. Histogram of the frequency distribution (in fraction) of the daily maximum UHI intensity as a function of the time of day in (a) spring, (b) summer, (c) autumn, and (d) winter.

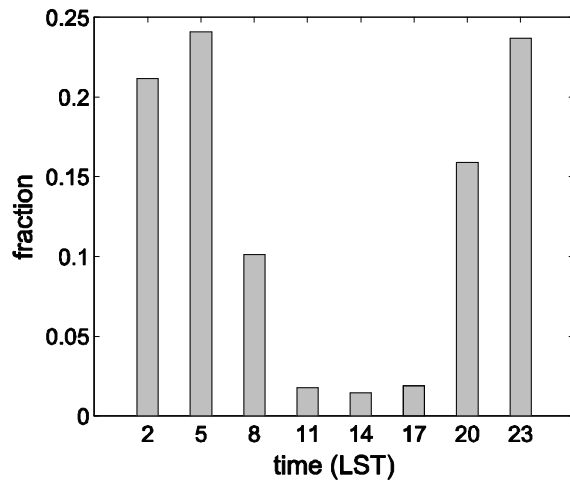


Figure 2.7. Histogram of the frequency distribution (in fraction) of the daily maximum UHI intensity as a function of the time of day.

increasing rate of the daily maximum UHI intensity is larger in autumn and winter than in spring and summer.

Figure 2.6 shows the histogram of the frequency distribution of the daily maximum UHI intensity as a function of the time of day in each season. The frequency distribution is represented in fraction. In spring and summer, the occurrence frequency in the nighttime is similar and the highest frequency occurs at 0500 LST. Unlike in spring and summer, the most prominent occurrence frequency of the daily maximum UHI intensity in autumn and winter is found at 2000 LST. The occurrence frequency at 0800 LST in autumn and winter is also greater than that in spring and summer. The increase in occurrence frequency in the morning and evening in autumn and winter is likely associated with increased heating activity in ger-houses in the morning and evening in cold months.

Figure 2.7 shows the histogram of the frequency distribution of the daily maximum UHI intensity as a function of the time of day. The occurrence frequency of the daily maximum UHI intensity in the nighttime is 5.6 times that in the daytime. This value is larger than the value for Seoul (3.3) (Kim and Baik 2002).

2.3.3 Effects of meteorological parameters on the daily maximum urban heat island intensity

Following Kim and Baik (2002), a multiple linear regression analysis is performed to examine the relative importance of meteorological parameters that affect the daily maximum UHI intensity. Four meteorological parameters are considered: the maximum UHI intensity for the previous day (PER), wind speed (WS), cloudiness (CL), and relative humidity (RH). The data of wind speed, cloudiness, and relative humidity at Ulaanbaatar station are used for the analysis. The dependent (daily maximum UHI intensity) and independent variables (PER, WS, CL, and RH) are subtracted from the mean and then divided by the standard deviation. This normalization allows us to compare regression coefficients for different parameters and thus understand their relative importance.

The normalized regression coefficients for the four meteorological parameters and the percentage of the total variance explained by the multiple linear regression model are given in Table 2.1. The analysis is performed using all data and classified data in daytime/nighttime and season. All normalized regression coefficients are statistically significant at the 95% confidence level. Half of the variance (49.8%) is explained by the multiple linear regression model. The most important parameter among the four

meteorological parameters is PER. The normalized regression coefficient of PER is 0.48. The stronger daily maximum UHI intensity is mostly led by stronger PER. The second most important parameter is CL. CL is negatively correlated with the daily maximum UHI intensity. That is, the daily maximum UHI intensity increases as CL decreases. The third most important parameter is WS. The daily maximum UHI intensity increases as WS decreases. Under calm or weak wind conditions, the daily maximum UHI intensity becomes strong. Magee et al. (1999) found that the increase in wind speed reduces the UHI intensity in Fairbanks and noted that the reason for the stronger UHI intensity under weak winds is because weak winds allow heat to accumulate near the surface without extensive mixing. Wind speed and UHI intensity have an inverse relationship, and stronger wind enhances turbulent mixing and advection, resulting in a decrease in the temperature difference between urban and rural areas (Oke 1982). The importance of RH to the daily maximum UHI intensity is negligible. Kim and Baik (2004) calculated the normalized regression coefficients of the four meteorological parameters for the six largest cities of South Korea (Seoul, Incheon, Daejeon, Daegu, Gwangju, and Busan) and showed that a more important parameter between CL and WS is CL in Daejeon and Busan and WS in Seoul, Incheon, Daegu, and Gwangju. Oke (1982) mentioned that wind and cloud are surrogate parameters that determine the relative

roles of turbulent and radiative transfer

Table 2.1. Normalized regression coefficients of the four meteorological parameters (PER, maximum UHI intensity for the previous day; WS, wind speed; CL, cloudiness; RH, relative humidity). r^2 is the percentage of the total variance explained by the regression model, and n is the sample size.

	All	Daytime	Nighttime	Spring	Summer	Autumn	Winter
PER	0.48	0.48	0.44	0.30	0.20	0.41	0.32
WS	-0.14	-0.11	-0.14	-0.22	-0.14	-0.15	-0.05
CL	-0.34	-0.27	-0.36	-0.36	-0.44	-0.34	-0.26
RH	0.03	0.17	0.01	-0.06	-0.18	-0.02	0.02
r^2 (%)	49.8	55.6	46.6	33.4	33.4	38.1	18.5
n	11272	11272	1272	2845	2847	2818	2762

in producing temperature changes.

The percentage of the total variance explained by the multiple linear regression model in the daytime (55.6%) is larger than that in the nighttime (46.6%). The normalized regression coefficients of PER and RH are larger in the daytime than in the nighttime. The signs of the normalized regression coefficients for seasonally classified datasets except for RH are the same, but the magnitudes differ. The percentage of the total variance explained by the multiple linear regression model is smaller in winter than in other seasons. This is contrasted with the result for Seoul that shows the smallest percentage of the total variance in spring (Kim and Baik 2002). The smaller percentage of the total variance in winter than in other seasons for Ulaanbaatar means that factors other than the four meteorological parameters affect the daily maximum UHI intensity more in winter than in other seasons. One of the important factors is anthropogenic heat. The anthropogenic heat would be larger and thus have a greater influence on the daily maximum UHI intensity in winter than in other seasons. The larger anthropogenic heat in winter can be one of the reasons for the smaller percentage of the total variance in winter. In spring and summer, the most important parameter is CL and the second most important parameter is PER. In autumn and winter, PER is the most important parameter and CL is the second most important parameter. Different weather conditions and

anthropogenic heat amounts according to season are to some extent responsible for the different relative importance.

3 Interactions of urban breeze circulation with mountain slope winds: A numerical study

This section investigates the interactions of urban breeze circulation with upslope/downslope winds and the dependences of these interactions and urban heat island intensity on mountain height and urban fraction using a mesoscale model coupled with an advanced urban canopy model. Idealized two-dimensional simulations are conducted to clearly understand these interactions and these dependences within a simple framework.

3.1 Experimental design

The numerical model used in this study is the Advanced Weather Research and Forecasting (WRF) model version 3.2 (Skamarock et al. 2008) coupled with the Seoul National University Urban Canopy Model (SNUUCM) (Ryu et al. 2011). The model physics options are as follows: the Yonsei University (YSU) planetary boundary layer scheme (Hong et al. 2006), the Rapid Radiative Transfer Model (RRTM) longwave radiation scheme (Mlawer et al. 1997), the Dudhia shortwave radiation scheme (Dudhia 1989), and the Purdue–Lin cloud microphysics scheme (Chen and Sun 2002). The SNUUCM parameterizes important physical processes that

occur in urban canopies, including absorption and reflection of shortwave and longwave radiation, turbulent energy and water exchanges between surfaces (road, two facing walls, and roof) and adjacent air, and conductive heat transfer through substrates (Ryu et al. 2011). The SNUUCM is coupled with the Noah land surface model (Chen and Dudhia 2001) in a tile approach.

A city and an isolated mountain are considered to examine two-dimensional interactions between urban breeze circulation and mountain slope winds. The city has a size of 20 km, and the urban area consists of built-up (80%) and natural (20%) areas. All natural areas consist of cropland-woodland mosaic (60%) and loamy soil sand (40%). Some important urban parameters in the SNUUCM are specified as follows: the roof level height is 15 m, the canyon aspect ratio is 1, and the emissivity and albedo of all artificial surfaces (road, wall, and roof) are 0.95 and 0.2, respectively. The mountain is Gaussian-shaped with a size of 20 km, which is given by $h(x)=h_m e^{-\left(\frac{x-c}{k}\right)^2}$, where h_m is the maximum mountain height, c is the horizontal location of the mountain peak, and k is the slope parameter ($k = 5000$ m).

The domain size is 200 km in the horizontal and 8 km in the vertical. The horizontal grid interval is 500 m. The vertical grid interval is stretched with height, with the lowest model level being $z = 48$ m, and the number of

vertical layers is 82. The Rayleigh-damping layer is set to $z = 6\text{--}8$ km to avoid the reflection of waves at the top of the physical domain ($z = 6$ km). The lateral boundary condition is periodic. The mountain height is set to zero at mountain-edge grid points. The initial potential temperature at the surface is 298 K, and the lapse rate of the initial potential temperature is 5 K km^{-1} . No basic-state wind is considered to ensure that focus is placed on thermally induced circulation/flow. The initial relative humidity is uniform throughout $z = 0\text{--}4$ km (30%), decreases linearly with height up to $z = 6$ km (where it is 10%), and remains constant above this height. Since this study is concerned with thermally induced local circulations, the initial relative humidity is set to be low so that clouds and precipitation do not occur. The effect of Earth's rotation is neglected, and the latitude is set to 30°N . The model is integrated for 27 h starting from 0500 LST on June 23, and the 24-h simulation data starting from 0800 LST are used for analysis.

3.2 Results and discussions

3.2.1 Urban breeze circulation and mountain slope winds

Figure 3.1 shows the horizontal velocity, vertical velocity, and velocity vector fields and the potential temperature anomaly field at 0900,

1300, 1900, and 2300 LST in a simulation that includes only a city (hereafter, the URBAN simulation). The potential temperature anomaly is calculated as the difference between total and horizontally averaged values at each height. The city spans $x = 100\text{--}120$ km. The urban breeze circulation is induced by the horizontal temperature difference between the urban area and the surrounding rural area.

At 0900 LST, a weak horizontal potential temperature difference is present and an urban breeze circulation is about to form. As the horizontal temperature difference increases with time, the urban breeze circulation becomes well established. The urban breeze circulation is symmetric about the urban center ($x = 110$ km) because there is no basic-state wind. At 1300 LST, urban-breeze fronts are located at $x = 105$ and 115 km and the horizontal wind behind the urban-breeze fronts is strong. The two urban-breeze fronts move toward the urban center, colliding with each other around 1455 LST and subsequently merging to produce strong upward motion. At 1900 LST, a strong updraft cell centered at the urban center appears, with a maximum updraft intensity of 2.0 m s^{-1} at $z = 1150$ m. Note that 1900 LST is very close to the sunset time on June 23 (~ 1858 LST). The urban breeze circulation is stronger in the late afternoon/early evening than in the early afternoon (Figs. 3.1b,c). This is consistent with the result of Savijarvi and Liya (2001). The simulated urban breeze circulation is

characterized by converging flow in the lower layer and diverging flow in the upper layer (Figs. 3.1b,c). At 1300 and

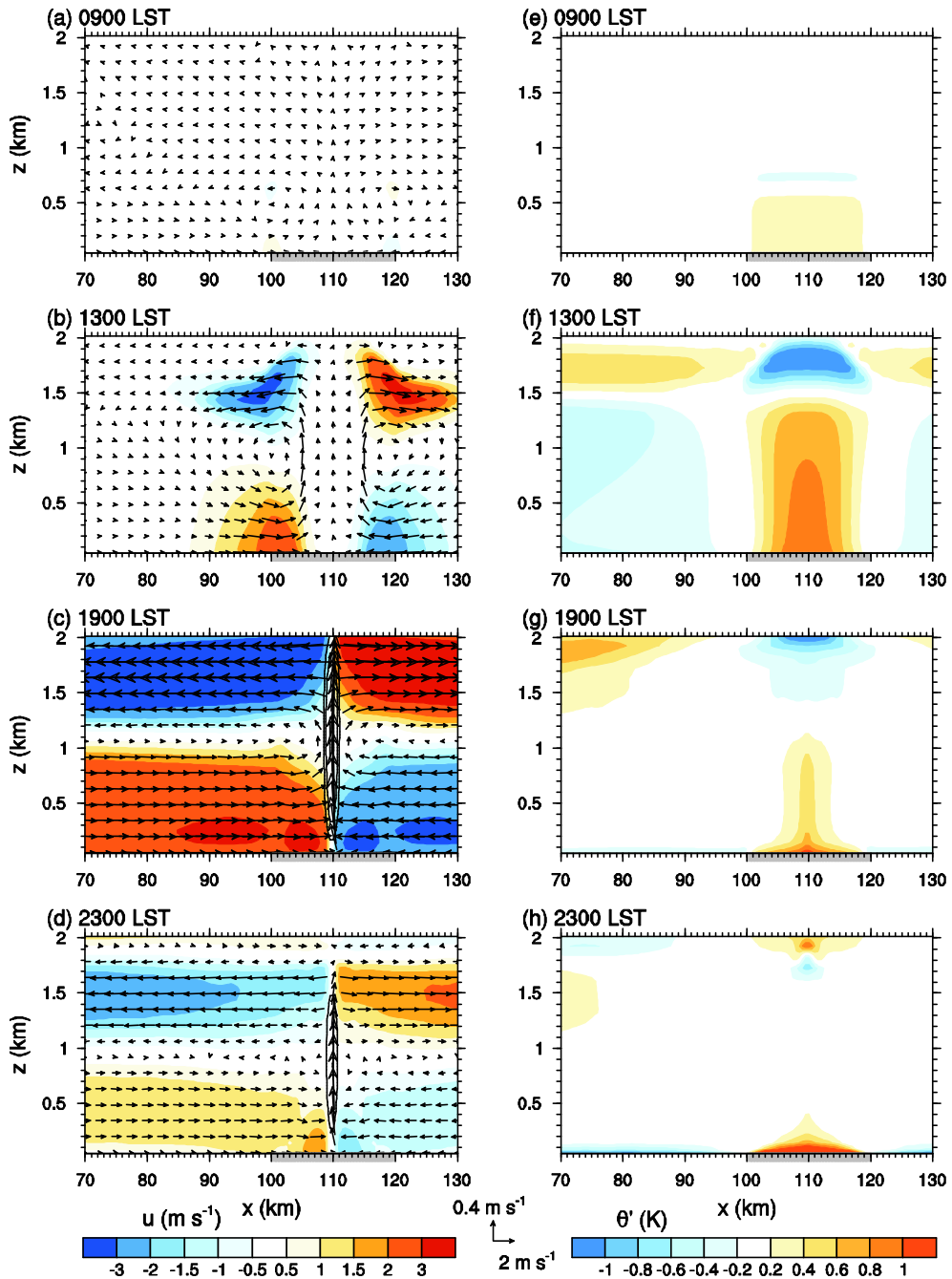


Figure 3.1. Horizontal velocity (shading), vertical velocity (contour), and velocity vector fields at (a) 0900, (b) 1300, (c) 1900, and (d) 2300 LST and corresponding potential temperature anomaly field (shading) at (e) 0900, (f)

1300, (g) 1900, and (h) 2300 LST in the URBAN simulation. The gray box on the x -axis (also in Figs. 3.3, 3.4, 3.7, 3.8, 3.11) indicates the urban area. The contour levels of vertical velocity are 0.5, 1, and 2 m s^{-1} .

1900 LST, deeper urban boundary layer results in the negative (cold) potential temperature anomaly in the upper layer owing to higher potential temperature in the rural area than in the urban area at the same upper level because of strong stratification above the top of rural boundary layer (Figs. 3.1f,g). The horizontal size of the urban breeze circulation at 1300 (1900) LST is 2.0 (3.9) times as large as the urban size. This is similar to the results of Hidalgo et al. (2008a) and Ryu et al. (2013a). The vertical size of the urban breeze circulation is ~1.8 km at 1300 LST and ~2.2 km at 1900 LST. It is notable that the horizontal and vertical sizes of the urban breeze circulation vary considerably with time. In the nighttime, although the near-surface potential temperature difference between the urban area and the surrounding rural area is relatively large (i.e., larger nighttime urban heat island), the urban breeze circulation is weak owing to nighttime stable stratification that suppresses vertical motion (Fig. 3.1d).

A simulation with Earth's rotation was performed with flat terrain and a city being considered, and simulation results were compared with the results of the simulation without Earth's rotation (that is, the URBAN simulation). In both the simulations, daytime urban breeze circulations are similar to each other. When the Earth's rotation is included, in the late evening, winds start to turn away from the city above the surface, exhibiting

an anti-urban heat island circulation-like feature (Savijarvi and Liya 2001).

The transverse wind

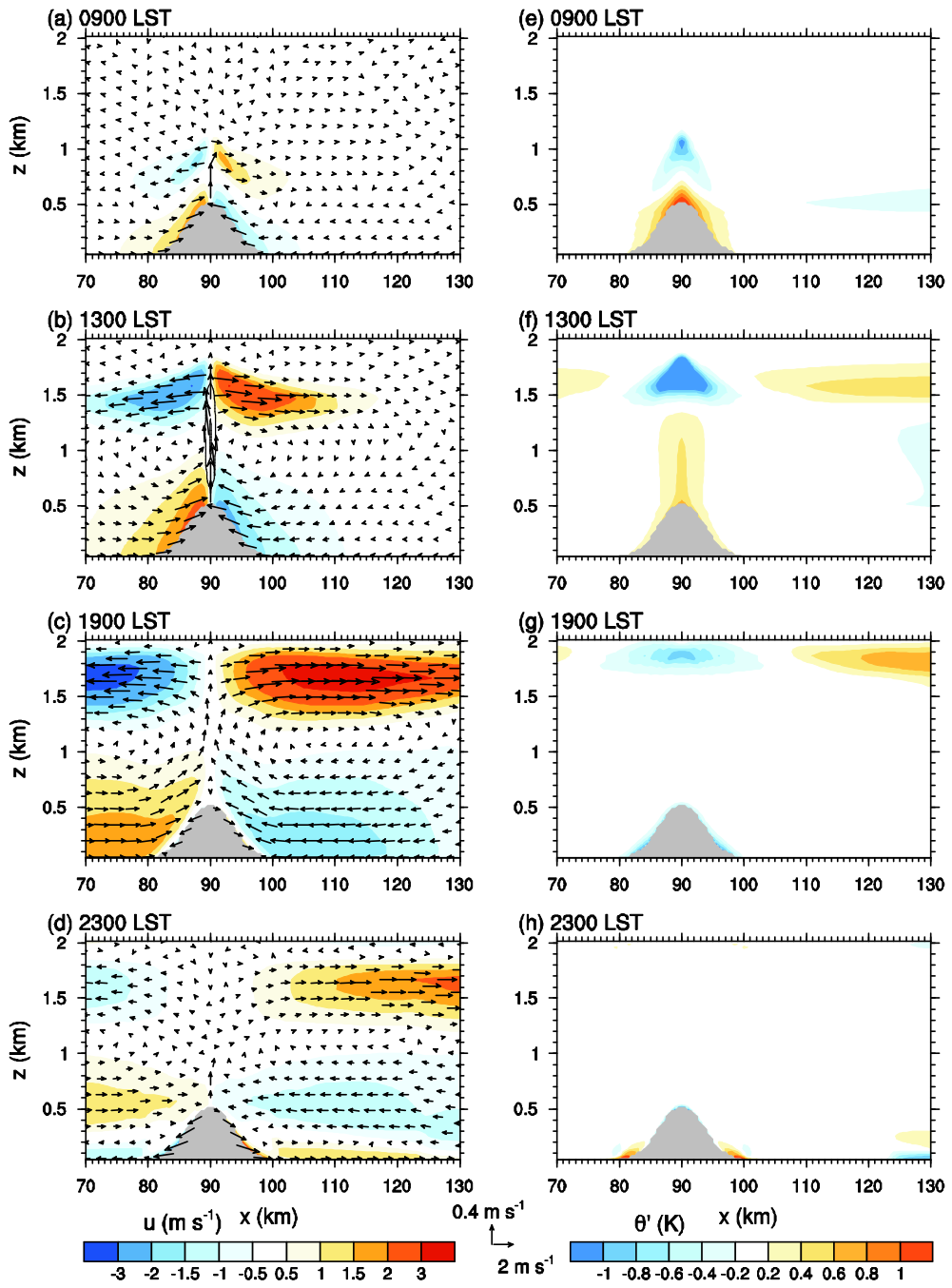


Figure 3.2. Same as in Fig. 3.1 but for the MOUNT simulation. The contour levels of vertical velocity are 0.5 and 1 m s⁻¹.

(v velocity) arises in the simulation with Earth's rotation due to the Coriolis force, but in the daytime its magnitude is smaller than that of u velocity.

Figure 3.2 shows the horizontal velocity, vertical velocity, and velocity vector fields and the potential temperature anomaly field at 0900, 1300, 1900, and 2300 LST in a simulation that includes only a mountain (hereafter, the MOUNT simulation). In this simulation, the mountain peak is located at $x = 90$ km, and the maximum mountain height (h_m) is 500 m. As expected, the upslope (downslope) wind appears at 0900 and 1300 (1900 and 2300) LST. Note that the downslope wind at 1900 LST occurs near the mountain-slope surface. At 1300 LST, a strong updraft cell is produced over the mountain top and flow in the upper layer diverges away from the mountain, forming an apparent mountain circulation. Above the mountain top, a weak warm region and a relatively strong cold region are observed. The upslope wind attains a maximum intensity of 2.2 m s^{-1} around 1340 LST. The transition from upslope wind to downslope wind at a mid-slope location ($x = 95$ km) occurs around 1845 LST. During the 24-h period, the occurrence frequency of the 10-m upslope wind at the mid-slope location (47%) is similar to that of the downslope wind (53%).

3.2.2 Interactions of urban breeze circulation with mountain slope winds

To examine interactions between urban breeze circulation and mountain slope winds, a numerical experiment in which both a city and a mountain exist is performed. This simulation is referred to as the URBAN-MOUNT simulation. The horizontal size of the city (20 km) is the same as that of the mountain, and the horizontal location of the mountain peak (urban center) is $x = 90$ (110) km. The maximum mountain height is set to 500 m. Several terms are utilized in the present study to indicate areas or locations within the domain. The mountain slope on the rural (urban) side is referred to as the rural-side (urban-side) mountain slope and spans $x = 80$ –90 (90–100) km (Fig. 3.3). The urban area whose edge borders the mountain (plain) area is referred to as the mountain-side (plain-side) urban area and spans $x = 100$ –110 (110–120) km. The urban periphery that borders the mountain (rural) area is referred to as the mountain–urban (urban–rural) edge [$x = 100$ (120) km]. In the URBAN-MOUNT simulation, the mountain–urban edge is located at the center of the domain.

Figure 3.3 shows the horizontal velocity, vertical velocity, and velocity vector fields and the potential temperature anomaly field at five different times (1300, 1500, 1600, 1900, and 2300 LST) in the URBAN-

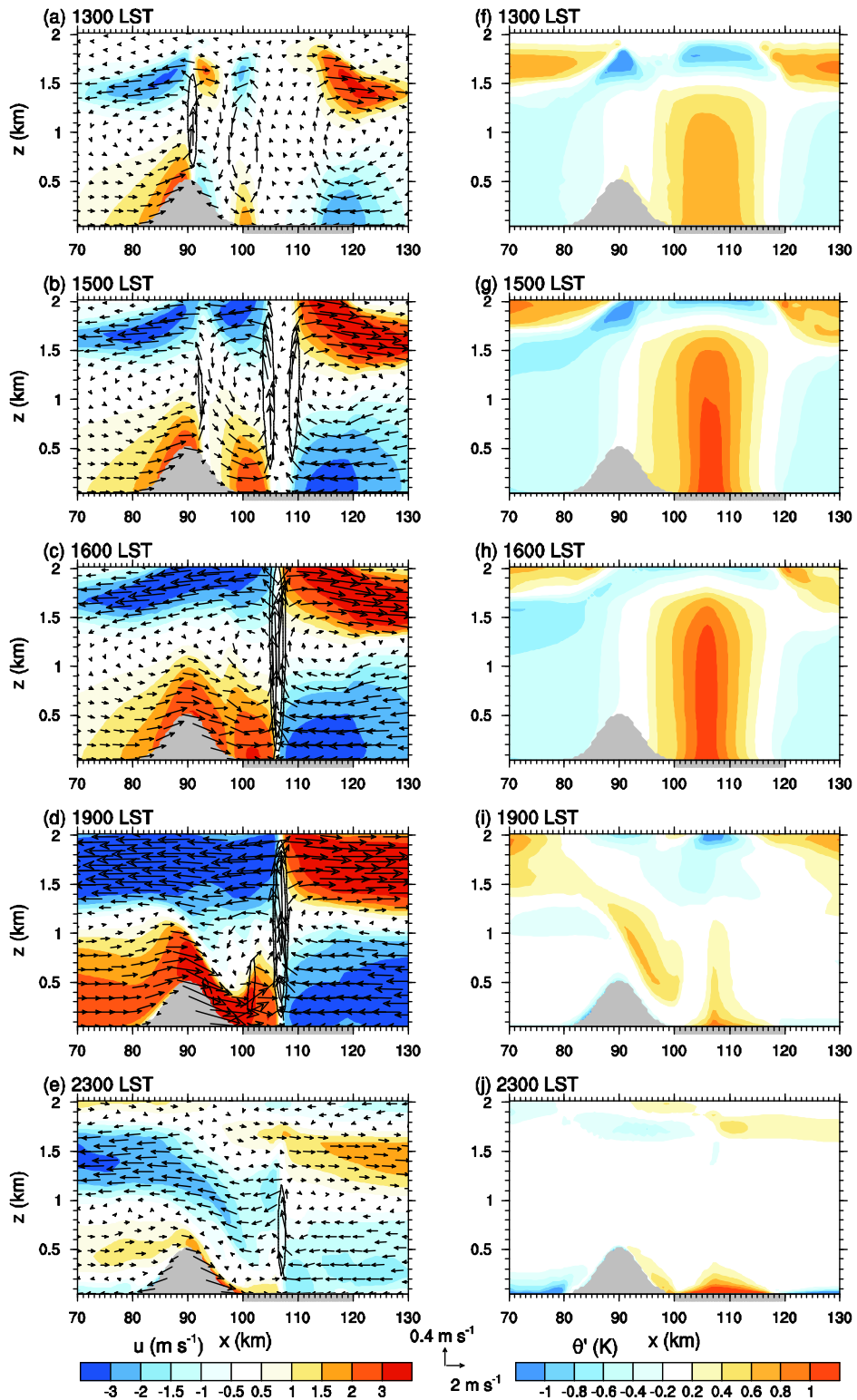


Figure 3.3. Horizontal velocity (shading), vertical velocity (contour), and velocity vector fields at (a) 1300, (b) 1500, (c) 1600, (d) 1900, and (e) 2300 LST and corresponding potential temperature anomaly field (shading) at (f) 1300, (g) 1500, (h) 1600, (i) 1900, and (j) 2300 LST in the URBAN-MOUNT simulation. The gray box on the x -axis indicates the urban area. The contour levels of vertical velocity are -0.5 (dashed line, Fig. 3.3d), 0.5 , 1 , and 2 m s^{-1} .

MOUNT simulation. At 1300 LST, the upslope wind on the mountain slope and an updraft cell over the mountain top are produced. The upslope wind is stronger on the rural-side mountain slope than on the urban-side mountain slope because the mountain upslope wind on the urban-side mountain slope is opposed by the urban breeze. The circulation over the urban area is not symmetric about the urban center owing to the influence of the mountain circulation. At 1500 LST, the upslope wind exists on the rural-side mountain slope, whereas the downslope wind exists in the lower region of the urban-side mountain slope. Two updraft cells over the urban area are apparent and are associated with urban-breeze fronts. The updraft cell centered at $x = 105.5$ km is influenced more by the mountain circulation than that centered at $x = 109.5$ km. A deep warm region centered at $x = 105.5$ km is formed (Fig. 3.3g). The two updraft cells move toward each other, colliding around 1540 LST and subsequently merging to produce a strong updraft cell. At 1600 LST, the downslope wind on the urban-side mountain slope is produced and the two updraft cells are merged into a strong updraft cell centered at $x = 106.5$ km. The plain-side urban wind pushes the urban breeze convergence zone toward the mountain. At 1900 LST, the downslope wind on the urban-side mountain slope is enhanced. At 2300 LST, the downslope wind is present on both sides of the mountain, the urban wind weakens, and a shallow warm region is observed over the urban

area. In this study, night-morning transitions and circulations are not focused, but they deserve an investigation with a longer time simulation.

Fernando (2010) noted that downslope flow approaching a slope break may undergo hydraulic adjustment and then merge with the urban nocturnal atmospheric boundary layer. In the URBAN-MOUNT simulation, a clear hydraulic jump appears at 1900 LST (Fig. 3.3d). The urban-side mountain downslope wind accelerates while descending through a thin layer (Fig. 3.3d). Around 1800 LST, a hydraulic jump starts to occur near the mountain–urban edge when the strong and thin downslope wind merges with the urban wind. Additionally, the larger roughness length in the urban area contributes partly to the development of this hydraulic jump. The upward motion in association with the hydraulic jump has a maximum intensity of 1 m s^{-1} at 2000 LST, and afterward the hydraulic jump begins to weaken and eventually disappears.

Savijarvi and Liya (2001) demonstrated that urban breeze circulation opposes the weak daytime upslope circulation of a narrow valley. Similarly, Ohashi and Kida (2002) showed that in the daytime the weakening of winds toward urban and mountain areas is caused by their opposing wind directions. In essence, the results of the present study are consistent with those of both Savijarvi and Liya (2001) and Ohashi and Kida (2002).

The combined effects of the city and mountain on the local wind system produce some interesting features, including an earlier transition from upslope wind to downslope wind on the urban-side mountain slope and a stronger downslope wind. At the mid-slope location of the urban-side mountain slope, the transition from upslope wind to downslope wind occurs around 1430 LST, which is approximately 4 h earlier than the transition in the MOUNT simulation. The rural-side upslope wind passes over the mountain top, and the urban-side downslope wind is enhanced (Fig. 3.3c,d). The combined effects of the city and mountain also produce an extended period of urban-side downslope wind. The occurrence frequency of downslope wind at the urban-side mid-slope location constitutes 68% of total wind during the 24-h period.

Figure 3.4 shows the distance–time section of 10-m horizontal wind in the URBAN, MOUNT, and URBAN-MOUNT simulations. Note that the mountain and city span $x = 80\text{--}100$ km and $x = 100\text{--}120$ km, respectively. The urban breeze is weaker and its horizontal extent is smaller in the nighttime than in the daytime (Fig. 3.4a). Around 1635 LST, the urban breeze reaches its maximum intensity of 2.9 m s^{-1} at $x = 103$ and 117 km. The horizontal extension and intensity of downslope wind are smaller and weaker, respectively, than those of upslope wind (Fig. 3.4b). Around 1840

LST, the transition from upslope wind to downslope wind begins near the mountain

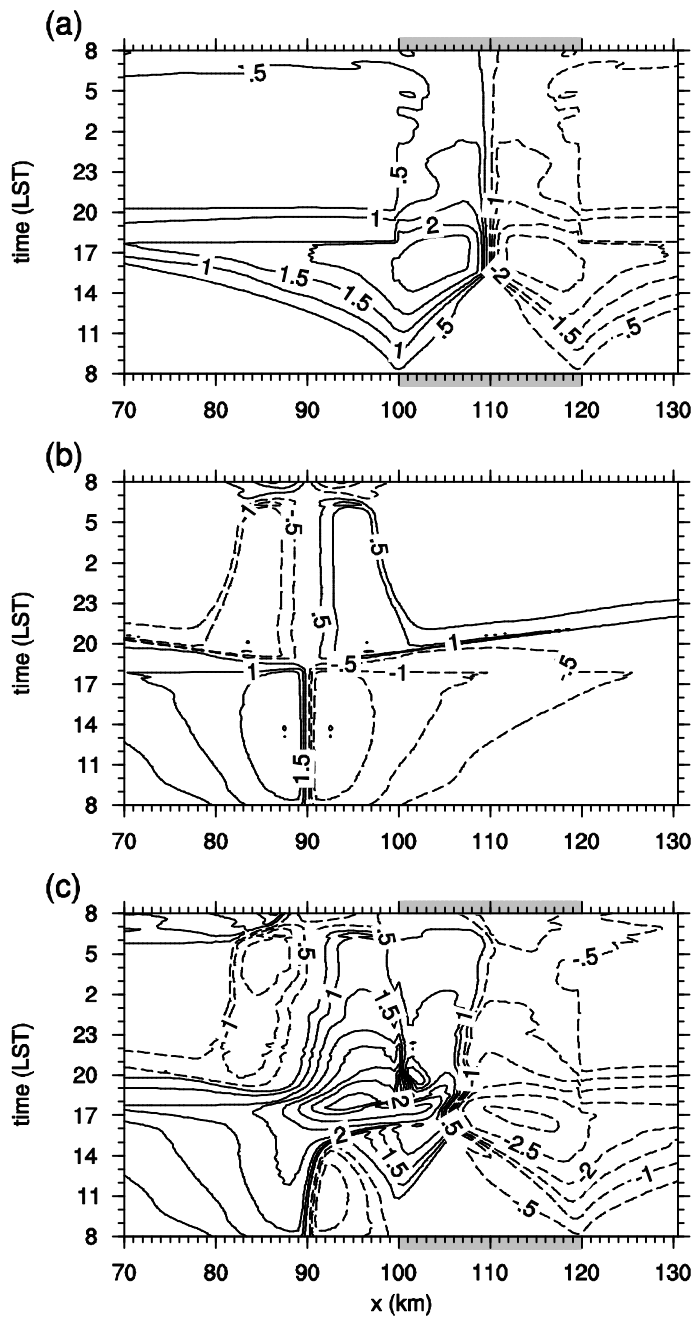


Figure 3.4. Distance-time section of horizontal wind at 10 m above the surface in the (a) URBAN, (b) MOUNT, and (c) URBAN-MOUNT simulations. The gray box on the x -axis indicates the urban area. The

mountain is located in the region from $x = 80$ to 100 km in (b) and (c). The contour intervals are 0.5 m s^{-1} .

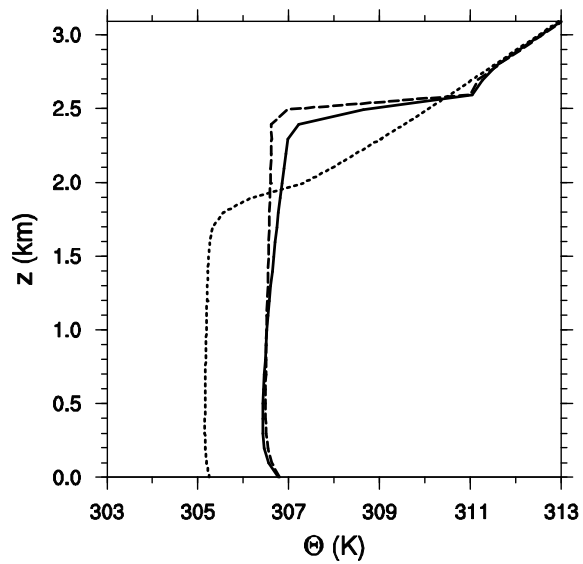


Figure 3.5. Vertical profiles of potential temperature at $x = 110$ km and $t = 1600$ LST in the URBAN (dashed), MOUNT (dotted), and URBAN-MOUNT (solid) simulations.

top. The downslope wind reaches its maximum intensity of 1.5 m s^{-1} around 1925 LST, and the upslope wind starts again around 0650 LST.

In the URBAN-MOUNT simulation, asymmetric winds over the urban area appear owing to the combined effects of the city and mountain (Fig. 3.4c). The onset of the mountain-side urban breeze is delayed by about 2 h with respect to that of the plain-side urban breeze. The transition from upslope wind to downslope wind on the urban-side mountain slope occurs earlier than that on the rural-side mountain slope. The maximum downslope wind speed at the urban-side mid-slope location (4.2 m s^{-1}) is roughly twice the maximum downslope wind at the rural-side mid-slope location (1.9 m s^{-1}). Moreover, the plain-side urban wind in the URBAN-MOUNT simulation is slightly stronger than that in the URBAN simulation. In the nighttime, the urban wind is slightly stronger in the URBAN-MOUNT simulation than in the URBAN simulation and the downslope wind is slightly stronger in the URBAN-MOUNT simulation than in the MOUNT simulation.

The vertical profiles of potential temperature at $x = 110 \text{ km}$ in the URBAN, MOUNT, and URBAN-MOUNT simulations are presented in Fig. 3.5 for 1600 LST. A well-mixed boundary layer is produced. The boundary layer height in the URBAN ($\sim 2430 \text{ m}$) and URBAN-MOUNT ($\sim 2340 \text{ m}$) simulations is higher than that in the MOUNT simulation ($\sim 1730 \text{ m}$) owing to stronger surface sensible heat flux in the presence of the city. The

potential temperature near $z = 2$ km is higher in the URBAN-MOUNT simulation than in the URBAN simulation, although the potential temperature profiles for these simulations are generally very similar.

To reveal the nonlinear interactions of urban breeze circulation with mountain slope winds, the distance–time section of 10-m horizontal wind of a linear superposition of the URBAN and MOUNT simulations is compared with that of the URBAN-MOUNT simulation (not shown). Larger differences are found generally in the daytime. In the daytime, the linear superposition does not show the earlier occurrence of the urban-side downslope winds, hydraulic jump, intensified upslope winds on the rural-side mountain slope, and shift of convergence wind toward the mountain. In the nighttime, nonlinear interaction shows the intensified downslope winds on the urban-side mountain slope in comparison with the linear superposition.

To examine the topographic shading effect on the interactions of urban breeze circulation with mountain slope winds, the simulation which includes the topographic shading effect (URBAN-MOUNT_SHAD) is tested. Distance-time sections of horizontal wind at 10 m above the surface in the URBAN-MOUNT_SHAD, URBAN-MOUNT, and their difference are shown in Fig. 3.6. Overall features between URBAN-MOUNT and

URBAN-MOUNT_SHAD simulations are very similar, but some distinct features appear owing to the topographic shading effect. The differences are

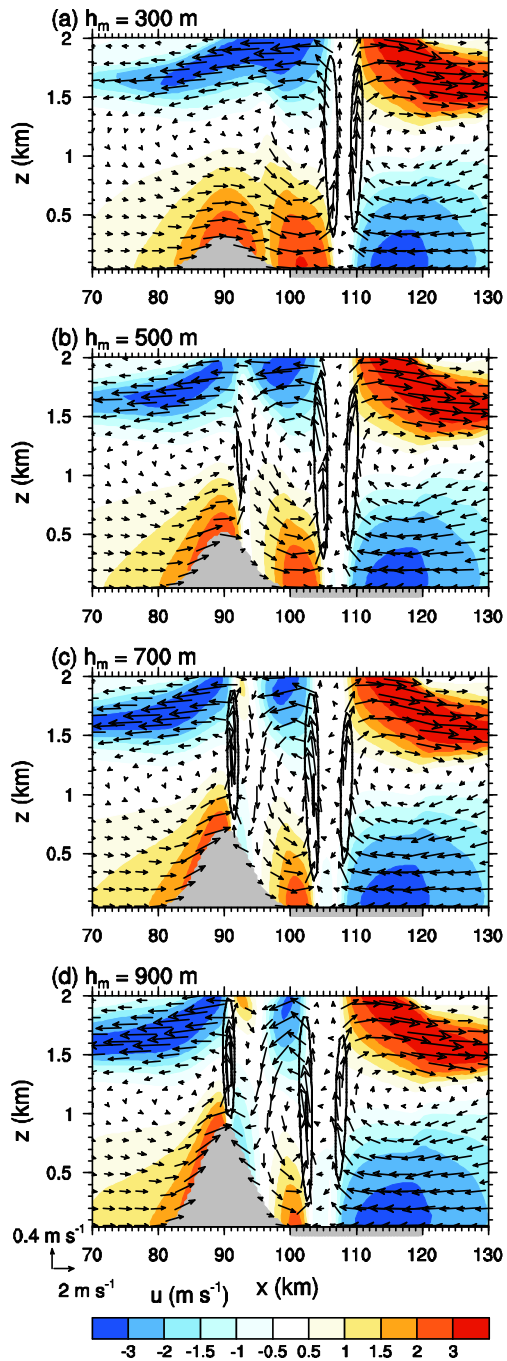


Figure 3.6. Horizontal velocity (shading), vertical velocity (contour), and velocity vector fields at 1500 LST in the simulations with maximum

mountain heights of (a) 300, (b) 500, (c) 700, and (d) 900 m. The contour levels of vertical velocity are 0.5 and 1 m s⁻¹.

significant in the daytime. In the morning, as the sunward (urban-side mountain) slope is heated more than the shadow-ward (rural-side mountain) slope, the upslope winds on that slope are slightly stronger (difference up to $\sim 0.2 \text{ m s}^{-1}$) in the URBAN-MOUNT_SHAD simulation than that in the URBAN-MOUNT simulation. As a consequence, the mountain-side urban wind and rural-side upslope winds are slightly weaker than those in the URBAN-MOUNT simulation. The positive difference over the mountain top is associated with slightly stronger upslope winds on the urban-side mountain slope. By noon, the difference in slope winds between the simulations become small. At the mid-slope location of the urban-side mountain slope, the transition from upslope wind to downslope wind occurs around 1440 LST (10 min later than the URBAN-MOUNT simulation). Due to later occurrence of the downslope winds on the urban-side slope, the negative difference is shown over the mountain peak and urban-side slope in the afternoon. Moreover, related with less heated urban-side slope due to topographic shading, the positive difference is shown in the afternoon. After 1500 LST, as rural-side slope is heated more than the urban-side slope, the upslope winds on the rural-side slope becomes generally stronger (up to $\sim 0.6 \text{ m s}^{-1}$) than that on the urban-side slope.

The occurrence frequency of downslope wind at the urban-side mid-slope location constitutes 65% of total wind during the 24-h period. As expected, the mountain shading effect is negligible in the nighttime.

3.2.3 Sensitivity to mountain height and urban fraction

The effects of mountain height and urban fraction on interactions between urban breeze circulation and mountain slope winds and urban heat island intensity are examined here, based upon sensitivity experiments conducted for various maximum mountain heights and urban fractions in the presence of both a city and a mountain. The mean slope angles of mountains are 1.7° , 2.8° , 3.9° , and 5.1° , respectively, for maximum mountain heights of 300, 500, 700, and 900 m. The 500 m case is the URBAN-MOUNT simulation case (section 3.2.2). The experimental setup and parameter values in the other three cases are the same as those in the URBAN-MOUNT simulation but for maximum mountain height (h_m). As mountain height increases, the rural-side upslope wind weakens slightly but exists longer. In the simulation with $h_m = 300$ m, the downslope wind is evident on the urban-side mountain slope (Fig. 3.7a). The urban-side downslope wind in the simulation with $h_m = 300$ m is much stronger than that in the

simulation with $h_m = 500$ m (Fig. 3.7a, b). In the simulations with $h_m = 700$ and 900 m, the upslope wind and downslope wind coexist on the urban-side mountain slope, with stronger upslope wind in the upper slope region and weaker downslope wind in the lower slope region in the $h_m = 900$ m simulation than in the $h_m = 700$ m simulation (Fig. 3.7c,d). These features likely occur because the urban effect becomes more important than the mountain effect at 1500 LST as mountain height decreases. Lee and Kimura (2001) demonstrated that anabatic winds strengthen as mountain height increases and that mountain height is one of the major factors affecting the temporal evolution of predominant mesoscale circulation over inhomogeneous land surfaces and non-uniform terrain. In the present study, the plain-side urban wind intensifies slightly as mountain height increases (Fig. 3.7). In the simulation with $h_m = 900$ m, the updraft cell lies immediately over the mountain top. Two updraft cells over the urban area, which are associated with the two urban-breeze fronts, are located further toward the mountain as mountain height increases. This is likely related to the stronger plain-side urban wind that occurs in the simulations with greater mountain heights.

The horizontal velocity, vertical velocity, and velocity vector fields at 1500 LST in simulations with urban fractions of 0.2, 0.4, 0.6, and 0.8 are

presented in Fig. 3.8. The 0.8 case is the URBAN-MOUNT simulation case (section 3.2.2). The experimental setup and parameter values in the other

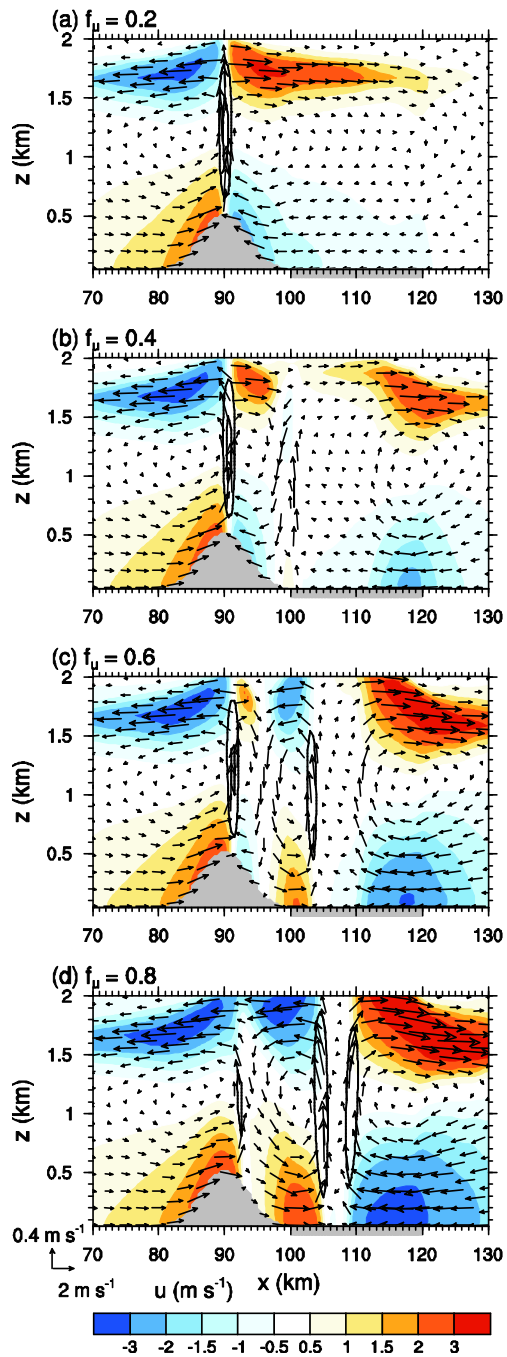


Figure 3.7. Same as in Fig. 3.6 but for the simulations with urban fractions of (a) 0.2, (b) 0.4, (c) 0.6, and (d) 0.8.

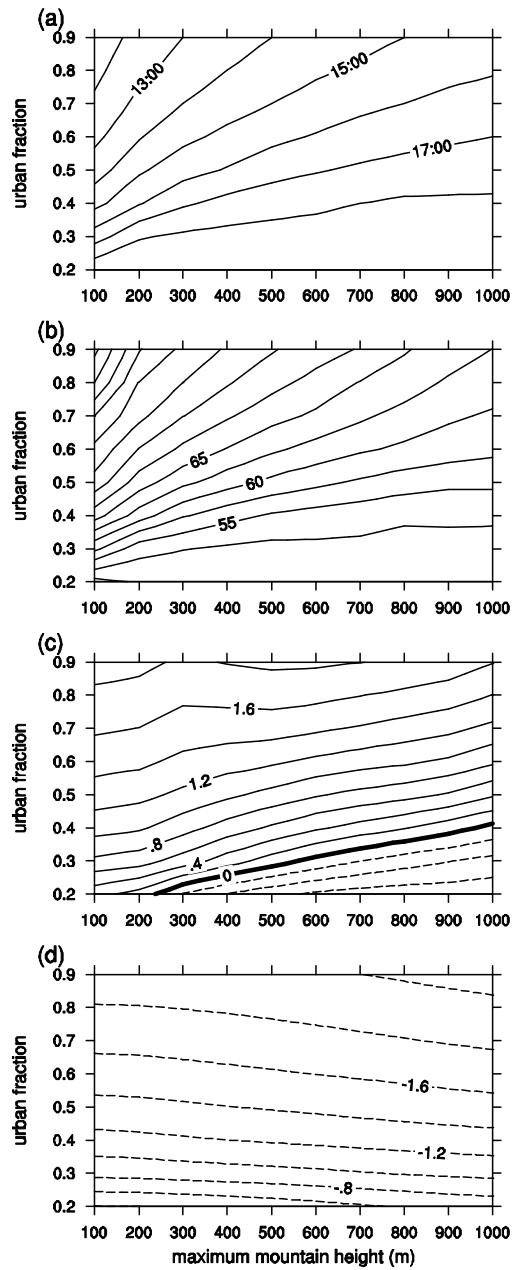


Figure 3.8. Transition time from upslope wind to downslope wind (at 10 m above the slope) at the urban-side mid-slope location ($x = 95$ km), (b) percentage of the occurrence frequency of downslope wind (at 10 m above

the slope) at the urban-side mid-slope location, and 10-m horizontal wind at (c) the mountain–urban edge ($x = 100$ km) and (d) the urban–rural edge ($x = 120$ km) as a function of maximum mountain height and urban fraction. (c) and (d) are averaged over the period 0800–2000 LST, and (b) is for the one-day period 0800–0800 LST. The contour intervals in (a), (b), (c), and (d) are 1 h, 2.5%, 0.2 m s^{-1} , and 0.2 m s^{-1} , respectively.

three cases are the same as those in the URBAN-MOUNT simulation but for urban fraction (f_u). As urban fraction increases, the urban breeze circulation intensifies owing to stronger sensible heat flux. This is consistent with the results of Zhang et al. (2014). In the simulation with $f_u = 0.8$, the urban wind is stronger than that in the simulation with $f_u = 0.6$. In the simulations with $f_u = 0.6$ and 0.8 , the upslope wind and downslope wind coexist on the urban-side mountain slope, with stronger downslope wind in the lower region and weaker upslope wind in the upper region in the simulation with $f_u = 0.8$ than in the simulation with $f_u = 0.6$. These features likely occur because the mountain effect becomes more important than the urban effect at 1500 LST as urban fraction decreases. The rural-side upslope wind tends to accelerate slightly in the upper slope region with increasing urban fraction (Fig. 3.8). In the simulations with $f_u = 0.6$ and 0.8 , the updraft cells with vertical velocity greater than 0.5 m s^{-1} are evident over the urban area (Fig. 3.8c,d). The updraft cell over the mountain top weakens and moves slightly toward the urban-side slope as urban fraction increases.

Extensive numerical experiments are conducted to examine the dependencies of urban wind and slope winds on mountain height and urban fraction. To achieve this, maximum mountain height is varied from 100 to 1000 m at intervals of 100 m and urban fraction is varied from 0.2 to 0.9 at intervals of 0.1; this results in 80 simulations. Figure 3.9 shows the

transition time from upslope wind to downslope wind and the percentage of occurrence frequency of downslope wind at the urban-side mid-slope location ($x = 95$ km) and the horizontal winds at the mountain–urban edge ($x = 100$ km) and the urban–rural edge ($x = 120$ km) as a function of maximum mountain height and urban fraction. The horizontal winds at the mountain–urban and urban–rural edges are averaged over the period 0800–2000 LST, and the percentage of the occurrence frequency of downslope wind at $x = 95$ km is over a 1-day period spanning 0800–0800 LST.

The transition from upslope wind to downslope wind starts earlier as mountain height decreases and urban fraction increases (Fig. 3.9a). The transition time exhibits a greater dependency on mountain height when urban fraction is larger. The simulation with the highest mountain ($h_m = 1000$ m) and smallest urban fraction ($f_u = 0.2$) exhibits the latest transition from upslope wind to downslope wind, which occurs at 1835 LST. Conversely, the simulation with the lowest mountain ($h_m = 100$ m) and largest urban fraction ($f_u = 0.9$) shows the earliest transition, which occurs at 1125 LST. This change in transition time influences interactions between urban breeze circulation and mountain slope winds.

The occurrence frequency (%) of downslope wind at the urban-side mid-slope location during the 1-day period increases as mountain height

decreases and urban fraction increases (Fig. 3.9b). The occurrence frequency

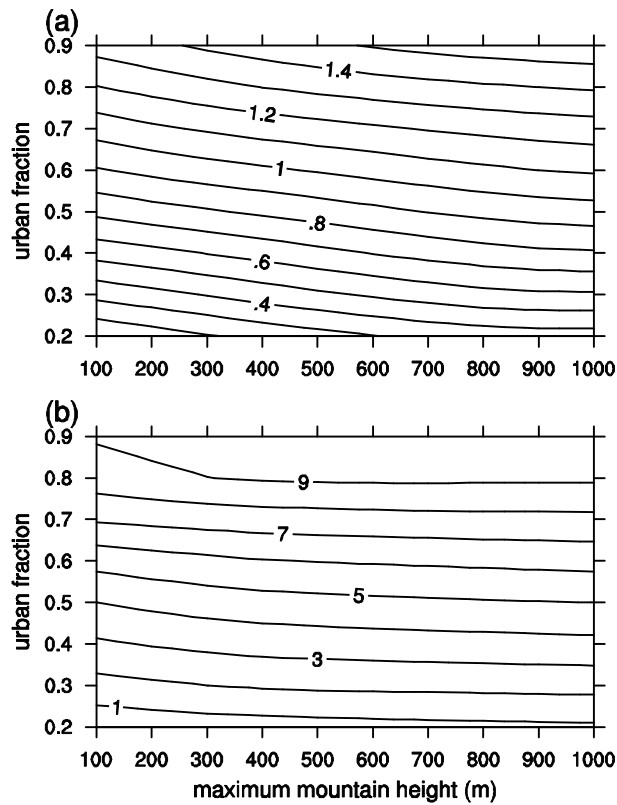


Figure 3.9. (a) Daytime (1200–1700 LST) and (b) nighttime (0000–0500 LST) averaged urban heat island intensities as a function of maximum mountain height and urban fraction.

of downslope wind is more sensitive to urban fraction when mountain height is lower. When urban fraction is smaller, the occurrence frequency of downslope wind has a smaller sensitivity to mountain height. The occurrence frequency of upslope wind is similar to that of downslope wind when urban fraction is very small. In the simulation with the lowest mountain and largest urban fraction, the downslope wind consists of 85% of total wind according to its occurrence frequency.

The averaged 10-m horizontal wind at the mountain–urban edge is toward the urban or mountain area depending on mountain height and urban fraction (Fig. 3.9c). The strongest wind toward the mountain area (0.8 m s^{-1}) occurs in the simulation with the highest mountain and smallest urban fraction, whereas the strongest wind toward the urban area (1.8 m s^{-1}) occurs in the simulation with the lowest mountain and largest urban fraction. Each urban fraction increase of 0.1 results in an average increase of 0.3 m s^{-1} in the speed of wind toward the urban area. Each maximum mountain height increase of 100 m results in an average increase of 0.1 m s^{-1} in the speed of wind travelling toward the mountain area.

The averaged 10-m horizontal wind at the urban–rural edge strengthens as mountain height increases and urban fraction increases (Fig. 3.9d). The dependency of the horizontal wind on mountain height is small for a given urban fraction, whereas the dependency of the horizontal wind

on urban fraction for a given mountain height is relatively large. The horizontal wind is strongest (2.1 m s^{-1}) in the simulation with the highest mountain and largest urban fraction and weakest (0.4 m s^{-1}) in the simulation with the lowest mountain and smallest urban fraction. Here, each urban fraction increase of 0.1 results in an average increase of 0.2 m s^{-1} in the plain-side urban wind.

Figure 3.10 shows the daytime- and nighttime-averaged urban heat island intensities as a function of maximum mountain height and urban fraction. Here, the urban heat island intensity is calculated as the difference in 2-m air temperature averaged over $x = 100\text{--}120 \text{ km}$ between any case with given maximum mountain height and urban fraction and the case with homogeneous surface and uniform terrain (no city and no mountain). The daytime and nighttime averages are taken from 1200 to 1700 LST and from 0000 to 0500 LST, respectively. As expected, the urban heat island is stronger in the nighttime than in the daytime. In both the daytime and nighttime, the sensitivity of urban heat island intensity to urban fraction is more significant than that to maximum mountain height. The daytime urban heat island intensity increases as mountain height increases and urban fraction increases. In the nighttime, the dependency of urban heat island intensity on urban fraction is considerably large for a given maximum mountain height.

The nighttime urban heat island intensity for a given urban fraction varies very little with mountain height when maximum mountain height is greater than about 500 m. Each urban fraction increase of 0.1 results in average increases of 0.17 and 1.27°C in the daytime and nighttime urban heat island intensities, respectively.

3.3 A city in a basin

This section presents the results of a simulation in which a city is located in a basin between two isolated mountains (the BASIN simulation). In this case, the urban center coincides with the domain and basin centers, two identical mountains have maximum heights of 500 m, and the urban fraction is 0.8. Figure 3.11 shows the horizontal velocity, vertical velocity, and velocity vector fields at 1300, 1500, 1600, 1900, and 2300 LST in the BASIN simulation. The circulation developed is symmetric about the city center. At 1300 LST, the plain-side upslope wind and the return flow over the plain side are stronger and deeper than those over the basin side owing to the weakened urban-side upslope wind that is associated with the opposing urban breeze. The urban-side upslope wind reaches a maximum intensity of 1.9 m s^{-1} around 1025 LST. At the urban-side mid-slope location, the downslope wind starts around 1400 LST. This downslope wind facilitates the plain-to-

Figure 3.10. Horizontal velocity (shading), vertical velocity (contour), and velocity vector fields at (a) 1200, (b) 1500, (c) 1600, (d) 1900, and (e) 2300 LST in the BASIN simulation. The gray box on the x -axis indicates the urban area. The contour levels of vertical velocity are -0.5 (dashed line, Fig. 3.10d), 0.5 , 1 , and 2 m s^{-1} .

basin wind. The earlier onset of plain-to-basin wind in the present study is distinct from the results of previous studies adopting homogeneous land surfaces (e.g., Kimura and Kuwagata 1993; de Wekker et al. 1998); such studies have suggested that the plain-to-basin wind commences at dusk. Valley geometry results in the accumulation of more heat than plain geometry (Kimura and Kuwagata 1995), thus producing lower pressure inside the valley than over the plain. At 1500 and 1600 LST, there are two updraft cells over the urban area. These cells move toward the urban center and merge around 1635 LST. The urban-side downslope wind attains a maximum intensity of 7.9 m s^{-1} around 1815 LST; this is stronger than the downslope wind on the urban-side slope in the URBAN-MOUNT simulation. At 1900 LST, a strong updraft cell appears over the urban center. As demonstrated in Kimura and Kuwagata (1993), the strong downslope wind on the basin-side mountain slope around sunset or after dusk is owing to the plain-to-basin wind as well as the downslope wind. The transition time from upslope wind to downslope wind at the rural-side mid-slope location in the BASIN simulation is almost the same as that in the URBAN-MOUNT simulation. The urban-side downslope wind persists longer than the rural-side downslope wind. Around 1745 LST, hydraulic jumps occur near the mountain–urban edges. They persist until 2145 LST. The potential temperature anomaly over the urban area is smaller in the BASIN

simulation than in the URBAN-MOUNT simulation (not shown). This is likely associated with stronger plain-to-basin wind from the plain areas in the BASIN simulation, which contributes to cooling of the basin air.

4 Interactions of urban breeze circulation with mountain slope winds: A theoretical study

In the previous section, the two-dimensional interactions of urban breeze circulation with mountain slope winds and the dependences of these interactions and urban heat island intensity on urban fraction and mountain height under no basic state wind were investigated using the numerical model which includes an urban canopy model. The present section investigates the circulations induced by thermal forcings in urban and mountain areas through a linear, theoretical approach. Also, the sensitivities of the interactions of urban breeze circulation and mountain slope winds to the urban and mountain thermal forcings are examined.

4.1 Governing equations, solutions, and experimental settings

4.1.1 Governing equations and solutions

Consider a two-dimensional, hydrostatic, nonrotating, Boussinesq airflow system. Equations governing small-amplitude perturbations with

constant basic-state horizontal wind and buoyancy frequency in the presence of thermal forcing can be written as

$$\frac{\partial u}{\partial t} + U \frac{\partial u}{\partial x} = -\frac{\partial \pi}{\partial x} - \nu u, \quad (4.1)$$

$$\frac{\partial \pi}{\partial z} = b, \quad (4.2)$$

$$\frac{\partial b}{\partial t} + U \frac{\partial b}{\partial x} + N^2 w = \frac{g}{c_p T_0} q - \nu b, \quad (4.3)$$

$$\frac{\partial u}{\partial x} + \frac{\partial w}{\partial z} = 0, \quad (4.4)$$

Here, u and w are the perturbation velocities in the x - and z -directions, respectively, π is the perturbation kinematic pressure, b is the perturbation buoyancy, U is the basic-state wind speed in the x -direction, N is the buoyancy frequency, g is the gravitational acceleration, c_p is the specific heat of air at constant pressure, T_0 is the reference temperature, and ν is the coefficient of Rayleigh friction and Newtonian cooling. The thermal forcing q is specified to be bell-shaped in the horizontal, to decrease exponentially with height, and to exhibit diurnal variation.

$$q(x, z, t) = q_0 \frac{a^2}{x^2 + a^2} e^{-z/h} \operatorname{Re}\{e^{i\Omega t}\}, \quad (4.5)$$

where q_0 is the magnitude of the thermal forcing, a is the half-width of the bell-shaped function, h is the e -folding thermal forcing depth, and Ω is the angular frequency of the diurnal variation.

Combining the above governing equations into a single equation for the perturbation vertical velocity yields

$$\left(\frac{\partial}{\partial t} + U \frac{\partial}{\partial x} + \nu \right)^2 \frac{\partial^2 w}{\partial z^2} + N^2 \frac{\partial^2 w}{\partial x^2} = \frac{g}{c_p T_0} \frac{\partial^2 q}{\partial x^2}. \quad (4.6)$$

Taking the Fourier transform in x ($\rightarrow k$) and t ($\rightarrow \omega$) upon (4.6) gives

$$\frac{d^2 \hat{w}}{dz^2} + N^2 \lambda^2 \hat{w} = \frac{g}{c_p T_0} \lambda^2 \hat{q}, \quad (4.7)$$

where

$$\lambda = \frac{k}{(\omega + Uk) - i\nu}, \quad \hat{q}(k, z, \omega) = q_0 a e^{-ak} e^{-z/h} \frac{\delta(\omega - \Omega) + \delta(\omega + \Omega)}{2}.$$

Here, δ is the delta function.

The general solution of (4.7) is

$$\hat{w}(k, z, \omega) = A(k, \omega)e^{iN\lambda z} + B(k, \omega)e^{-iN\lambda z} + \frac{\lambda^2 h^2}{1 + N^2 \lambda^2 h^2} \frac{g}{c_p T_0} \hat{q}. \quad (4.8)$$

Two unknown coefficients $A(k, \omega)$ and $B(k, \omega)$ are determined by imposing a flat bottom boundary condition [$\hat{w} = 0$ at $z = 0$] and an upper radiation condition [$B(k, \omega) = 0$ for $U \geq 0$]. Then, the solution in transformed space becomes

$$\hat{w}(k, z, \omega) = C \frac{\lambda^2}{1 + N^2 \lambda^2 h^2} e^{-ak} \frac{\delta(\omega - \Omega) + \delta(\omega + \Omega)}{2} (e^{-z/h} - e^{iN\lambda z}), \quad (4.9)$$

where

$$C = \frac{g}{c_p T_0} q_0 a h^2.$$

The solution for the perturbation vertical velocity in physical space for thermal forcing (5) is obtained by taking the inverse Fourier transform in k ($\rightarrow x$) and ω ($\rightarrow t$) upon (4.9):

$$w(x, z, t) = \frac{C}{2} \operatorname{Re} \left\{ \int_0^\infty \left[\frac{\lambda_+^2}{1 + N^2 \lambda_+^2 h^2} (e^{-z/h} - e^{iN\lambda_+ z}) e^{i\Omega t} + \frac{\lambda_-^2}{1 + N^2 \lambda_-^2 h^2} (e^{-z/h} - e^{iN\lambda_- z}) e^{-i\Omega t} \right] e^{-ak} e^{ikx} dk \right\}, \quad (4.10)$$

where

$$\lambda_+ = \frac{k}{(\Omega + Uk) - iv}, \quad \lambda_- = \frac{k}{(-\Omega + Uk) - iv}.$$

Evaluating the real part of (10) gives

$$w(x, z, t) = \frac{C}{2} \int_0^\infty k^2 e^{-ak} \left\{ X_R \left[e^{-z/h} \cos(kx + \Omega t) - e^{-\gamma z} \cos(kx + mz + \Omega t) \right] - X_I \left[e^{-z/h} \sin(kx + \Omega t) - e^{-\gamma z} \sin(kx + mz + \Omega t) \right] + X_R' \left[e^{-z/h} \cos(kx - \Omega t) - e^{-\gamma' z} \cos(kx + m'z - \Omega t) \right] - X_I' \left[e^{-z/h} \sin(kx - \Omega t) - e^{-\gamma' z} \sin(kx + m'z - \Omega t) \right] \right\} dk, \quad (4.11)$$

where

$$X_R = \frac{(\Omega + Uk)^2 + N^2 h^2 k^2 - v^2}{\left[(\Omega + Uk)^2 + N^2 h^2 k^2 - v^2 \right]^2 + 4v^2 (\Omega + Uk)^2},$$

$$X_I = \frac{2v(\Omega + Uk)}{\left[(\Omega + Uk)^2 + N^2 h^2 k^2 - v^2 \right]^2 + 4v^2 (\Omega + Uk)^2},$$

$$X_R' = \frac{(\Omega - Uk)^2 + N^2 h^2 k^2 - v^2}{\left[(\Omega - Uk)^2 + N^2 h^2 k^2 - v^2 \right]^2 + 4v^2 (\Omega - Uk)^2},$$

$$X_I' = \frac{-2v(\Omega - Uk)}{\left[(\Omega - Uk)^2 + N^2 h^2 k^2 - v^2 \right]^2 + 4v^2 (\Omega - Uk)^2},$$

$$\gamma = \frac{Nkv}{(\Omega + Uk)^2 + v^2}, \quad m = \frac{Nk(\Omega + Uk)}{(\Omega + Uk)^2 + v^2},$$

$$\gamma' = \frac{Nkv}{(\Omega - Uk)^2 + v^2}, \quad m' = \frac{-Nk(\Omega - Uk)}{(\Omega - Uk)^2 + v^2}.$$

The solutions for the perturbation horizontal velocity, perturbation buoyancy, and perturbation kinematic pressure can be obtained using (4.11) and the transformed equations of (4.1)–(4.4). These are, respectively, given by

$$\begin{aligned} u(x, z, t) = & \frac{C}{2} \int_0^\infty k e^{-ak} \left\{ X_R \left[h^{-1} e^{-z/h} \sin(kx + \Omega t) \right. \right. \\ & + e^{-\gamma z} \left\{ m \cos(kx + mz + \Omega t) - \gamma \sin(kx + mz + \Omega t) \right\} \\ & + X_I \left[h^{-1} e^{-z/h} \cos(kx + \Omega t) \right. \\ & - e^{-\gamma z} \left\{ m \sin(kx + mz + \Omega t) + \gamma \cos(kx + mz + \Omega t) \right\} \\ & + X_R' \left[h^{-1} e^{-z/h} \sin(kx - \Omega t) \right. \\ & + e^{-\gamma' z} \left\{ m' \cos(kx + m'z - \Omega t) - \gamma' \sin(kx + m'z - \Omega t) \right\} \\ & + X_I' \left[h^{-1} e^{-z/h} \cos(kx - \Omega t) \right. \\ & \left. \left. - e^{-\gamma' z} \left\{ m' \sin(kx + m'z - \Omega t) + \gamma' \cos(kx + m'z - \Omega t) \right\} \right\} \right] dk, \end{aligned} \quad (4.12)$$

$$\begin{aligned}
b(x, z, t) = & -\frac{C}{2} \int_0^\infty k e^{-ak} \left\{ Y_R \left[h^{-2} e^{-z/h} \cos(kx + \Omega t) \right. \right. \\
& + e^{-\gamma z} \left\{ (m^2 - \gamma^2) \cos(kx + mz + \Omega t) - 2m\gamma \sin(kx + mz + \Omega t) \right\} \\
& - Y_I \left[h^{-2} e^{-z/h} \sin(kx + \Omega t) \right. \\
& + e^{-\gamma z} \left\{ (m^2 - \gamma^2) \sin(kx + mz + \Omega t) + 2m\gamma \cos(kx + mz + \Omega t) \right\} \\
& + Y_R' \left[h^{-2} e^{-z/h} \cos(kx - \Omega t) \right. \\
& + e^{-\gamma' z} \left\{ (m'^2 - \gamma'^2) \cos(kx + m'z - \Omega t) - 2m'\gamma' \sin(kx + m'z - \Omega t) \right\} \left. \right] \\
& - Y_I' \left[h^{-2} e^{-z/h} \sin(kx - \Omega t) \right. \\
& \left. \left. + e^{-\gamma' z} \left\{ (m'^2 - \gamma'^2) \sin(kx + m'z - \Omega t) + 2m'\gamma' \cos(kx + m'z - \Omega t) \right\} \right] \right\} dk,
\end{aligned}
\tag{4.13}$$

$$\begin{aligned}
\pi(x, z, t) = & \frac{C}{2} \int_0^\infty k e^{-ak} \left\{ Y_R \left[h^{-1} e^{-z/h} \cos(kx + \Omega t) \right. \right. \\
& - e^{-\gamma z} \left\{ m \sin(kx + mz + \Omega t) + \gamma \cos(kx + mz + \Omega t) \right\} \left. \right] \\
& - Y_I \left[h^{-1} e^{-z/h} \sin(kx + \Omega t) \right. \\
& + e^{-\gamma z} \left\{ m \cos(kx + mz + \Omega t) - \gamma \sin(kx + mz + \Omega t) \right\} \left. \right] \\
& + Y_R' \left[h^{-1} e^{-z/h} \cos(kx - \Omega t) \right. \\
& + e^{-\gamma' z} \left\{ m' \sin(kx + m'z - \Omega t) - \gamma' \cos(kx + m'z - \Omega t) \right\} \left. \right] \\
& + Y_I' \left[h^{-1} e^{-z/h} \sin(kx - \Omega t) \right. \\
& \left. \left. - e^{-\gamma' z} \left\{ m' \cos(kx + m'z - \Omega t) + \gamma' \sin(kx + m'z - \Omega t) \right\} \right] \right\} dk,
\end{aligned}
\tag{4.14}$$

where

$$Y_R = Y_R' = \nu X_R - \Omega X_I, \quad Y_I = -Y_I' = \Omega X_R + \nu X_I.$$

The integration with respect to k in (4.11)–(4.14) are evaluated numerically using the forward scheme.

4.1.2 Parameter settings

The specified forcing (4.5) produces thermally induced circulation/flow, and the interactions of urban breeze circulation with mountain slope winds can be examined by analyzing the solution obtained by the superposition of a solution for the case of urban breeze circulation and a solution for the case of mountain slope winds. Solutions for individual cases are the same [given by (4.11)–(4.14)] but with some different parameter values suitable for individual cases. The thermal forcing that induces urban breeze circulation (mountain slope winds) is supposed to have a steady component and a diurnally varying component. Then, the solution for the perturbation vertical velocity is expressed by

$$w(x, z, t) = [q_{us} w_{us}(x - c_u, z, t - \tau_u) + q_{ud} w_{ud}(x - c_u, z, t - \tau_u) + q_{ms} w_{ms}(x - c_m, z, t - \tau_m) + q_{md} w_{md}(x - c_m, z, t - \tau_m)]. \quad (4.15)$$

Here, w_{us} and w_{ud} are the perturbation vertical velocities corresponding to a steady thermal forcing component and a diurnally varying thermal forcing

component, respectively, for the case of urban breeze circulation. The magnitudes of steady and diurnally varying thermal forcings for the case of urban breeze circulation are denoted by q_{us} and q_{ud} , respectively. w_{ms} and w_{md} are the perturbation vertical velocities corresponding to steady and diurnally varying thermal forcing components, respectively, for the case of mountain slope winds. The magnitudes of steady and diurnally varying thermal forcings for the case of mountain slope winds are denoted by q_{ms} and q_{md} , respectively. c_u (c_m) is the center of thermal forcing for the case of urban breeze circulation (mountain slope winds), and τ_u (τ_m) is the time of the maximum thermal forcing for the case of urban breeze circulation (mountain slope winds).

An urban area (mountain area) is mainly located from $x = 0$ to 20 km (from $x = -20$ to 0 km). Parameter values specified are $c_u = 10$ km, $c_m = -10$ km, $\tau_u = 1700$ LT, $\tau_m = 1400$ LT, $a_u = a_m = 5$ km [half-width of thermal forcing, subscript u (m) denoting the urban (mountain)], $N = 0.01$ s⁻¹, and $T_0 = 283$ K. The values of τ_u and τ_m are chosen based on the results of section 3.2. Note that the angular frequency of the steady thermal forcing component is 0 s⁻¹ and that of the diurnally varying thermal forcing component is $2\pi/(24$ h).

Figure 4.1 shows the temporal variations of urban thermal forcing at $x = c_u$ and $z = 0$ km and mountain thermal forcing at $x = c_m$ and $z = 0$ km.

Here, $q_{us} = 0.20$, $q_{ud} = 0.15$, $q_{ms} = 0.05$, and $q_{md} = 0.20 \text{ J kg}^{-1} \text{ s}^{-1}$ are used. Urban breeze circulation is induced by the temporally varying positive thermal forcing (heating) in the urban area. Mountain slope winds are induced by the temporally varying positive/negative thermal forcing (heating/cooling) in the mountain area. Although not included in the present theoretical study, the topographical structure can also affect mountain slope winds. Recently, Kirshbaum (2013) compared the circulation induced by horizontally varying surface heating over Gaussian terrain with the circulation induced by localized heating over flat terrain. The analysis results indicate that the circulation induced by heating over flat terrain can reproduce the circulation induced by surface heating over Gaussian terrain. The finding of Kirshbaum (2013) provides a justification for imposing heating/cooling only in the present study, although a further study that includes topographic effect is needed.

This study considers no-basic state wind. Under this condition, ν should be positive to get a physical solution to steady thermal forcing component because γ and γ' in exponents in (4.11) become infinite in an inviscid system. In this study, $\nu = 1/7200 \text{ s}^{-1}$ is chosen. The e -folding depth of thermal forcing is determined to have a height of maximum vertical velocity similar to that in the previous section: $h = 750 \text{ m}$ for the case of urban breeze circulation and $h = 500 \text{ m}$ for the case of mountain slope winds.

Seven cases with different thermal forcing magnitudes are examined in sections 4.3.1 and 4.3.2. Table 4.1 lists names and thermal forcing magnitudes for individual cases. Hereafter, for brevity, the perturbation vertical velocity, perturbation horizontal velocity, perturbation velocity vector, perturbation buoyancy, and perturbation kinematic pressure are designated as the vertical velocity, horizontal velocity, velocity vector, buoyancy, and kinematic pressure, respectively.

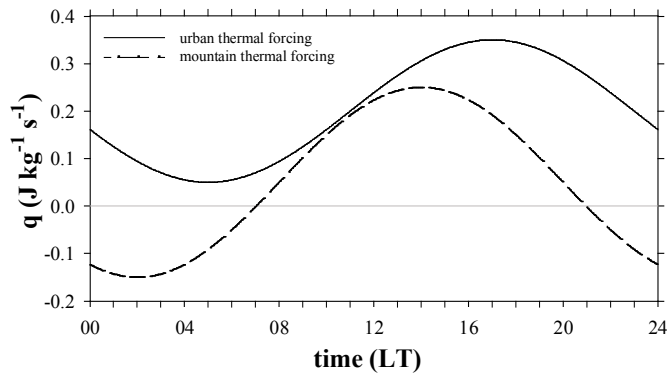


Figure 4.1. Temporal variations of urban thermal forcing at $x = c_u$ and $z = 0$ km (solid line) and mountain thermal forcing at $x = c_m$ and $z = 0$ km (dashed line).

Table 4.1. Names and thermal forcing magnitudes for eight cases (unit: J kg⁻¹ s⁻¹)

CASE	q_{us}	q_{ud}	q_{ms}	q_{md}
URBAN	0.20	0.15	0	0
MOUNT	0	0	0.05	0.20
URBAN-MOUNT	0.20	0.15	0.05	0.20
URBAN+	0.30	0.225	0.05	0.20
URBAN-	0.10	0.075	0.05	0.20
MOUNT+	0.20	0.15	0.075	0.30
MOUNT-	0.20	0.15	0.025	0.10

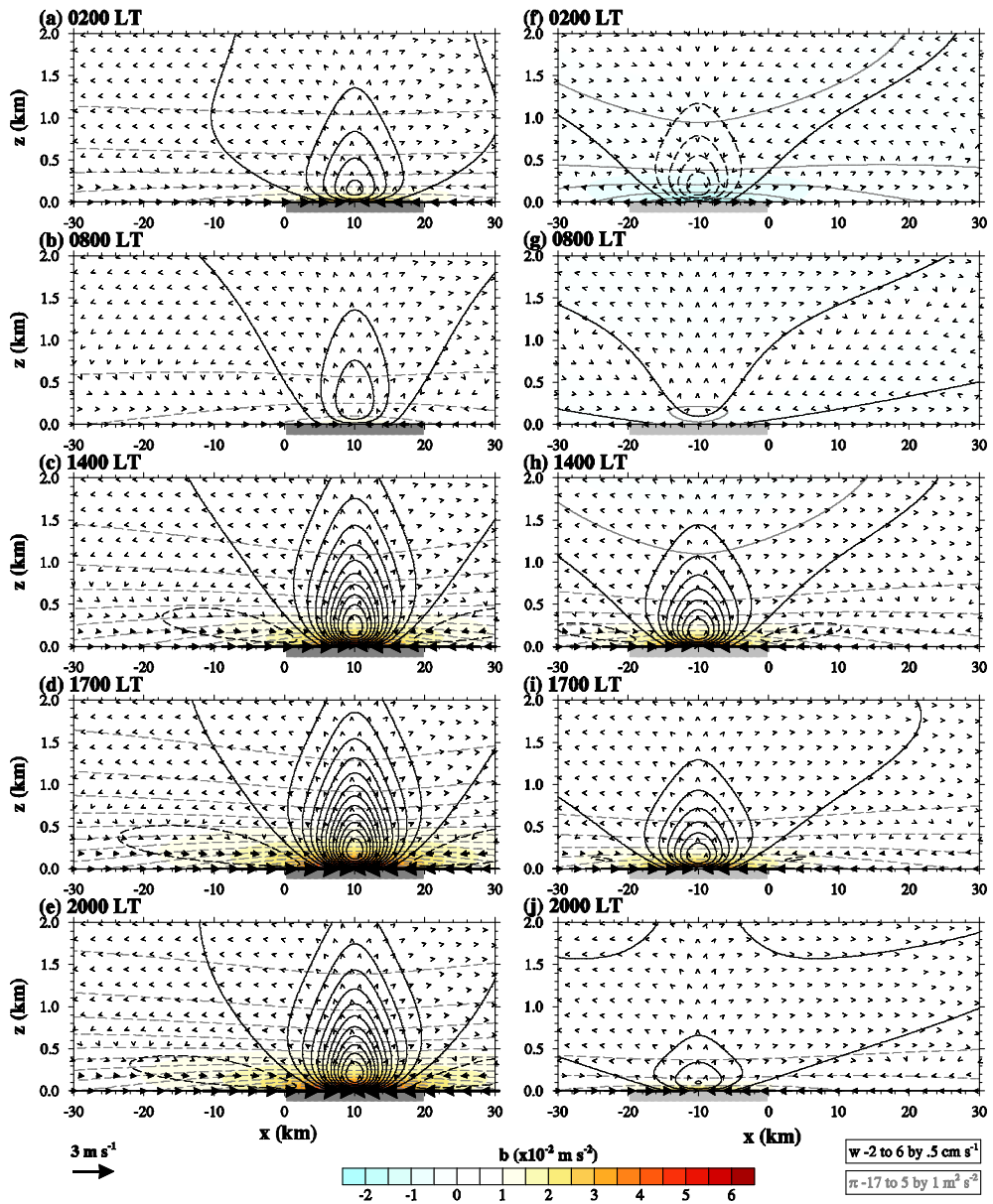


Figure 4.2. Kinematic pressure (gray dashed contour), buoyancy (shaded), vertical velocity (black contour), and velocity vector fields at (a) and (f) 0200, (b) and (g) 0800, (c) and (h) 1400, (d) and (i) 1700, and (e) and (j) 2000 LT in the URBAN (left) and MOUNT (right) cases. The dark gray

(gray) box on the x -axis (also, in Figs. 4.4–4.6) indicates the urban (mountain) area.

4.2 Results and discussion

4.2.1 Urban breeze circulation and mountain slope winds

Figure 4.2a–e shows the kinematic pressure, buoyancy, vertical velocity, and velocity vector fields at 0200, 0800, 1400, 1700, and 2000 LT in the URBAN case with $q_{us} = 0.20$, $q_{ud} = 0.15$, $q_{ms} = 0$, and $q_{md} = 0 \text{ J kg}^{-1} \text{ s}^{-1}$. At 0200 LT, the low pressure and positive buoyancy centered at $x = 10 \text{ km}$ and $z = 0 \text{ km}$ drive low-level converging flows toward the urban center and relatively strong upward motion there. There appear weak upper-level diverging flows and weak downward motion outside the urban area. At 0800 LT, the urban breeze circulation is very weak. The urban breeze circulation intensifies and the layer of low-level converging flows becomes thick (Figs. 4.2c,d) as the urban heating increases (Fig. 4.1). At 1700 LT, the horizontal size of the urban breeze circulation is 2.9 times the urban size and its vertical size is 2.2 km. Here, the horizontal (vertical) size of the urban breeze circulation is determined as the horizontal (vertical) extent where the surface horizontal velocity (the vertical velocity) is larger than 0.2 (0.1) times its maximum value. At 2000 LT, the urban breeze circulation is still strong.

Figure 4.2f–j shows the kinematic pressure, buoyancy, vertical velocity, and velocity vector fields at 0200, 0800, 1400, 1700, and 2000 LT in the MOUNT case with $q_{us} = 0$, $q_{ud} = 0$, $q_{ms} = 0.05$, and $q_{md} = 0.20 \text{ J kg}^{-1} \text{ s}^{-1}$. Note that cooling exists from 2100 to 0700 LT and heating exists from 0700 to 2100 LT (Fig. 4.1). Unlike the urban breeze circulation, since the mountain thermal forcing changes its sign twice a day, the mountain slope wind also changes its direction twice a day. At 0200 LT, the high pressure and negative buoyancy centered at $x = -10 \text{ km}$ and $z = 0 \text{ km}$ drive low-level diverging flows away from the mountain center and relatively strong downward motion there. There appear upper-level converging flows and weak upward motion outside the mountain area. These features are different from those of the urban breeze circulation (Fig. 4.2a,f). At 0800 LT, the mountain circulation is very weak. At 1400 and 1700 LT, circulation features are similar to those of urban breeze circulation (Fig. 4.2c,d,h,i). At 2000 LT, the mountain circulation is weak. It is physically meant that diverging (converging) flows in the mountain area are downslope (upslope) winds. The transition from the upslope wind to downslope wind at a mid-slope location ($x = -5 \text{ km}$) occurs at 2313 LT. The occurrence frequency of the downslope (upslope) wind at the mid-slope location is 42% (58%) during the 24-h period.

Figure 4.3 shows the temporal variations of the maximum horizontal velocity in the entire domain (u_{\max}) and w_m in $0 \text{ km} \leq x \leq 20 \text{ km}$ and $-20 \text{ km} \leq x \leq 0 \text{ km}$. Here, w_m is taken as the largest value between the maximum and minimum vertical velocities keeping its sign. Different temporal variations in

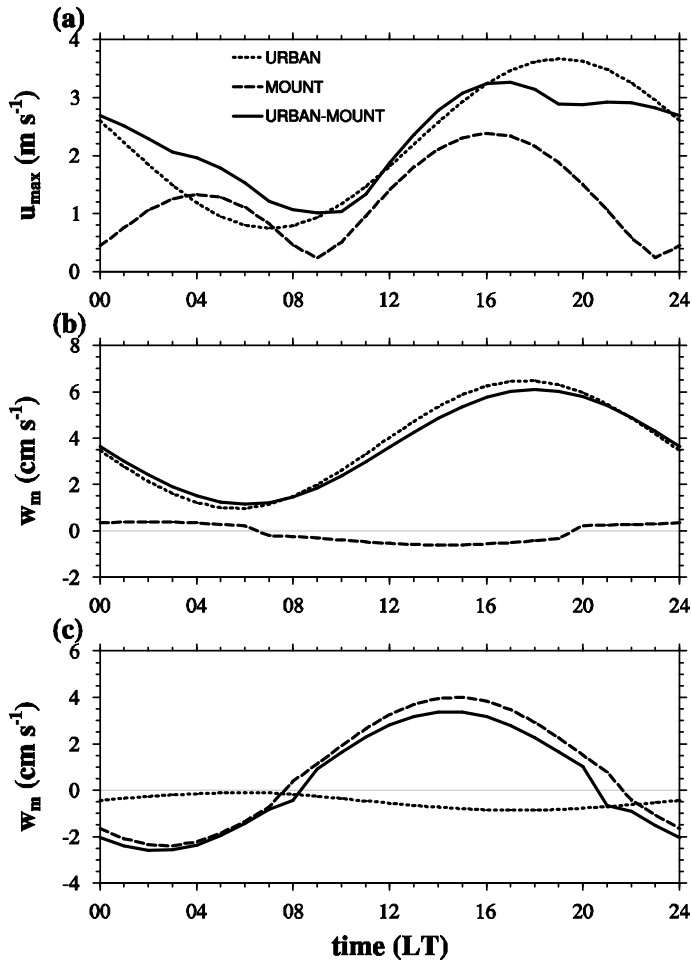


Figure 4.3. Temporal variations of (a) the maximum horizontal velocity in the entire domain and w_m in (b) $0 \text{ km} \leq x \leq 20 \text{ km}$ and (c) $-20 \text{ km} \leq x \leq 0 \text{ km}$ in the URBAN (short-dashed lines), MOUNT (dashed lines), URBAN-MOUNT (solid lines) cases.

u_{\max} and w_m in the URBAN and MOUNT cases are associated with different temporal variations of thermal forcing. A lag exists between the time of the strongest thermal forcing and maximal u_{\max} or w_m (Fig. 4.3). In both URBAN and MOUNT cases, the time lag is larger for maximal u_{\max} than for the maximal w_m . In the URBAN case, the maximal u_{\max} occurs 2 h 2 min later than the strongest heating. In the MOUNT case, there are two maxima in u_{\max} . Both the two maxima in u_{\max} occurs 2 h 11 min later than the strongest daytime heating (nighttime cooling). The urban heating induces upward motion in the urban area (Fig. 4.3b), while the mountain heating (cooling) induces upward (downward) motion in the mountain area (Fig. 4.3c). Weaker buoyancy in the MOUNT case than in the URBAN case results in smaller w_m . The lag between the time of the strongest heating and the time of maximal w_m is 36 min in the URBAN case and 43 min in the MOUNT case. The lag between the time of the strongest cooling and the time of minima in w_m in the MOUNT case is 43 min. Figure 4.4 shows the distance–time sections of the horizontal velocity at the surface and the vertical velocity at $z = 200$ m. In each of the URBAN and MOUNT cases, the horizontal velocity is anti-symmetric and the vertical velocity is symmetric about the thermal forcing center. In the URBAN case, at ~0700 LT, the urban breeze circulation is weakest in horizontal velocity and its

horizontal size is smallest (Fig. 4.4a). The horizontal velocity is strongest at 1902 LT (3.7 m s^{-1}). The vertical

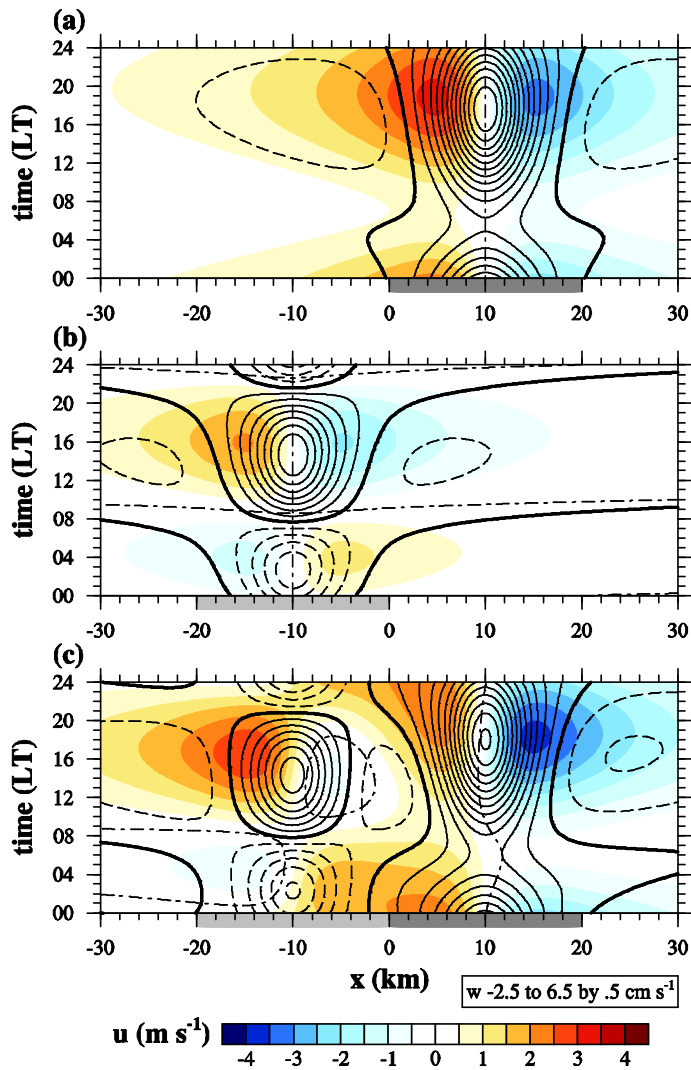


Figure 4.4. Distance-time sections of the horizontal velocity (shaded) at the surface and the vertical velocity (solid and dashed lines) at $z = 200$ m in the (a) URBAN, (b) MOUNT, and (c) URBAN-MOUNT cases. Dashed lines indicate the negative vertical velocity. Bold solid and dashed-short dashed lines indicate the zero vertical and horizontal velocity, respectively.

velocity is strongest at 1736 LT (6.5 cm s^{-1}). In the MOUNT case, the magnitude of the mountain heating is larger than that of the mountain cooling, thus producing stronger converging flows/upslope winds in the daytime than diverging flows/downslope winds in the nighttime (Fig. 4.4b). The maximum (minimum) vertical velocity of 4.0 (-2.4) cm s^{-1} occurs at 1443 (0243) LT.

4.2.2 Interactions of urban breeze circulation with mountain slope winds

For brevity, following terminologies (section 3) are used: mountain-side urban area (from $x = 0$ to 10 km), plain-side urban area (from $x = 10$ to 20 km), urban-side mountain slope (from $x = -10$ to 0 km), rural-side mountain slope (from $x = -20$ to -10 km), urban-side mid-slope location ($x = -5$ km), mountain–urban edge ($x = 0$ km), and urban–rural edge ($x = 20$ km). Figure 4.5 shows the kinematic pressure, buoyancy, vertical velocity, and velocity vector fields at 0200, 0800, 1100, 1400, 1700, and 2000 LT in the URBAN-MOUNT case with $q_{us} = 0.20$, $q_{ud} = 0.15$, $q_{ms} = 0.05$, and $q_{md} = 0.20 \text{ J kg}^{-1} \text{ s}^{-1}$. At 0200 LT, positive (negative) buoyancy in the urban (mountain) area is responsible for surface converging (diverging) flows and upward (downward) motion there. Larger pressure gradient between the

urban and mountain areas produces stronger winds on the urban-side
mountain slope

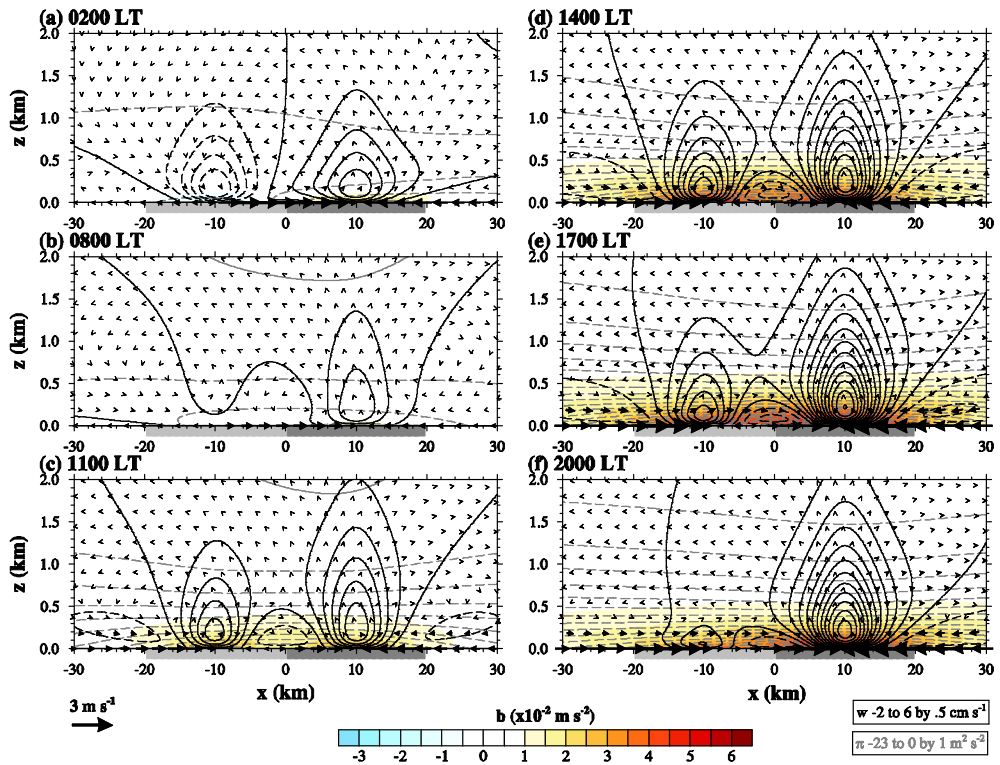


Figure 4.5. Kinematic pressure (gray lines), buoyancy (shaded), vertical velocity (black lines), and velocity vector fields at (a) 0200, (b) 0800, (c) 1100, (d) 1400, (e) 1700, and (f) 2000 LT in the URBAN-MOUNT case.

than on the rural-side mountain slope and stronger winds in the mountain-side urban area than in the plain-side urban area. Converging flows toward the urban center weaken the negative horizontal velocity on the rural-side mountain slope, and diverging flows away from the mountain center weaken the negative horizontal velocity in the plain-side urban area. At 0800 LT, the downslope wind on the urban-side mountain slope is maintained. As the buoyancy in the mountain area becomes positive and strong with time, the converging flows induced by the urban heating and those induced by the mountain heating effectively interfere with each other in the region between $x = -10$ and 10 km, producing weakened upslope winds on the urban-side mountain-slope (Fig. 4.5c). At 1400 and 1700 LT, the upslope wind on the urban-side mountain slope is apparent but weaker than that on the rural-side mountain slope. Moreover, the upslope wind on the urban-side mountain slope is much weaker than the upslope wind in the MOUNT case (Fig. 4.5d,e and 4.2h,i). At the urban-side mid-slope location, the maximum upslope wind is 0.9 m s^{-1} at 1440 LT (2.4 m s^{-1} at 1607 LT in the MOUNT case) and the transition from the upslope wind to downslope wind occurs at 1906 LT (4 h 7 min earlier than in the MOUNT case). At 2000 LT, winds on the mountain slope are toward the urban area. At the urban-side mid-slope location, the occurrence frequency of the downslope (upslope) wind increases (decreases) with its value of 63% (37%) in comparison with the

MOUNT case due to the interactions of urban breeze circulation with mountain slope winds.

Two features are reflected in the time variation of the maximum horizontal velocity in the URBAN-MOUNT case (Fig. 4.3a). From 0300 to 1900 LT, the maximum horizontal velocity shows a time variation similar to that in the URBAN case. During this period, the maximum horizontal velocity is mostly led by the converging flows induced by the urban heating. From 1900 to 0300 LT, the downslope wind strengthens (weakens) converging flows toward the urban center in the mountain-side (plain-side) urban area. Because of this, the maximum horizontal velocity occurs between the two thermal forcing centers during this period and decreases with time due to the weakening of the urban heating in the nighttime. In the urban area, w_m follows the time variation of the thermal forcing, similar to the URBAN case (Fig. 4.3b). Weaker downward (upward) motion beside stronger upward (downward) motion induced by the mountain thermal forcing in the daytime (nighttime) weakens (strengthens) w_m in the daytime (nighttime) as compared with the URBAN case. As compared with the MOUNT case, in the mountain area, downward motion induced by the urban heating leads to weaker daytime upward motion and stronger nighttime downward motion (Fig. 4.3c).

In the URBAN-MOUNT case, flow patterns are not symmetric because of the interactions of urban breezes with mountain slope winds (Fig. 4.4c). In the nighttime, the downslope wind on the rural-side mountain slope is weakened. Furthermore, the wind in the plain-side urban area reaches its maximum intensity earlier than that in the mountain-side urban area and is weakened due to diverging flows from the mountain. Moreover, converging flows toward the urban area, which is primarily due to the urban heating, intensify the downslope wind on the urban-side mountain slope. Because of this, the downslope wind on the urban-side mountain slope in the URBAN-MOUNT case starts earlier than that in the MOUNT case. This leads to a longer persistence period of downslope wind. In the daytime, converging flows in the mountain-side urban area are weakened by the upslope wind on the urban-side mountain slope. This is consistent with the results of previous studies (e.g., Savijarvi and Liya 2001; Ohashi and Kida 2002).

4.2.3 Sensitivities to thermal forcing intensities

The sensitivities of the interactions between urban breeze circulation and mountain slope winds to urban fraction and maximum mountain height were examined in section 3.2.3. In the present section, analogous sensitivities to different magnitudes of urban and mountain thermal forcings (URBAN+, URBAN-, MOUNT+, and MOUNT- cases, Table 4.1) are

examined. In the URBAN+ (URBAN–) case, q_{us} and q_{ud} are 1.5 (0.5) times those in the URBAN-MOUNT case but q_{ms} and q_{md} are equal to those in the URBAN-MOUNT case. In the MOUNT+ (MOUNT–) case, q_{ms} and q_{md} are 1.5 (0.5) times those in the URBAN-MOUNT case but q_{us} and q_{ud} are equal to those in the URBAN-MOUNT case.

Figure 4.6 shows the kinematic pressure, buoyancy, vertical velocity, and velocity vector fields at 0200 and 1700 LT in the URBAN+, URBAN–, MOUNT+, and MOUNT– cases. In the nighttime, the downslope wind is strongly associated with the differences in kinematic pressure and buoyancy between the urban and mountain areas. At 0200 LT, the maximum horizontal velocity is 3.2 (2.5) m s^{-1} at $x = 4.9$ (–4.9) km in the URBAN+ (MOUNT+) case and 1.5 (2.1) m s^{-1} at $x = -4.9$ (5.0) km in the URBAN– (MOUNT–) case (Fig. 6a–d). The strongest wind tends to occur closer to the center of stronger thermal forcing. At 1700 LT, cancellation or enhancement of converging flows is apparent depending on the area (Fig. 6e–h). At 1700 LT, the maximum intensity of upslope wind on the rural-side mountain slope is 3.7 (2.8) m s^{-1} at $x = -14.0$ (–14.4) km in the URBAN+ (URBAN–) case and the wind in the plain-side urban area is 4.3 (3.7) m s^{-1} at $x = 14.4$ (14.6) km in the MOUNT+ (MOUNT–) case. This result indicates that the enhancement of the upslope wind on the rural-side mountain slope (wind in the plain-side urban area) is related to the heating magnitude in the urban

(mountain) area. A stagnant point, where the horizontal velocity is zero, is present between the two heating centers due to cancellation of the converging flows toward the

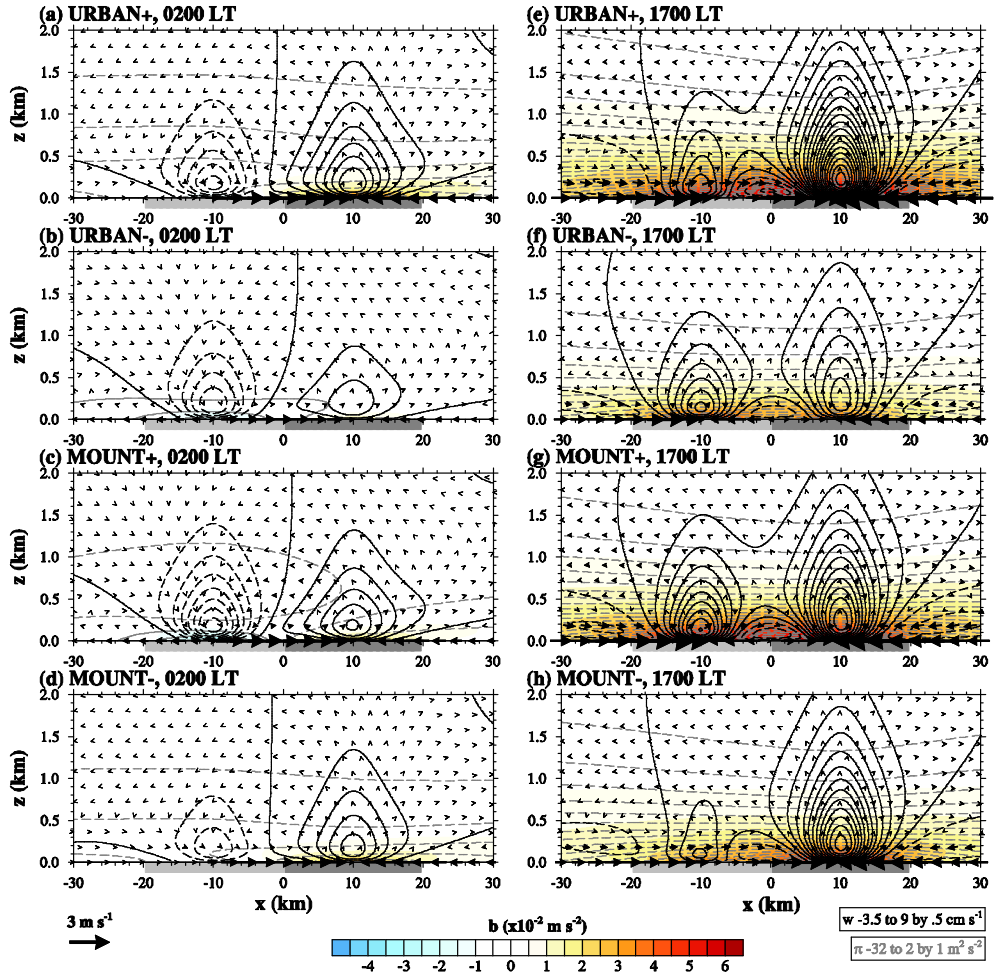


Figure 4.6. Kinematic pressure (gray lines), buoyancy (shaded), vertical velocity (black lines), and velocity vector fields at (a)–(d) 0200 and (e)–(h) 1700 LT in the URBAN+ (a and e), URBAN– (b and f), MOUNT+ (c and g), and MOUNT– (d and h) cases.

heating centers. The stagnant point or the location of u_{\min} (the minimum horizontal velocity in the entire domain) is shifted depending on the heating magnitude and located closer to the center of weaker heating. The stagnant points are located at $x = -2.6, 1.8,$ and 0.0 km in the URBAN-MOUNT, URBAN–, and MOUNT+ cases, respectively. In the URBAN+ and MOUNT– cases, the stagnant points do not exist because converging flows toward the urban heating center are much stronger than converging flows toward the mountain heating center due to the strong urban heating magnitude.

The dependencies of the interactions of urban breeze circulation with mountain slope winds on thermal forcing intensities are examined further. Figure 4.7 shows the maximum intensities of the horizontal velocity at the mountain–urban and urban–rural edges and the transition time from the upslope wind to downslope wind and the percentage of the occurrence frequency of downslope wind at the urban-side mid-slope location as a function of the ratios of thermal forcing magnitudes. Here, R_u (R_m) indicates the ratio of each magnitude of the urban (mountain) thermal forcing in any case to that in the URBAN-MOUNT case.

The maximum intensity of the horizontal velocity (u_{\max}) at the mountain–urban edge as a function of R_u and R_m is depicted in Fig. 4.7a. In Fig. 4.7a, the gray solid line ($R_m=4.35R_u$) indicates zero u_{\max} . u_{\max} has

negative sign in the area of $R_m > 4.35R_u$ and positive sign in the area of $R_m < 4.35R_u$. In both areas, u_{\max} increases with R_u for given R_m . Moreover, the area of $R_m \leq 4.35R_u$ can be divided into two areas by the gray dashed curve (Fig. 4.7a). In the area below the gray dashed curve, u_{\max} decreases with increasing R_m for given R_u due to intensified upslope winds in the daytime. In the area above the gray dashed curve, u_{\max} increases with increasing R_m for given R_u . This maximum intensity occurs in the nighttime due to the strong downslope winds induced by cooling in the mountain area. At the urban–rural edge, the sensitivity of u_{\max} to R_u is large for given R_m , whereas that to R_m for given R_u is small (Fig. 4.7b). The maximum intensity of the horizontal velocity linearly increases with R_u and R_m ($|u|_{x=20 \text{ km}} = 2.7R_u + 0.4R_m$).

The transition from the upslope wind to downslope wind at the urban-side mid-slope location occurs when $R_m > 0.58R_u$ (Fig. 4.7c). For $R_m < 0.58R_u$ (dotted area in Fig. 4.7c), the upslope wind does not exist at the urban-side mid-slope location during the 24-h period. The transition from the upslope wind to downslope wind occurs earlier for larger R_u and smaller R_m . For given R_m (R_u), the transition from the upslope wind to downslope wind starts earlier as R_u increases (R_m decreases). The sensitivity of the occurrence frequency of downslope wind at the urban-side mid-slope location to R_u and R_m exhibits a pattern similar to that of the transition time

from the upslope wind to downslope wind (Fig. 4.7d). As the transition from the upslope wind to downslope wind occurs later, the occurrence frequency of downslope wind is small. For $R_m \leq 0.58R_u$ (dotted area in Fig. 4.7d), only the downslope wind exists at the urban-side mid-slope location during the 24-h period. The occurrence frequency of downslope wind is large for large R_u and small R_m . For given R_m (R_u), the occurrence frequency of downslope wind increases with increasing R_u (decreasing R_m).

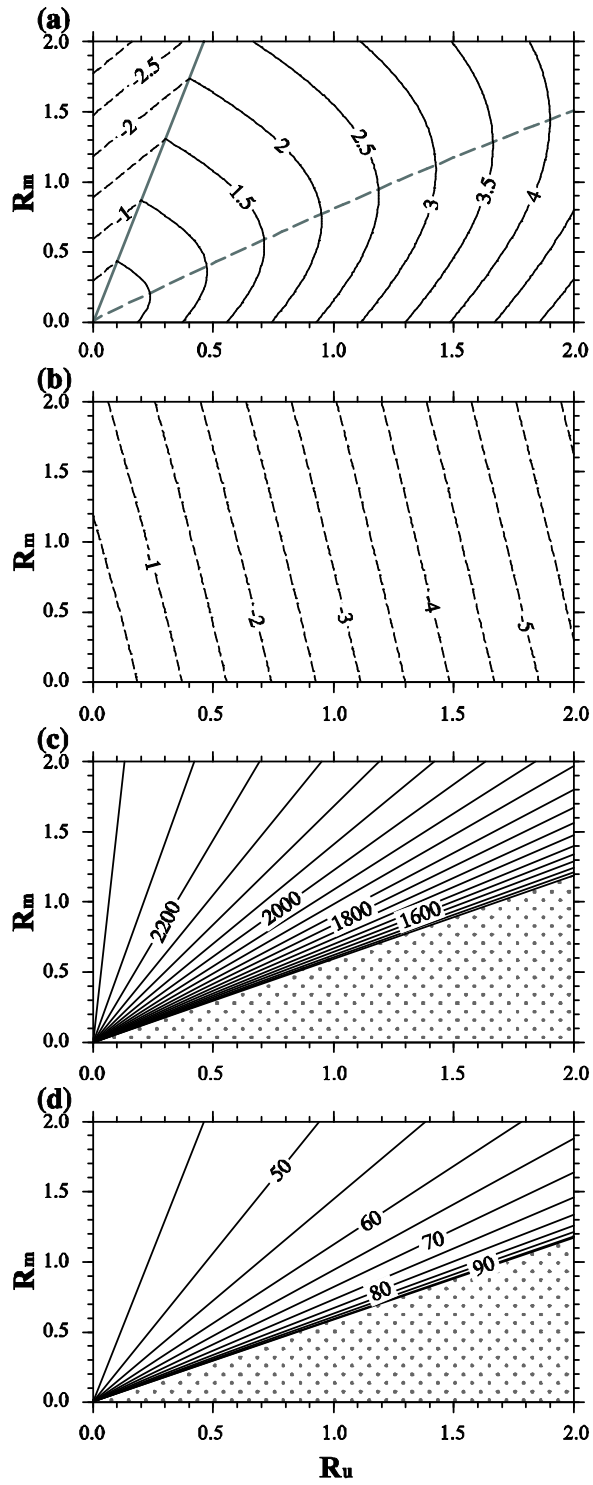


Figure 4.7. Maximum intensities of the horizontal velocity (m s^{-1}) at the (a) mountain–urban edge and (b) urban–rural edge, (c) the transition time (LT) from the upslope wind to downslope wind, and (d) the percentage of the occurrence frequency of downslope wind during the 24-h period as a function of the ratios of thermal forcing magnitudes. (c) and (d) are at the urban-side mid-slope location. The dotted area in (c) indicates that the upslope wind does not occur. The dotted area in (d) indicates 100% of the frequency of downslope wind.

5 Local circulations in the Ulaanbaatar area: Idealized simulations

In the previous sections, the numerical and theoretical investigations on the urban breeze circulations and mountain slope winds were conducted and their interactions were examined. Also, sensitivities of the interactions to several parameters were tested. Local circulations including urban breeze circulation and mountain slope/valley winds in a real topography are of great interest to understand the complex structure and behavior of the local circulations for scientific research and practical reasons. Thus, the present section investigates the local circulations in and around the Ulaanbaatar, Mongolia, metropolitan area under idealized summertime fair-weather conditions using a mesoscale model that includes an advanced urban canopy model. Sensitivities of the local circulations to urban fraction, atmospheric stability, and soil water content are examined.

5.1 Experimental design

The numerical model adopted in the present study is the Weather Research and Forecasting (WRF) model version 3.2 (Skamarock et al. 2008) coupled with the SNUUCM (Ryu et al. 2011). The model physics options

are the same to that in section 3. These are: the Yonsei University (YSU) planetary boundary layer scheme (Hong et al. 2006), the Rapid Radiative Transfer Model (RRTM) longwave radiation scheme (Mlawer et al. 1997), and the Dudhia shortwave radiation scheme (Dudhia 1989). The SNUUCM parameterizes important physical processes that occur in urban canopies, including absorption and reflection of shortwave and longwave radiation, turbulent energy and water exchanges between surfaces (road, two facing walls, and roof) and adjacent air, and conductive heat transfer through substrates (Ryu et al. 2011). The SNUUCM is coupled with the Noah land surface model (Chen and Dudhia 2001) using a tile approach.

The computational domain size is $215 \text{ km} \times 215 \text{ km}$ in the horizontal with a horizontal grid resolution of 500 m. As described in section 1.1.3, geographical feature in the study area is complex. So, the regions with outermost 30 grids are buffer regions, where the terrain height is gradually reduced from the lateral boundaries of the physical domain ($200 \text{ km} \times 200 \text{ km}$) (Fig. 5.1a) to reduce steepness at/near the lateral boundaries. The model top height is 8 km. The number of vertical layers is 83, and the lowest model level is $\sim 20 \text{ m}$. The initial temperature at the surface is 20°C , and the initial wind is calm. The lateral boundary condition is periodic. In the control simulation, the initial potential temperature lapse rate is 5 K km^{-1} ,

the initial relative humidity is 30%, and the initial volumetric soil water content is 0.17

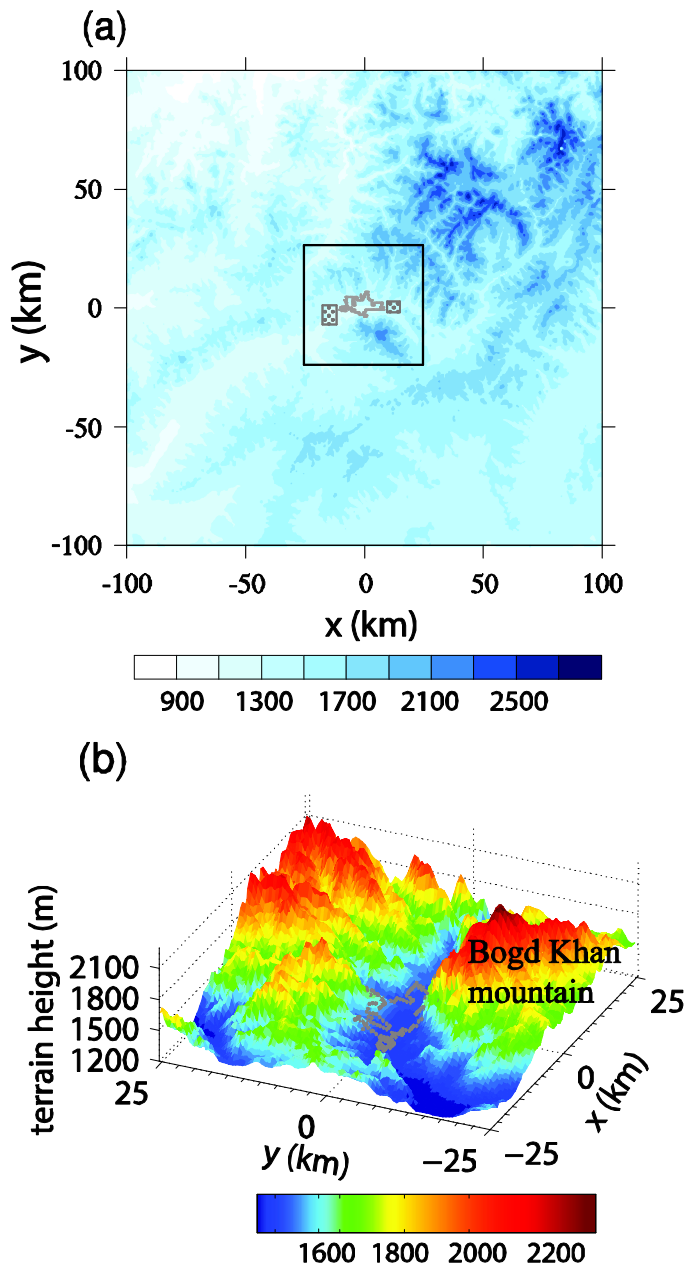


Figure 5.1. Terrain height of the (a) domain and (b) analysis area. The inner rectangle in (a) is the analysis domain. The gray lines indicate the Ulaanbaatar city boundary. The dotted boxes in (a) indicate the rural areas.

$\text{m}^3 \text{ m}^{-3}$. The Earth's rotation is included. The model is integrated for 36 h starting from 1200 LST 14 July 2013, with a time step of 1 s. Here, the year has no meaning. The results of last 24 h are used for the analysis.

The urban grid consists of built-up (70%) and natural (30%) areas. All natural areas consist of grassland (52.5%) and bare ground with sandy loam soil (47.5%). Some important urban parameters in the SNUUCM are specified as follows: the roof level height is 10 m, the aspect ratio is 0.5, and the albedos of roof, wall, and road are 0.12, 0.12, and 0.08, respectively.

Figure 5.1b shows the topographic features of the area with a size of $50 \text{ km} \times 50 \text{ km}$ centered in Ulaanbaatar which is taken for the analysis in this study (hereafter, analysis domain). The Shuttle Radar Topography Mission (SRTM) data with a resolution of $\sim 90 \text{ m}$ (Jarvis et al. 2008) are utilized for terrain data in this study. The United States Geological Survey (USGS) dataset and a combined dataset for Ulaanbaatar which includes the Moderate Resolution Imaging Spectroradiometer (MODIS) data (Friedl et al. 2002), a GlobCover land cover classifications map (Arino et al. 2010), and Google Earth imagery (Google Inc. 2013) are utilized for land-use/land-cover data.

5.2 Results and discussions

5.2.1 Control simulation

Figure 5.2 shows the diurnal variations of surface sensible heat flux, surface latent heat flux, 2-m air temperature, and atmospheric boundary-layer height averaged over the urban area (the gray line in Fig. 5.1a indicates the urban boundary) and rural areas (dotted boxes in Fig. 5.1a). Here, the rural areas, which have size and terrain height similar to those in the urban area, are chosen on the valley mouth and exit. In the daytime, the surface sensible heat flux is larger in the urban area than in the rural areas while the surface latent heat flux is smaller in the urban area than in the rural areas. This finding is consistent with the results of previous studies (e.g., Hidalgo et al. 2008b). In the urban area, the maximum surface sensible heat flux is 408 W m^{-2} at 1300 LST and the maximum surface latent heat flux is 132 W m^{-2} at 1220 LST. The larger daytime surface sensible heat flux in the urban area results in deeper daytime atmospheric boundary layer. The difference in 2-m air temperature between the urban and rural areas, which represents the urban heat island, is large in the nighttime and very small in the daytime. This feature of the simulated urban heat island is similar to that of the observed one in Ulaanbaatar (section 2.3.1). The

maximum urban heat island intensity is 5.0°C at 0350 LST. The atmospheric boundary-layer height in the urban

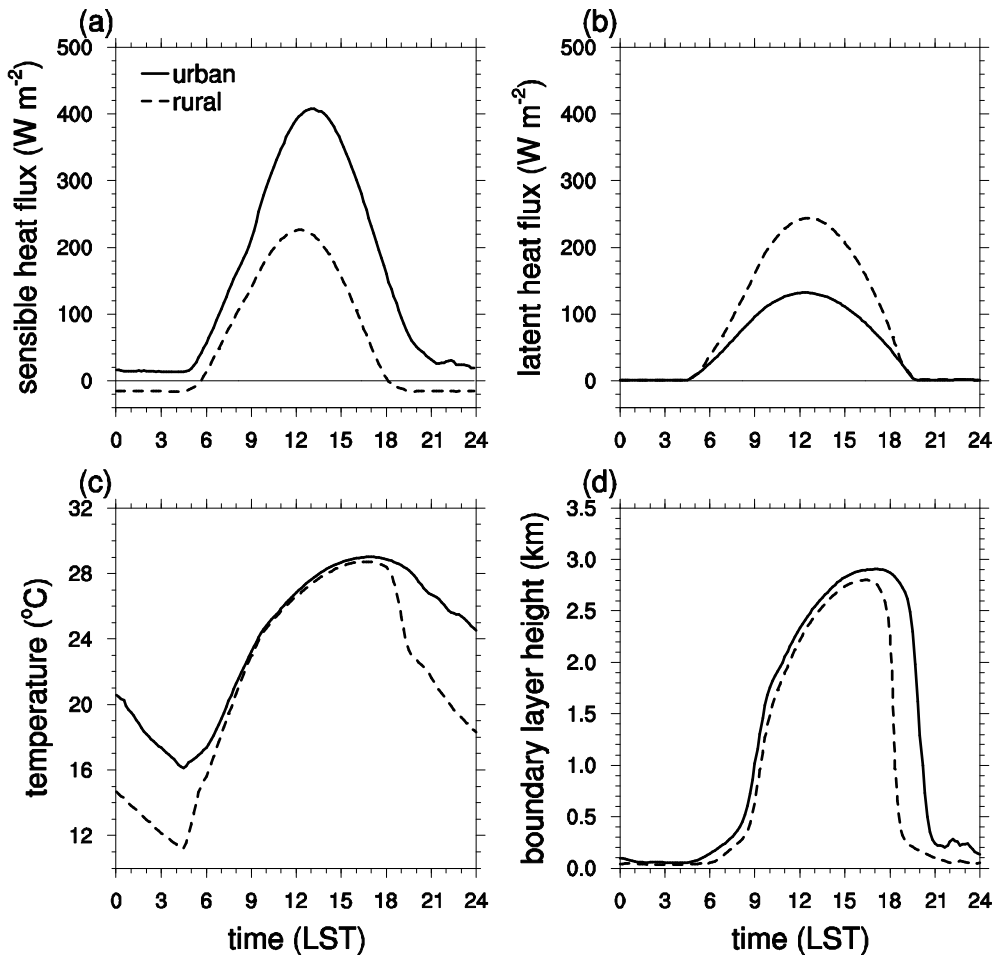


Figure 5.2. Diurnal variations of (a) surface sensible heat flux, (b) surface latent heat flux, (c) air temperature at 2 m, and (d) atmospheric boundary-layer height averaged over the urban and rural areas in the control simulation.

area (rural areas) reaches a maximum of 2906 (2802) m at 1710 (1620) LST. The simulated atmospheric boundary layer is quite deep. A few studies have reported that the atmospheric boundary layer can exceed a depth of 3 km above the surface in the arid region (Ma et al. 2011) and over the Tibetan Plateau (Chen et al. 2013).

Local circulations and their interactions are investigated through the analysis of wind fields. Figure 5.3 shows 2-m air temperature and 10-m wind vector fields at 0300, 0600, 0900, 1200, 1600, and 2100 LST. Figure 5.4 shows the vertical cross-sections of wind vector and vertical velocity along the south-north direction through the center of the analysis domain ($x = 0$ km, $y = 0$ km) at the times corresponding to Fig. 5.3. Figure 5.5 is the same as in Fig. 5.4 but for the east-west direction. It is mentioned that if the terrain is flat, only urban breeze circulation appears and mountain slope winds and up-/down-valley winds do not occur and that the urban breeze circulation is stronger in the daytime than in the nighttime. Note that the urban breeze circulation is featured by inward flow toward the center of a city in the lower atmospheric boundary layer, upward flow over the city, outward flow toward the surroundings in the upper atmospheric boundary layer, and downward flow in the surroundings (Hidalgo et al. 2010; Ryu et al. 2013b). In the presence of the terrain, urban breeze circulation, mountain

slope winds, and up-/down-valley winds are produced and interact with each other. The

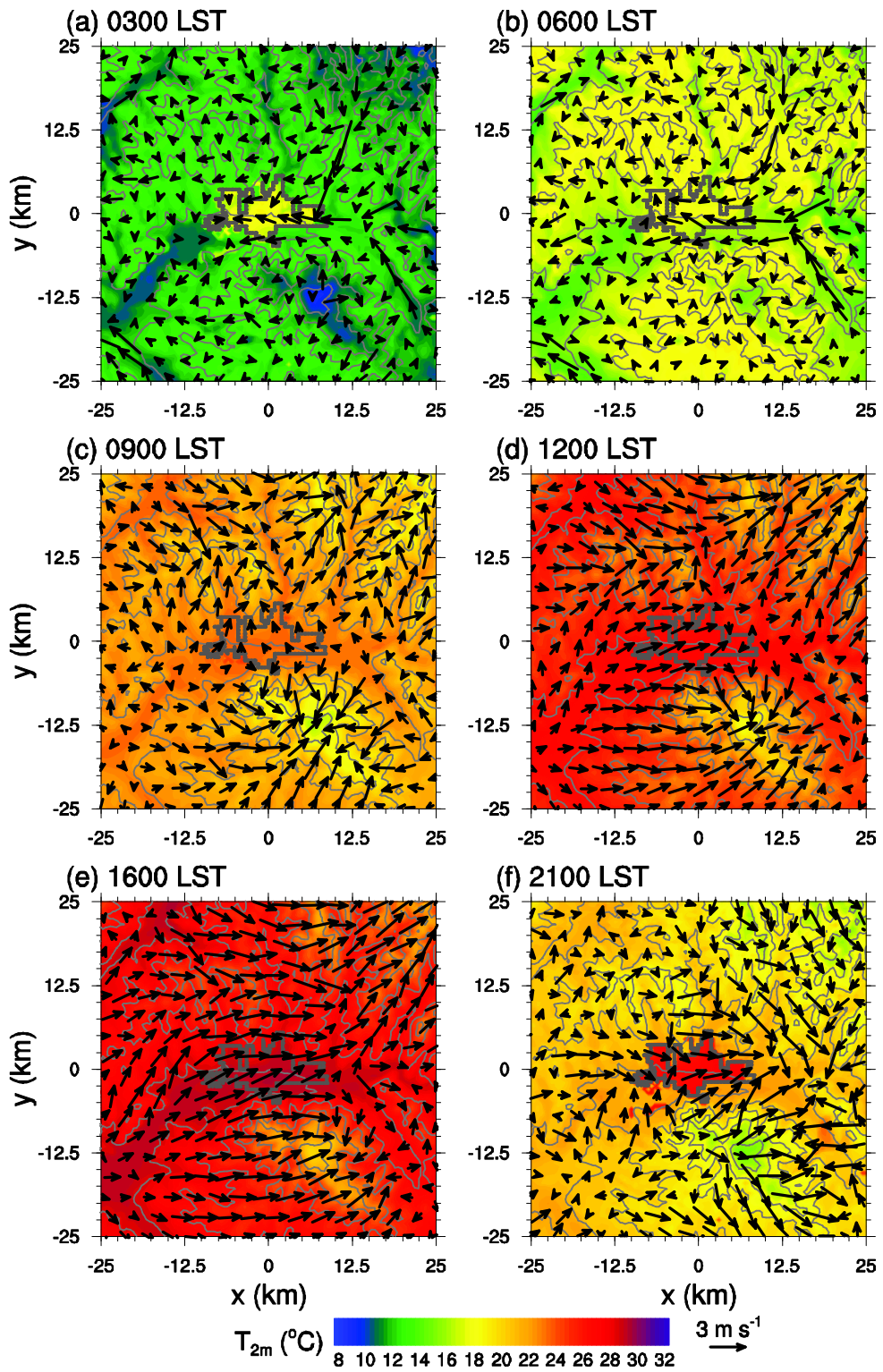


Figure 5.3. Fields of air temperature at 2 m and wind vector at 10 m at (a) 0300, (b) 0600, (c) 0900, (d) 1200, (e) 1600, and (f) 2100 LST in the control simulation. The dark gray line indicates the urban boundary. Light gray lines indicate the terrain height (from 1300 to 2100 m with intervals of 200 m).

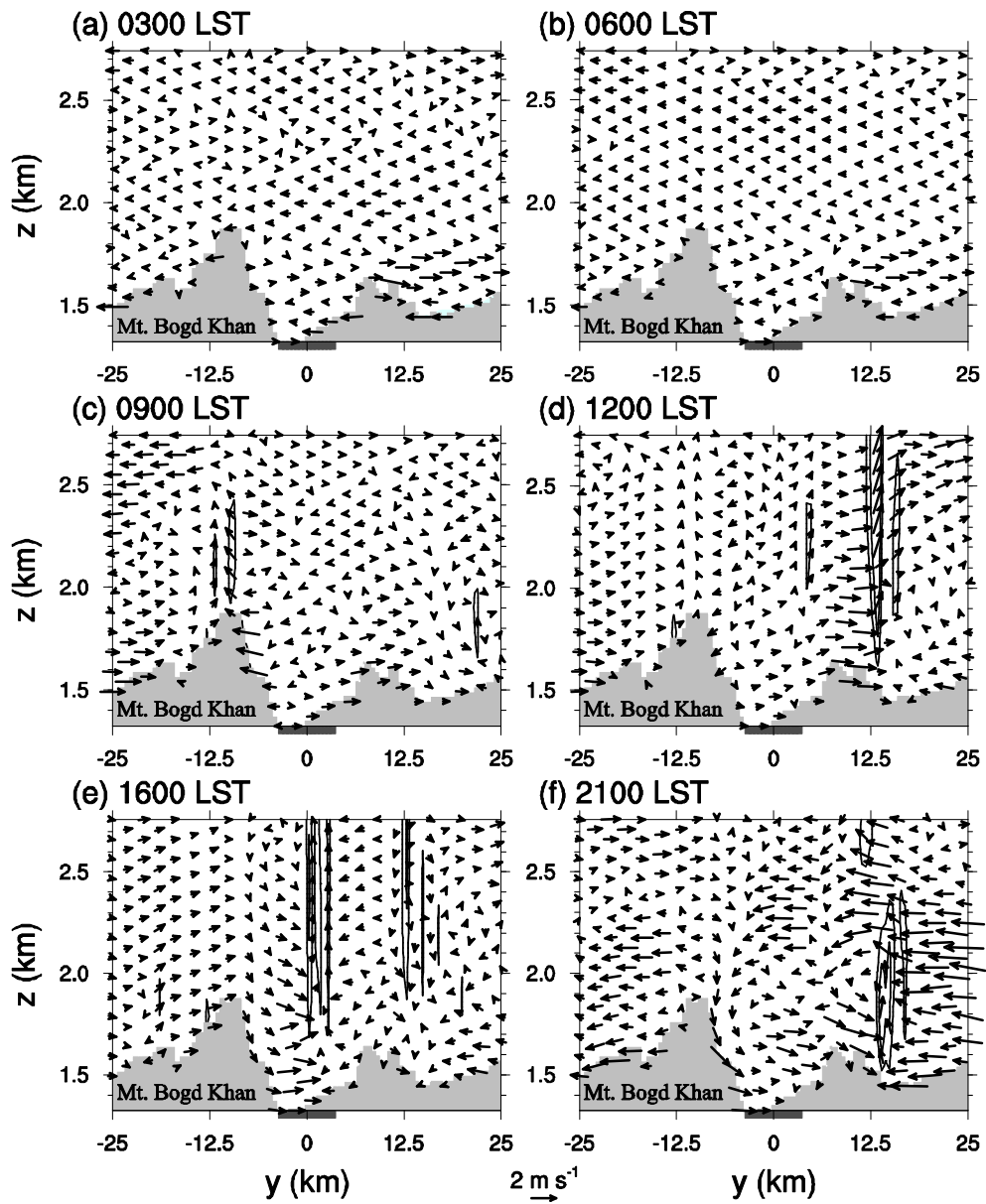


Figure 5.4. Vertical cross-sections of wind vector and vertical velocity (contours) along the south-north direction through the center of the analysis domain at (a) 0300, (b) 0600, (c) 0900, (d) 1200, (e) 1600, and (f) 2100 LST

in the control simulation. The contour levels of vertical velocity are 0.5 and 1 m s⁻¹. The dark gray bar on the horizontal axis indicates the urban area.

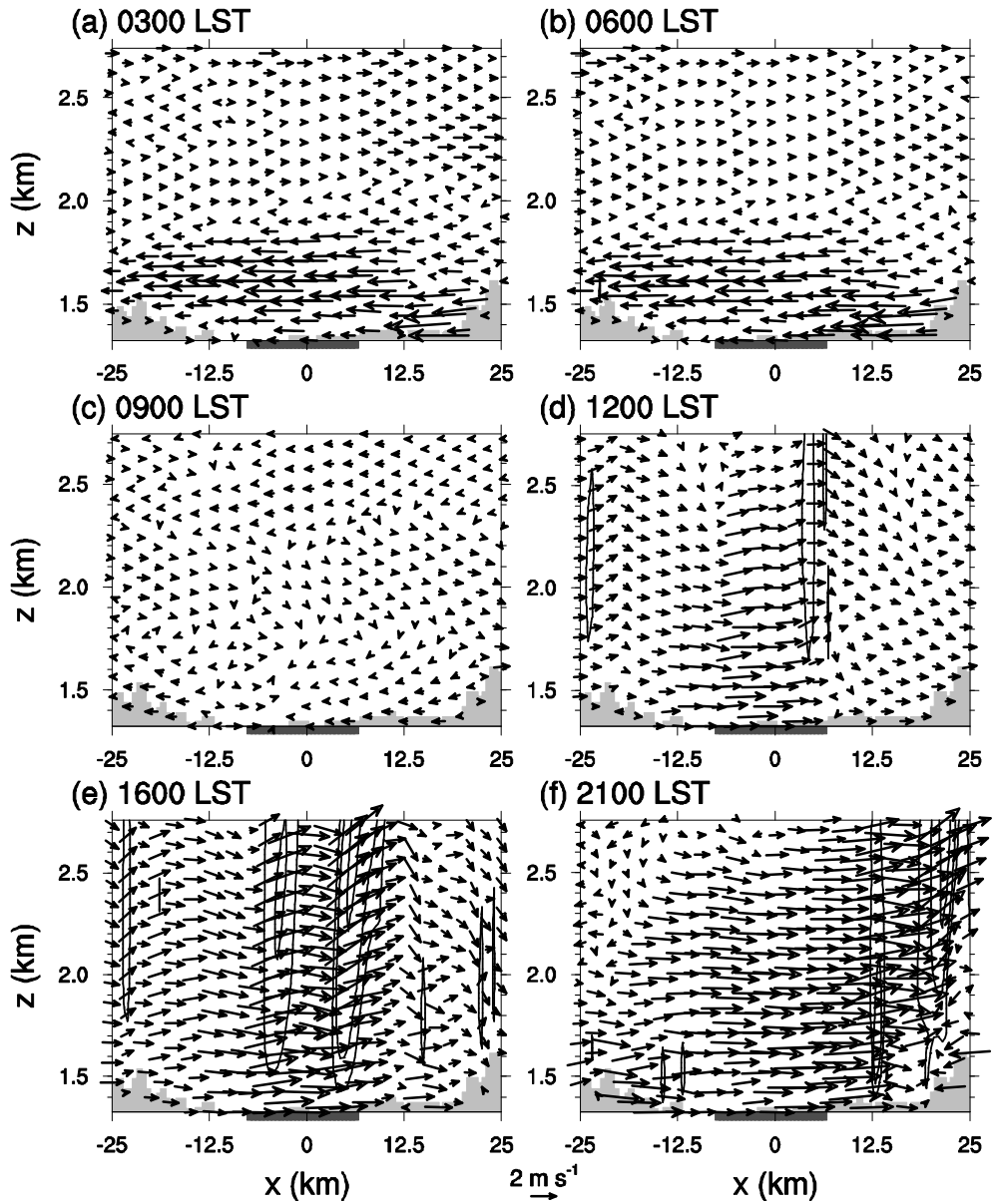


Figure 5.5. Same as in Fig. 5.4 but for the east-west direction. The contour levels of vertical velocity are 0.5 , 1 , and 2 m s^{-1} .

simulated winds result from these interactions.

At 0300 LST, the air temperature in Ulaanbaatar is much higher than that in its surrounding areas, exhibiting a well-developed urban heat island, and down-valley winds in the city (easterly) and weak mountain downslope winds appear (Fig. 5.3a). Down-valley winds are strong in some valley regions (e.g. valleys located to the northeast and southeast of Ulaanbaatar). Winds blowing from the tributary valleys join in/near the city valley. It is interesting to observe that down-valley winds in the city strengthen on the eastern side of the city. This is partially due to nighttime urban breezes. Down-valley winds over the city are prominent up to a height of ~600 m above the surface, featuring channeling flows (Fig. 5.5a). These results are largely consistent with those of Giovannini et al. (2014) which indicate that in the nighttime strong down-valley winds or channeling flows appear over a valley city, Trento, and the city strengthens down-valley winds.

After sunrise, the near-surface air temperature gradually increases as the surface is heated by solar radiation. At 0600 LST, the air temperature difference between Ulaanbaatar and the surrounding areas is small and air temperatures are higher on mountain slopes than in valleys (Fig. 5.3b). Down-valley winds are still strong (Fig. 5.3b). In some regions, mountain upslope winds begin to develop (Figs. 5.3b, 5.4b). At 0900 LST, the urban heat island nearly disappears (Fig. 5.3c). Mountain upslope winds are well

developed at this time (Fig. 5.3c), and updrafts are produced over the peak of Mt. Bogd Khan (Fig. 5.4c). Strong down-valley winds present at 0300 and 0600 LST disappear at 0900 LST (Figs. 5.3a–c). Along-valley winds at 0900 LST are very weak (Fig. 5.5c). At 1200 LST, mountain upslope winds are well developed and up-valley winds appear (Fig. 5.3d). Up-valley winds over the city are found up to a height of ~1400 m above the surface (Fig. 5.5d). Moreover, up-valley winds near the valley mouth region of the valley city weaken due to urban breeze circulation (Figs. 5.3d, 5.5d). Based on Fig. 3b–d, mountain upslope winds precede up-valley winds. At 1600 LST, mountain upslope winds and up-valley winds are well defined (Fig. 5.3e). Over the city, there are two regions with strong and relatively wide updrafts centered at $x = 3.5$ and 6 km (Fig. 5.5e). At 2100 LST, the urban heat island is established and local circulations are featured by up-valley winds in the city and mountain downslope winds (Fig. 5.3f).

In the morning, upslope winds are developed on the urban-side (northern) slope of Mt. Bogd Khan (Fig. 5.4c). As the urban breeze circulation becomes strong, the upslope winds weaken and eventually become downslope winds due to opposing urban breezes. Downslope winds on the urban-side slope of Mt. Bogd Khan are distinct in the late afternoon when the urban breeze circulation is strong (Fig. 5.4e). These features result

from the interactions of urban breeze circulation with mountain slope winds. This finding agrees with the results of previous study (e.g., section 3.2.2). Figure 5.6 shows the diurnal variation of wind vector at 10 m and the time-height variation of horizontal wind vector and boundary layer height at an urban location ($x = 0$ km, $y = 0$ km). The diurnal pattern of the wind speed and direction is shown up well. The channeling wind is clearly seen in the nighttime with maximum intensity of 5.6 m s^{-1} in the lowest ~ 600 m above the nighttime shallow boundary layer (< 100 m). This channeling wind is not apparent at the valley exit, where the topography is widened there (not shown). After ~ 0800 LST, as the down-valley wind ceases and the up-valley wind starts, the channeling wind is about to weaken and eventually vanishes. In the daytime, the two-layer structure of the wind direction within and urban breeze circulation and the up-valley winds. The daytime southwesterly winds are up-valley winds.

5.2.2 Sensitivity experiments

The sensitivity experiment results are presented and discussed in this section. The sensitivity of local circulations to urban fraction is examined by comparing simulations with different urban fractions: 0.5 (simulation called UF05), 0.7 (UF07, control simulation), and 0.9 (UF09). The sensitivity of local circulations to atmospheric stability is examined by comparing

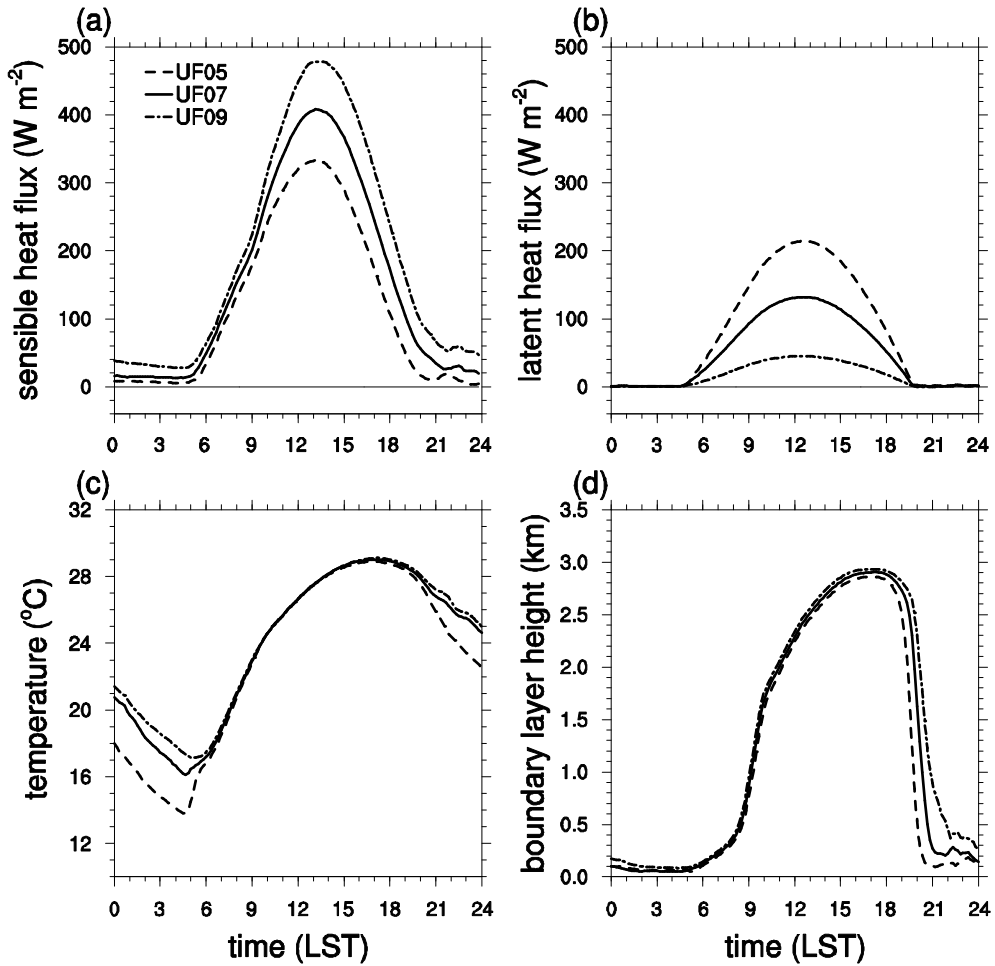


Figure 5.6. Diurnal variations of (a) surface sensible heat flux, (b) surface latent heat flux, (c) air temperature at 2 m, and (d) atmospheric boundary-layer height averaged over the urban area in the UF05 (dashed), UF07 (solid), and UF09 (dot-dashed) simulations.

simulations with different atmospheric stabilities: the initial potential slightly above the boundary layer (westerly in the lower layer and easterly in the upper layer) is apparently due to the return flow associated with both the temperature lapse rate is set to 4 (AS4), 5 (AS5, control simulation), and 6 (AS6) K km⁻¹. The sensitivity of local circulations to volumetric soil water content is examined by comparing simulations with different initial soil water contents: 0.09 (SW009), 0.17 (SW017, control simulation), and 0.25 (SW025) m³ m⁻³.

The diurnal variations of surface sensible heat flux, surface latent heat flux, 2-m air temperature, and atmospheric boundary-layer height averaged over the urban area in the UF05, UF07, and UF09 simulations are shown in Fig. 5.7. As expected, the UF09 simulation produces the largest daytime sensible heat flux and the smallest daytime latent heat flux. The urban area- averaged maximum sensible heat fluxes are 332, 408, and 478 W m⁻² in the UF05, UF07, and UF09 simulations, respectively. The urban area-averaged maximum latent heat fluxes are 214, 132, and 45 W m⁻² in the UF05, UF07, and UF09 simulations, respectively. In the nighttime, differences in 2-m air temperature between the UF09 and UF07 simulations are small compared to those between the UF07 and UF05 simulations. The daytime 2-m air temperatures are very similar in the three simulations.

Differences in atmospheric boundary-layer height between the simulations
at any time are

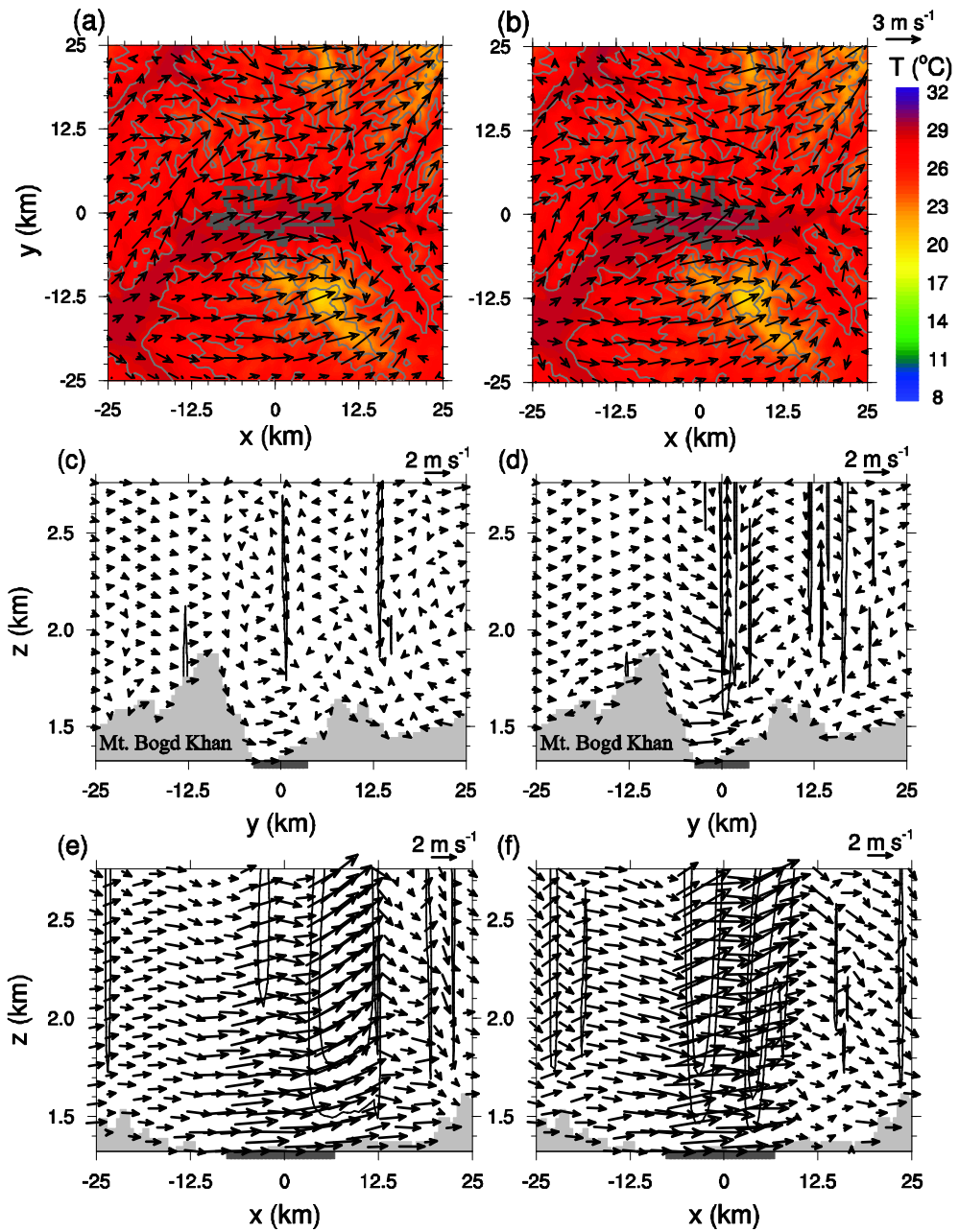


Figure 5.7. Fields of air temperature at 2 m and wind vector at 10 m in the (a) UF05 and (b) UF09 simulations and the vertical cross-sections of wind vector and vertical velocity (contours) along the south-north direction

through the center of the analysis domain in the (e) UF05 and (f) UF09 simulations at 1600 LST. The dark gray line in (a) and (b) indicates the urban boundary. Light gray contours in (a) and (b) indicate the terrain height (from 1300 to 2100 m with intervals of 200 m). The dark gray bar on the horizontal axis in (c)–(f) indicates the urban area. The contour levels of vertical velocity in (c)–(f) are 0.5 and 1 m s⁻¹.

small except in the late afternoon/evening. The daytime maximum atmospheric boundary-layer height slightly increases as urban fraction increases.

Figure 5.8 shows 2-m air temperature and 10-m wind vector fields and the vertical cross-sections of wind vector and vertical velocity along the south-north and east-west directions through the center of the analysis domain at 1600 LST in the UF05 and UF09 simulations. The air temperature fields are similar to each other (Figs. 5.3e, 5.8a,b). The overall local circulation patterns are also similar to each other, but there are some differences in local circulation intensity. Downslope winds on the urban-side slope of Mt. Bogd Khan strengthen as urban fraction increases (Figs. 5.4e, 5.8c,d). This result is apparently due to strengthened urban breezes with increasing urban fraction. As urban fraction increases, up-valley winds over the city strengthen and up-valley winds near the valley mouth region of the valley city weaken (Figs. 5.5e, 5.8e,f). These features are also apparently due to strengthened urban breezes with increasing urban fraction.

Ulaanbaatar is the capital of Mongolia and is the highest populated administrative region in Mongolia. Ulaanbaatar has been rapidly urbanized in recent decades. The population of Ulaanbaatar increased from 0.8 million in 1999 to 1.3 million in 2013. The results of the sensitivity experiments of urban fraction imply that if urbanization continues, local winds in and

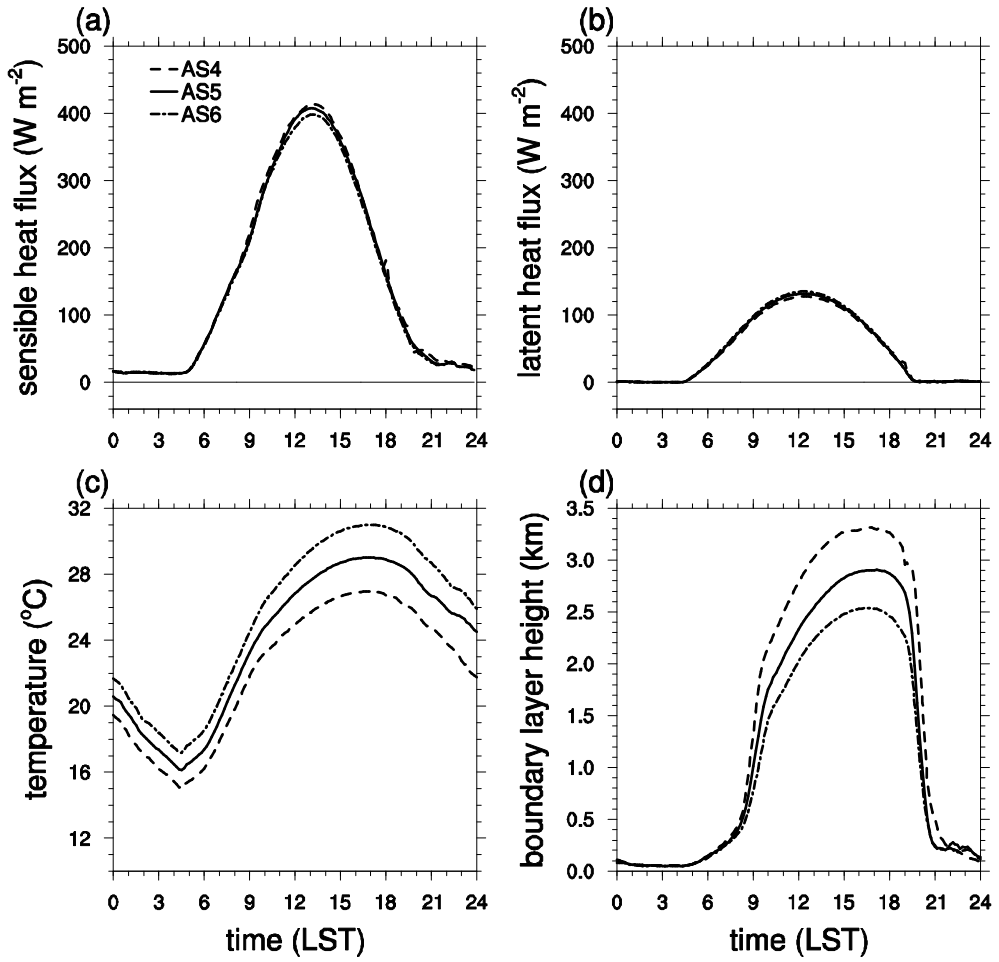


Figure 5.8. Same as in Fig. 5.6 but for the AS4 (dashed), AS5 (solid), and AS6 (dot-dashed) simulations.

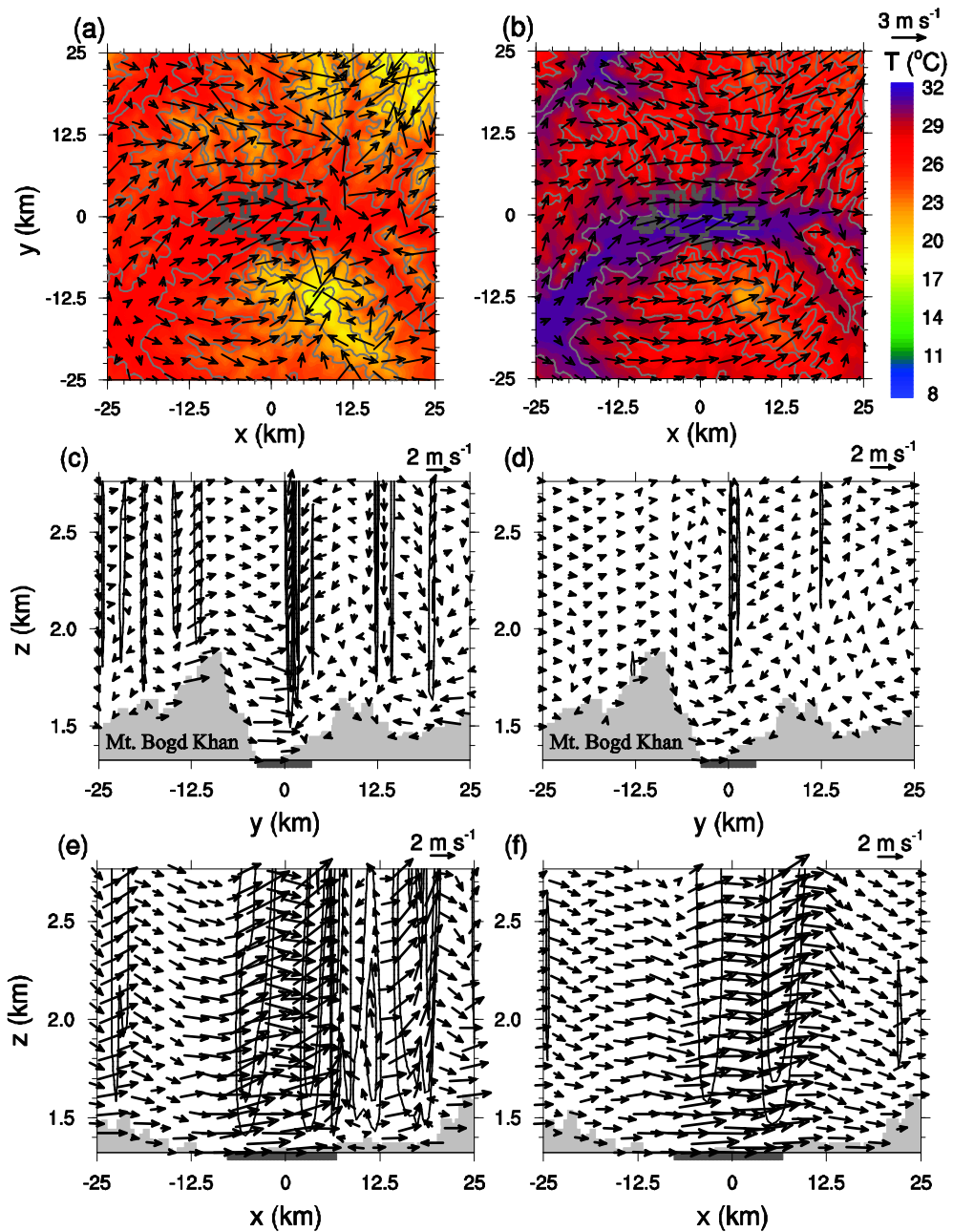


Figure 5.9. Figure 5.9. Same as in Fig. 5.7 but for the AS4 and AS6 simulations. The contour levels of vertical velocity in (c)–(f) are 0.5, 1, and 2 m s^{-1} .

near Ulaanbaatar will be altered. The alteration may include enhanced daytime up-valley winds over the city and enhanced daytime downslope winds on the urban-side slope of Mt. Bogd Khan.

The diurnal variations of surface sensible heat flux, surface latent heat flux, 2-m air temperature, and atmospheric boundary-layer height averaged over the urban area in the AS4, AS5, and AS6 simulations are shown in Fig. 5.9. Changes in atmospheric stability have insignificant impacts on surface sensible and latent heat fluxes but have significant impacts on air temperature and atmospheric boundary-layer height. As atmospheric stability increases, daytime and nighttime air temperatures increase and the daytime atmospheric boundary-layer height decreases. The urban area-averaged maximum atmospheric boundary-layer heights in the AS4, AS5, and AS6 simulations are 3313, 2906, and 2538 m, respectively.

In this study, atmospheric stability means the stability of the atmosphere expressed in terms of the initial potential temperature lapse rate. Thus, atmospheric stability in this study can be roughly regarded as the basic-state atmospheric stability. Local circulations simulated in this study are largely confined to the lower atmosphere, i.e., within a few kilometers above the surface. In the simulations, the stability above the lower atmosphere changes very little with time, thus being similar to the basic-state atmospheric stability. However, the stability of the lower atmosphere

varies with time, exhibiting convective boundary layers in the daytime in which the potential temperature is nearly constant with height and stable nighttime boundary layers. For larger atmospheric stability, more stable atmosphere above the lower atmosphere acts to suppress the growth of daytime convective boundary layer. This is a reason for less deep atmospheric boundary layer when atmospheric stability is larger (Fig. 5.9d).

Figure 5.10 shows 2-m air temperature and 10-m wind vector fields and the vertical cross-sections of wind vector and vertical velocity along the south-north and east-west directions through the center of the analysis domain at 1600 LST in the AS4 and AS6 simulations. The air temperature field in the AS4 simulation exhibits cold regions at the higher altitudes of the mountains located to the northeast and southeast of Ulaanbaatar. In these regions, downslope winds are produced. In the AS6 simulation, air temperatures are high in the valleys. As atmospheric stability increases, up-valley winds become more consistently directed in the along-valley direction (Figs. 5.5e, 5.10e,f) and cross-valley winds tend to weaken (Figs. 5.4e, 5.10c,d). Near- surface up-valley winds strengthen with increasing atmospheric stability (Figs. 5.5e, 5.10e,f). This seems to be related to higher near-surface air temperature in the urban area for larger atmospheric stability.

The diurnal variations of surface sensible heat flux, surface latent heat flux, 2-m air temperature, and atmospheric boundary-layer height averaged

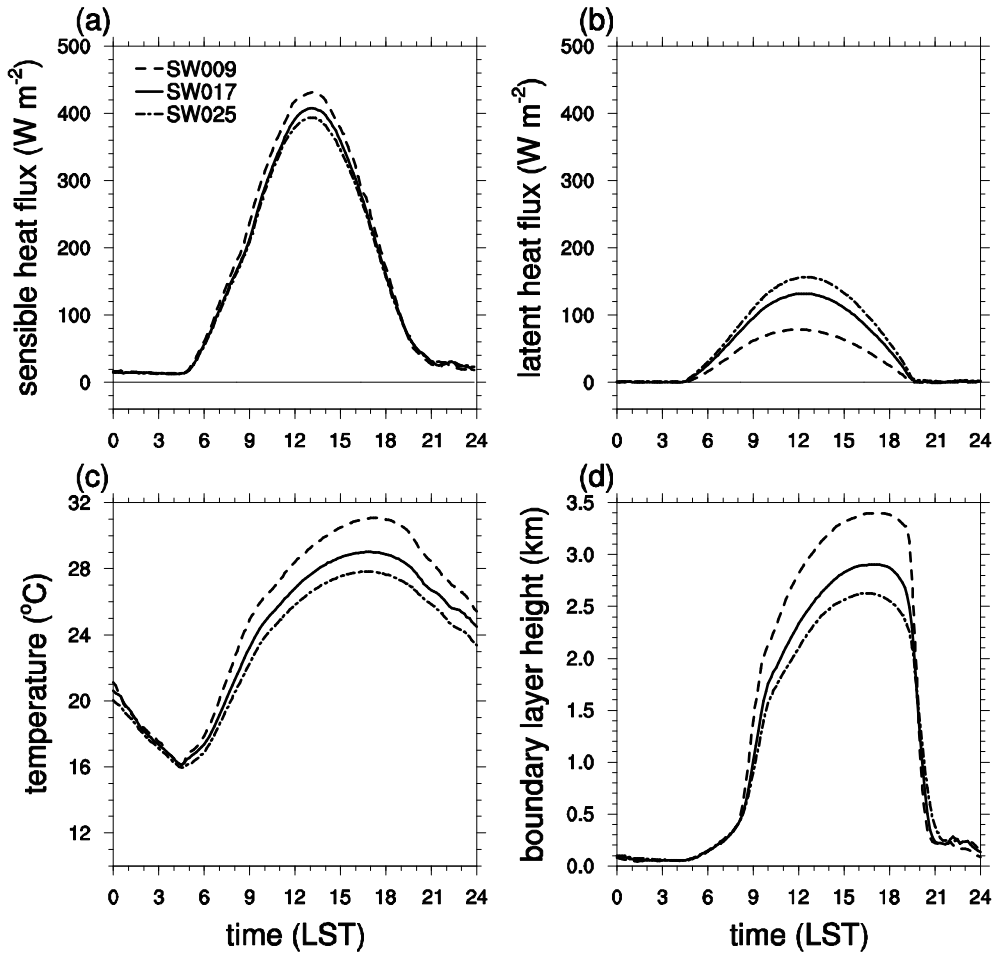


Figure 5.10. Same as in Fig. 5.6 but for the SW009 and SW025 simulations.

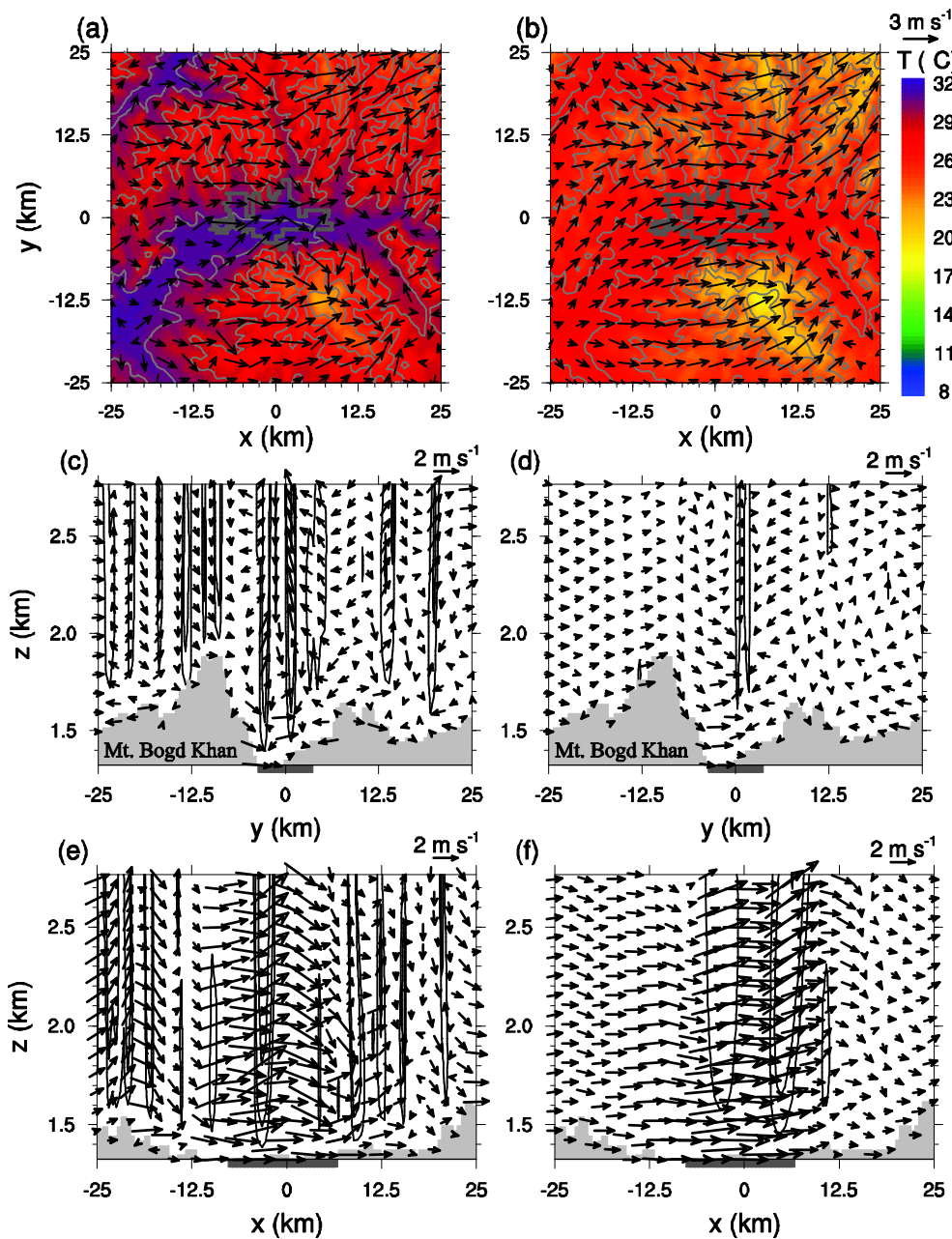


Figure 5.11. Same as in Fig. 5.7 but for the SW009 and SW025 simulations.

The contour levels of vertical velocity in (c)–(f) are 0.5 , 1 , and 2 m s^{-1} .

over the urban area in the SW009, SW017, and SW025 simulations are shown in Fig. 5.11. As soil water content decreases, in the daytime the surface sensible heat flux increases, the surface latent heat flux decreases, and the air temperature increases. The diurnal air temperature range is the largest in the SW009 simulation. The daytime atmospheric boundary-layer height is sensitive to soil water content. The urban area-averaged maximum atmospheric boundary-layer heights in the SW009, SW017, and SW025 simulations are 3397, 2906, and 2627 m, respectively.

Figure 5.12 shows 2-m air temperature and 10-m wind vector fields and the vertical cross-sections of wind vector and vertical velocity along the south-north and east-west directions through the center of the analysis domain at 1600 LST in the SW009 and SW025 simulations. As soil water content decreases, the air temperature increases (Figs. 5.3e, 5.12a,b). Based on the results of the atmospheric stability and soil water content sensitivity experiments, the impact of drier soil on near-surface air temperature is similar to that of larger atmospheric stability on near-surface air temperature. For example, air temperatures are high in the valleys in both AS6 simulation (larger atmospheric stability) and SW009 simulation (drier soil) (Figs. 5.9b, 5.12a). In the SW009 simulation, numerous small-scale deep convective updraft cells appear (Fig. 5.12c). As soil water content decreases, downslope winds on the urban-side upper slope of Mt. Bogd Khan weaken

while downslope winds on the urban-side lower slope of Mt. Bogd Khan strengthen (Figs. 5.4e, 5.12c,d). As soil becomes dry, that is, soil water content decreases, the daytime surface sensible heat flux increases. Note that the urban area consists of 30% natural area. At 1600 LST, in the SW009 simulation the surface sensible heat flux averaged over the urban area is 321 W m^{-2} (19 W m^{-2} increase compared to the control simulation) and the surface sensible heat flux averaged over the rural areas is 155 W m^{-2} (49 W m^{-2} increase compared to the control simulation). Hence, the gradient in surface sensible heat flux between the urban and rural areas decreases, which leads to weaker urban breeze circulation and thereby weakened near-surface up-valley winds in the city.

6 Local circulations in the Ulaanbaatar area: A case study

In the previous section, the local circulations in and around the Ulaanbaatar metropolitan area were investigated in idealized environments. Based on idealized settings, sensitivities of urban fraction, atmospheric stability, and soil water content to the local circulations were examined. The study is motivated to understand the local circulations and urban impacts on local circulations as combined results of temperature inversion in wintertime, limited ventilation in the valley due to topography, and urban pollutants cause serious air pollution problem in Ulaanbaatar. This section investigates the local circulations under wintertime conditions with temperature inversion in and around the Ulaanbaatar metropolitan area through the real-data simulations.

6.1 Experimental design

In this section, the same model and physics options that used in section 5 are used. The numbers of horizontal grid points for the five computational domains are 110×125 , 247×148 , 181×103 , 142×142 , and 181×181 with horizontal grid intervals of 27, 9, 3, 1, and $1/3$ km, respectively (Fig. 6.1a). The cumulus parameterization scheme is applied to

the outer two computational domains with horizontal grid intervals of 27 and 9 km. The initial and boundary conditions are taken from National Centers for Environmental Prediction final analysis data with horizontal resolution of $1^\circ \times 1^\circ$ in 6-h intervals. The model is integrated for 28 h, starting from 1200 UTC (2000 LST) 18 December 2013 and the last 24 h data are used for the analysis. Terrain data from the Shuttle Radar Topography Mission (SRTM) data with a resolution of ~ 90 m (Jarvis et al. 2008) provide a good representation of topography for the study area (Fig. 6.1b). The land-use/land-cover data consist of the United States Geological Survey (USGS) dataset and a combined dataset for Ulaanbaatar that includes the Moderate Resolution Imaging Spectroradiometer (MODIS) data (Friedl et al. 2002), the GlobCover land cover classifications map (Arino et al. 2010), and the Google Earth imagery (Google Inc. 2013).

6.2 Synoptic weather and model validation

Palffy (1995) and Whiteman et al. (1999) stated that the high-pressure system in wintertime is a favorable condition for the development of temperature inversion. A Siberian high-pressure system dominated in the study area on 18–20 December 2013 (see the surface weather map in Fig. 6.2a). The upper level was under the influence of the large-scale ridge system (see the 850-hPa weather map in Fig. 6.2b). Wind speeds at 10 m

observed at meteorological stations in and around Ulaanbaatar were 0–3 m s⁻¹ on 19 December 2013. Wind speeds at 700 and 850 hPa were 1–4 m s⁻¹. Skies were clear. Thus, the synoptic conditions were favorable for the formation of temperature inversion in the complex terrain.

The simulated 2-m temperature and 10-m wind speed and direction in the computational domain with a 9-km horizontal grid interval are validated against observations at 26 meteorological stations (Figs. 6.3a–c). The observations in Figs. 6.3a–c are averaged over the 26 meteorological stations (Fig. 6.1a), and the simulation data in Figs. 6.3a–c are averaged over 26 corresponding grid points (nearest to the meteorological stations). The meteorological stations are indicated by black dots in Fig. 6.1a. In the simulation, the minimum temperature is overestimated and the maximum temperature is slightly underestimated, but the diurnal variation of temperature is well reproduced. The wind speed is slightly overestimated. The scatterplot of observed and simulated 2-m temperatures shows a good agreement between the observations and simulation (Fig. 6.3d). To quantify the performance of the model, the hit rate is calculated. The accuracy ranges of hit rates for temperature, wind speed, and wind direction are set as $\pm 2^{\circ}\text{C}$, 1 m s^{-1} , and 30° , respectively. The calculated hit rates for temperature, wind speed, and wind direction are 94.9%, 96.1%, and 83.1%, respectively, demonstrating a good performance. The simulated atmospheric vertical

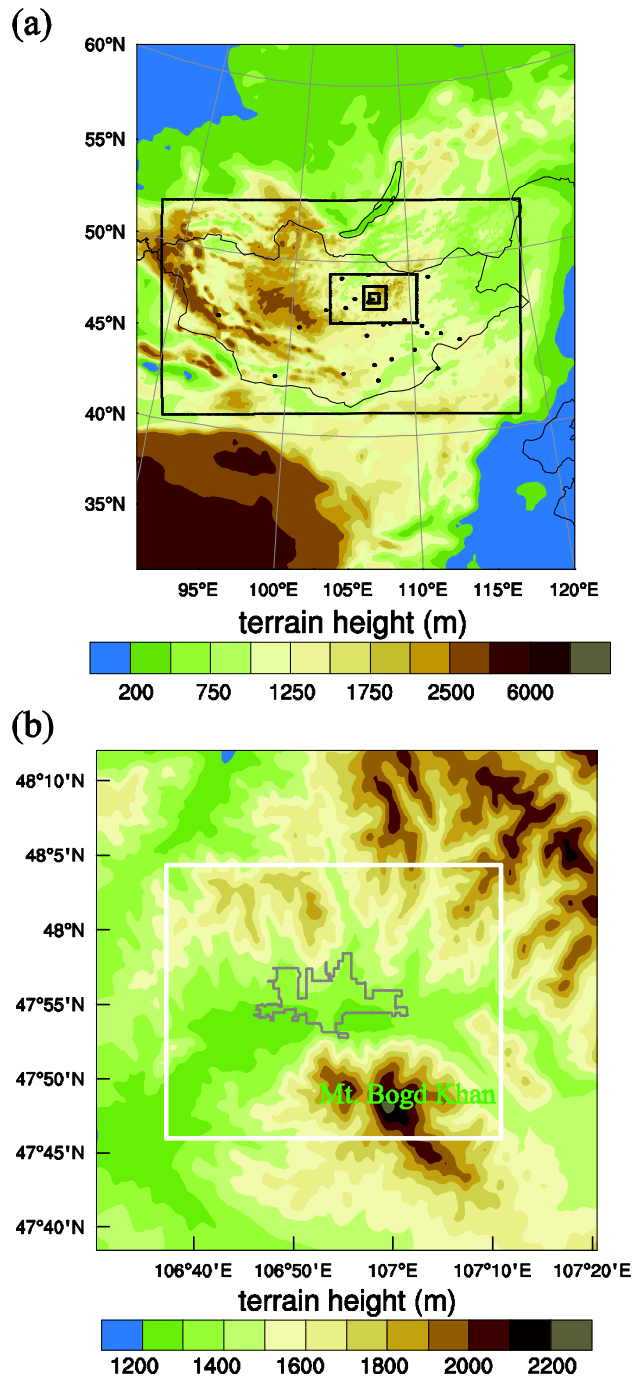
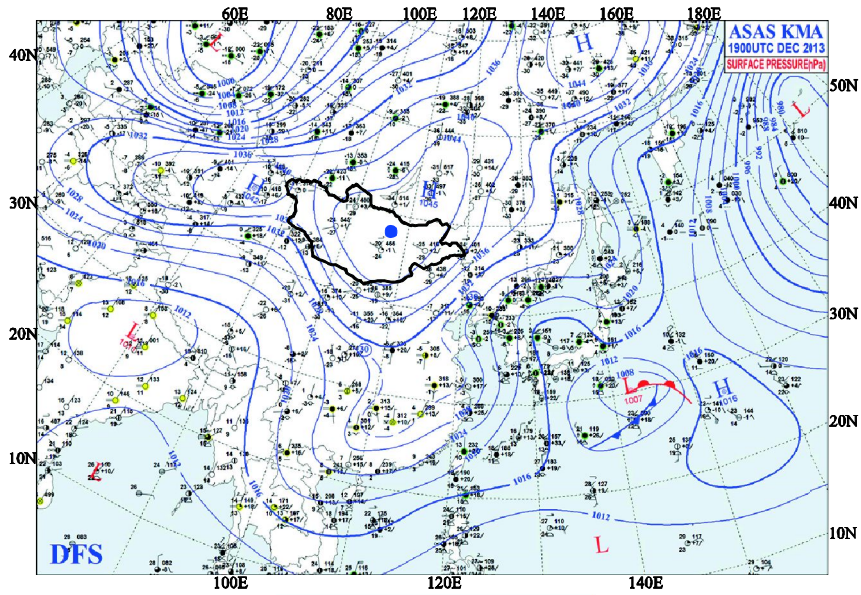


Figure 6.1. Terrain height in the (a) five computational domains and (b) innermost domain. The white rectangle in (b) indicates the analysis area. 26

meteorological stations are indicated by the black dots in (a). The urban boundary is indicated by the gray line in (b).

(a)



(b)

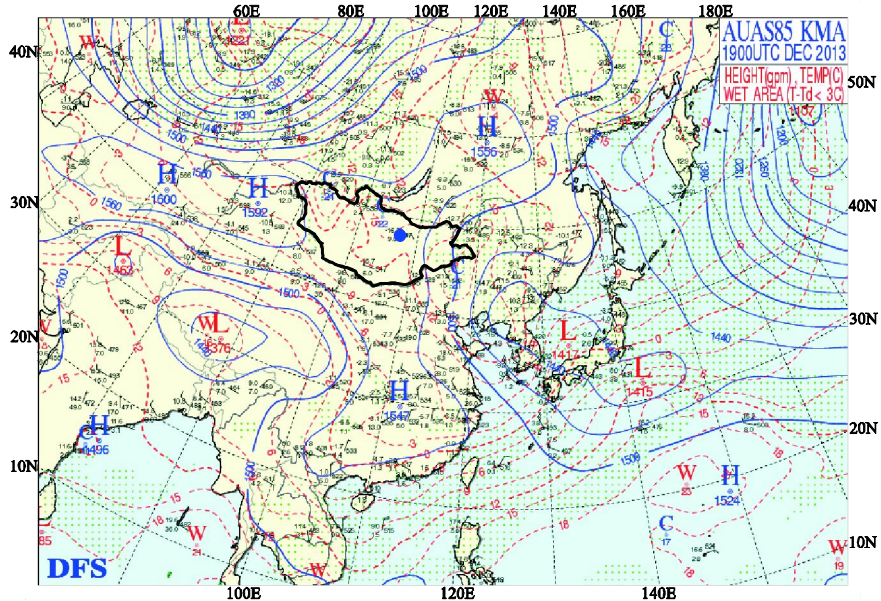


Figure 6.2. (a) Surface and (b) 850 hPa weather maps at 0000 UTC (0800 LST) 19 December 2013. Ulaanbaatar is indicated by the blue circle. (after courtesy of the Korea Meteorological Administration.)

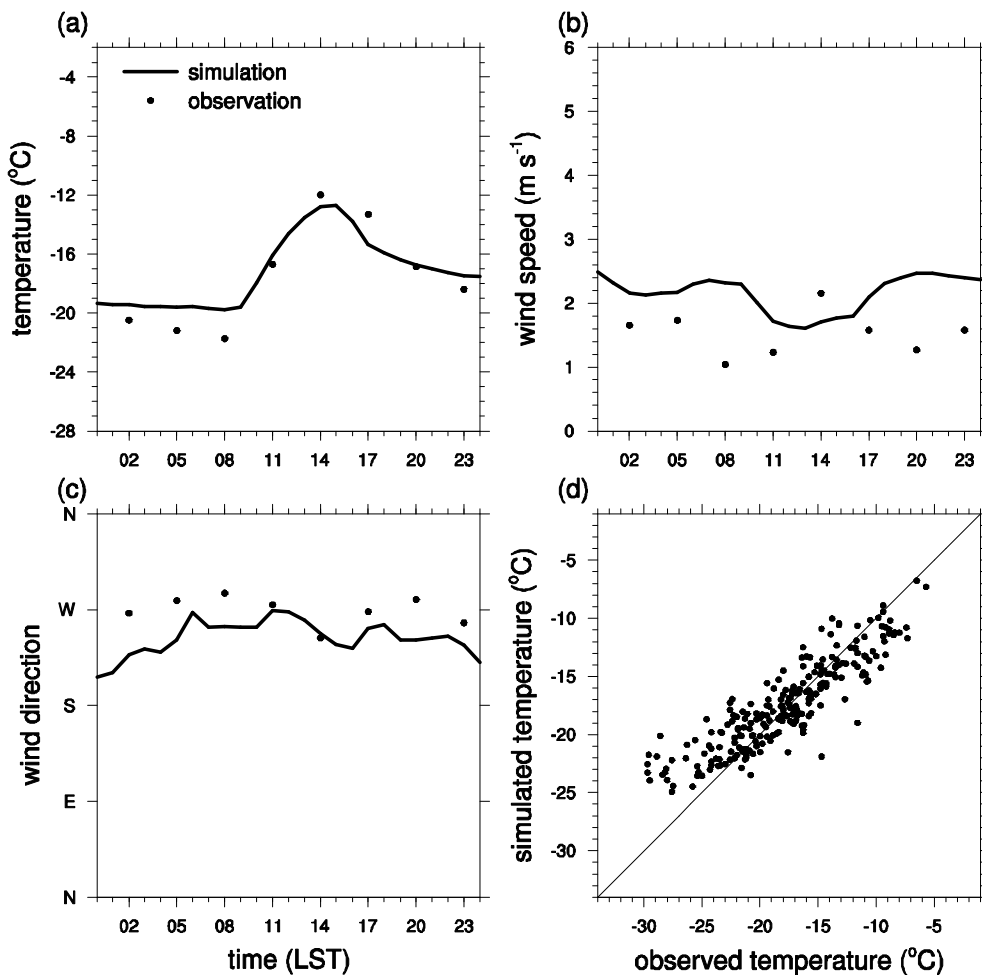
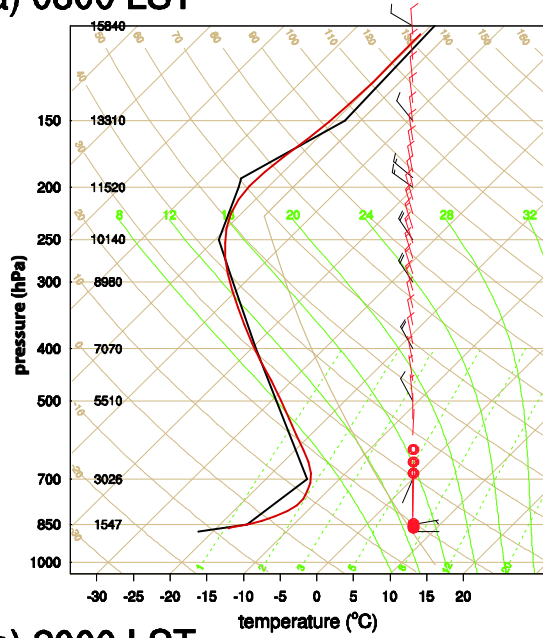


Figure 6.3. Diurnal variations of observed and simulated (a) 2-m temperature, (b) 10-m wind speed, (c) 10-m wind direction, and (d) scatterplot of 2-m temperatures observed at 26 meteorological stations and simulated. Observations are made at 3-h intervals.

(a) 0800 LST



(b) 2000 LST

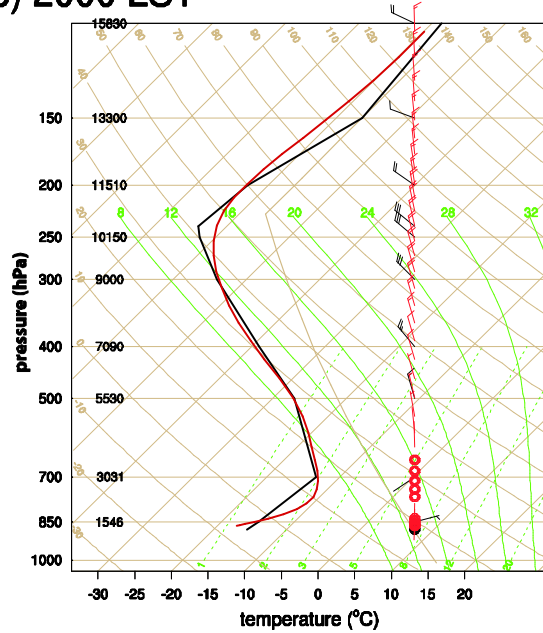


Figure 6.4. Skew T -log p diagrams at Ulaanbaatar station for observations (black) and simulations (red) valid at (a) 0800 and (b) 2000 LST 19 December 2013.

structure shows generally good agreement with observed one (Fig. 6.4).

6.3 Results and discussions

Figure 6.5 shows the diurnal variations of surface sensible heat flux, surface latent heat flux, 2-m temperature, and boundary layer height averaged over the urban area (see the area bounded by the gray line in Fig. 6.1b). Note that the simulated 2-m temperature averaged over the urban area is very low, ranging from -21°C to -15°C , and that local circulations in a very cold environment area investigated in this study. The simulated wintertime surface sensible heat flux is smaller than the summertime one (section 5.1.1). The maximum surface sensible heat flux is 104 W m^{-2} at 1330 LST. The surface latent heat flux is much smaller than the surface sensible heat flux, which is a typical feature of urban areas (Grimmond et al. 2010). The maximum surface latent heat flux is 12 W m^{-2} at 1320 LST. In contrast with the summertime deep convective boundary layer (section 5.1.1), the growth of the boundary layer in wintertime is suppressed. The boundary layer grows only up to a maximum of 172 m in the daytime. The nighttime boundary layer is very shallow in the very stable atmosphere, consistent with previous studies (e.g., Mahrt and Vickers 2006; Banta et al. 2007). In the very stable atmosphere, most of the surface sensible heat flux acts to reduce the large

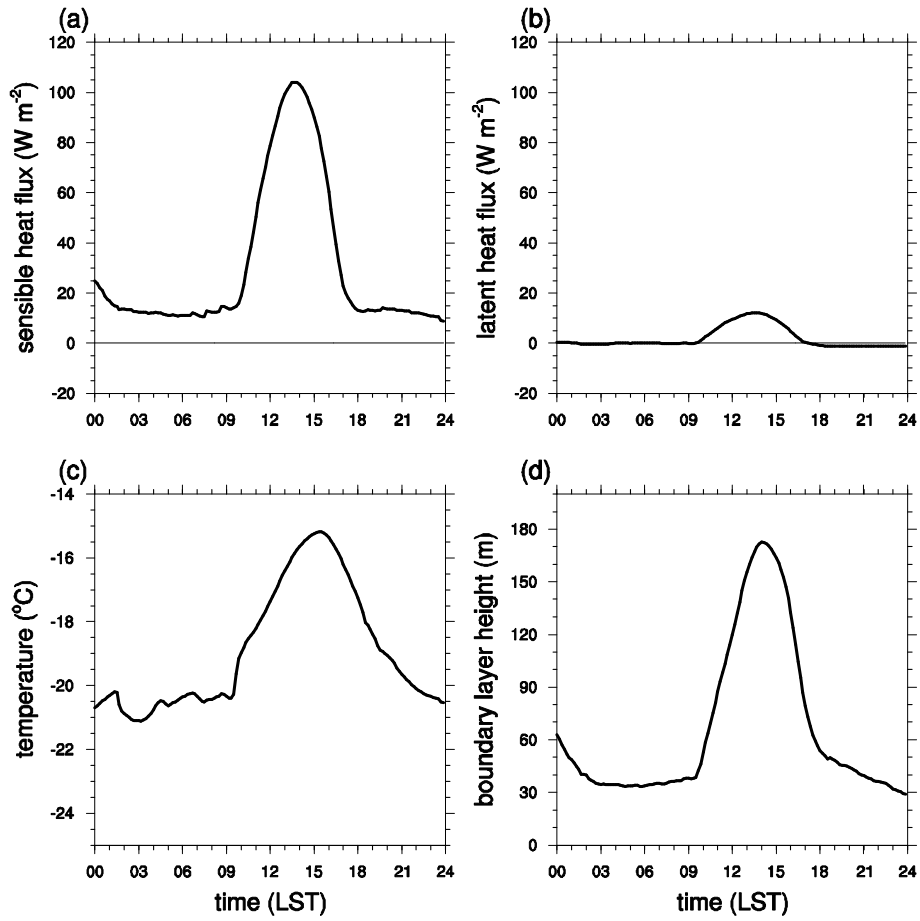


Figure 6.5. Diurnal variations of (a) surface sensible heat flux, (b) surface latent heat flux, (c) 2-m temperature, and (d) boundary layer height averaged over the urban area.

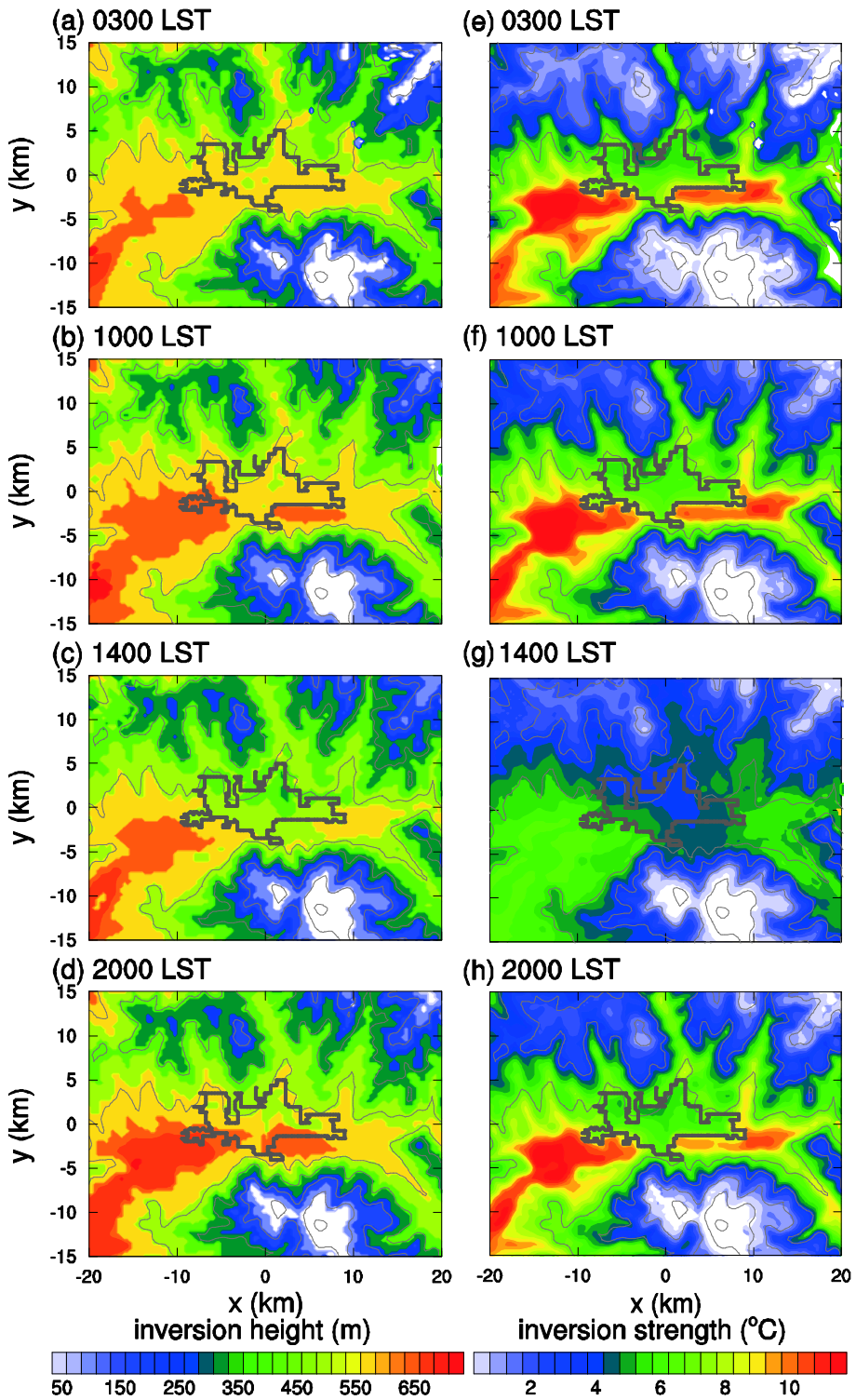


Figure 6.6. Fields of the thickness (left) and strength (right) of temperature inversion layer at (a), (e) 0300, (b), (f) 1000, (c), (g) 1400, and (d), (h) 2000 LST. The light gray lines (also in Figs. 6.8, 6.11, 6.12) indicate terrain height contours (from 1400 to 2200 m with intervals of 200 m). The urban boundary is indicated by the dark gray line (also in Figs. 6.8, 6.11, 6.12). The area without no inversion layer is shaded in white color (also in Fig. 6.11).

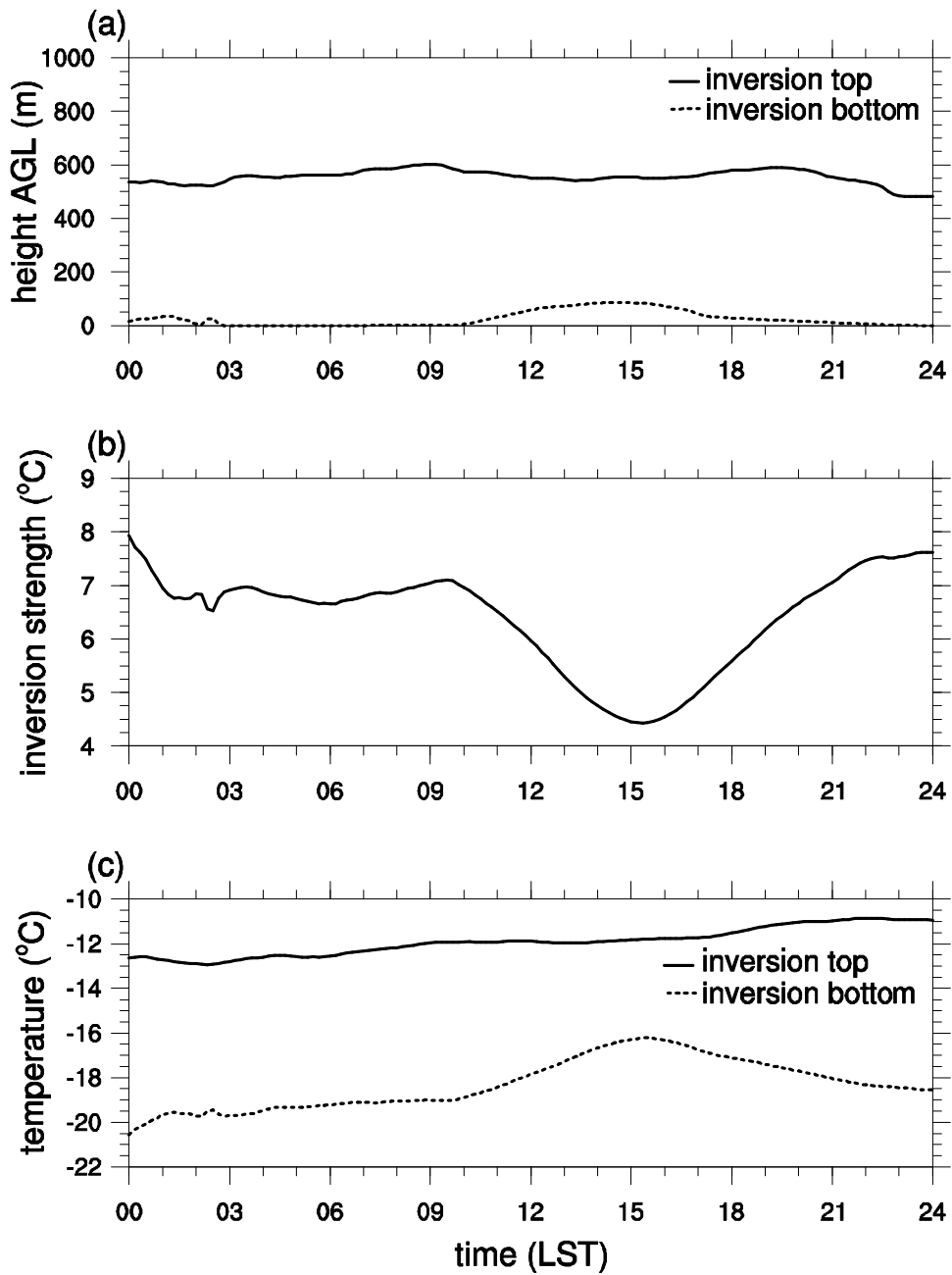


Figure 6.7. Diurnal variations of (a) top and bottom heights of temperature inversion layer, (b) its strength, and (c) temperatures at the inversion top and bottom averaged over the urban area.

temperature lapse rate rather than acts to grow the boundary layer (Bader and McKee 1985).

Figure 6.6 shows the fields of the thickness and strength of temperature inversion layer at 0300, 1000, 1400, and 2000 LST. In this study, the thickness and strength of a temperature inversion layer are determined as differences in height and temperature between its top and bottom, respectively. Figure 6.6 indicates that the temperature inversion is persistent over times and that the thickness and strength of temperature inversion layer are associated with the terrain. The temperature inversion layer is deep and strong in the valleys, particularly in the wide valley located southwest of the domain. On the other hand, the temperature inversion layer is relatively shallow and weak over the mountain slopes and does not exist over and around the high mountain peaks. The temperature inversion layer is shallower and its strength is weaker in the urban area than in its nearby valley area. This is due to urban effects. It is analyzed that the temperature inversion in the valleys except for the urban area and over the mountain slopes is mostly surface-based. It is also analyzed that the bottom of temperature inversion layer lies below the top of the boundary layer and that the top of temperature inversion layer is lower than the maximum ridge top of the surrounding mountains. A boundary layer top that is lower than the inversion top implies that mixing does not effectively occur vertically.

Figure 6.7 shows the diurnal variations of top and bottom heights of temperature inversion layer, its strength, and temperatures at the inversion top and bottom averaged over the urban area. The temperature inversion is not surface-based in the daytime, and the top height of temperature inversion layer averaged over the urban area varies little over times (Fig. 6.7a). The bottom height of temperature inversion layer averaged over the urban area varies between 0 and 86 m and its top height varies between 481 and 601 m. The thickness of temperature inversion layer averaged over the urban area ranges 462–599 m. The simulated thicknesses of temperature inversion layer are comparable to the monthly average over the period of 1981–2010 observed at Ulaanbaatar radiosonde station (Gerelchuluun and Ahn 2014). The temperature inversion strength averaged over the urban area decreases from 0930 LST (7.1°C) to 1520 LST (4.4°C) (Fig. 6.7b) and then increases. As the urban surface heats, the bottom of temperature inversion layer heats and rises up, while its top changes little. This causes the strength of temperature inversion layer to weaken (Figs. 6.7b,c). The destruction of temperature inversion layer, which is associated with the growth of the convective boundary layer with time while the inversion top remains almost fixed in time, is identified as Pattern 1 by Whiteman (1982).

Next, local circulations in the presence of temperature inversion are examined by analyzing simulated temperature and wind fields. Figure 6.8

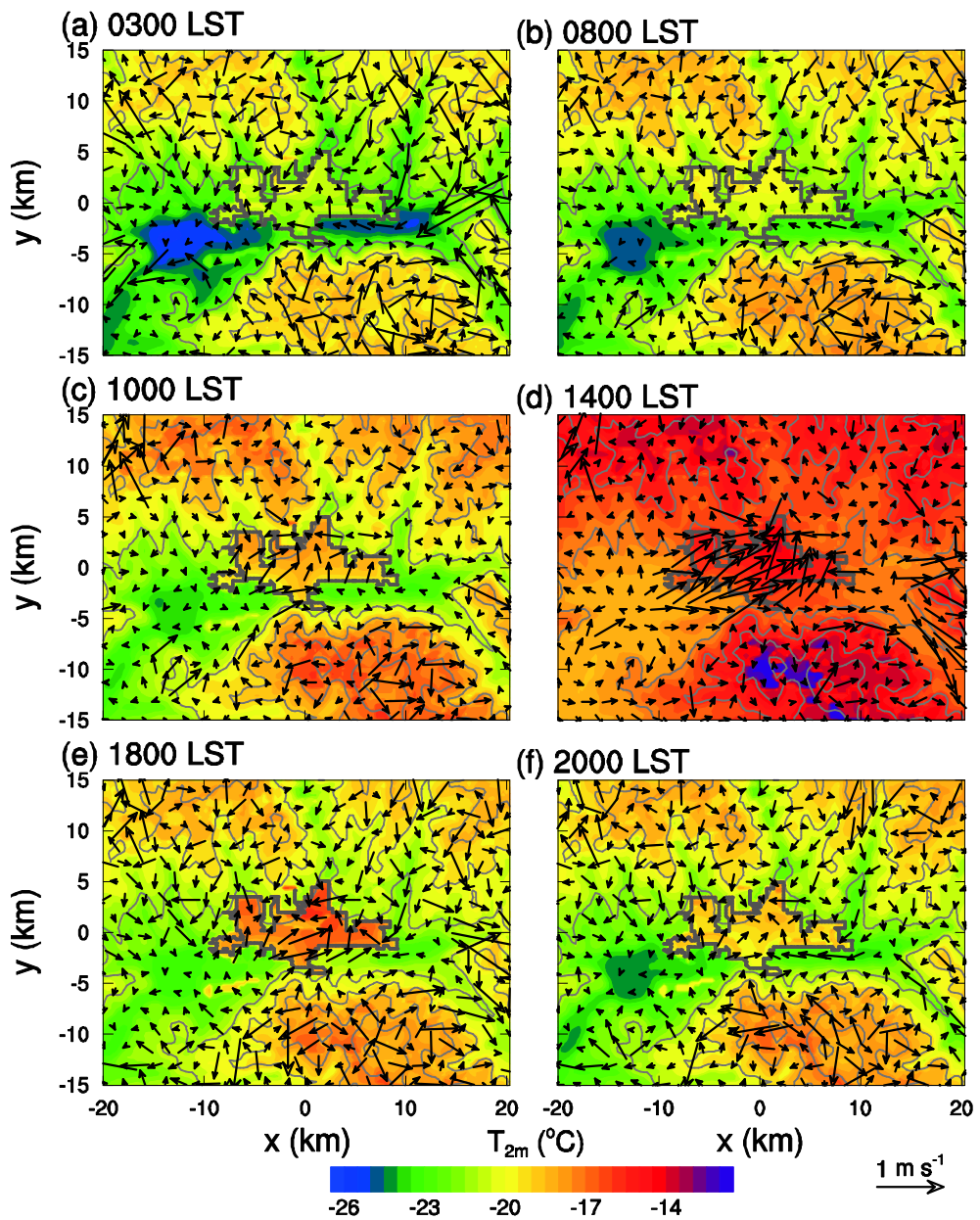


Figure 6.8. Fields of 2-m temperature and 10-m wind vector at (a) 0300, (b) 0800, (c) 1000, (d) 1400, (e) 1800, and (f) 2000 LST.

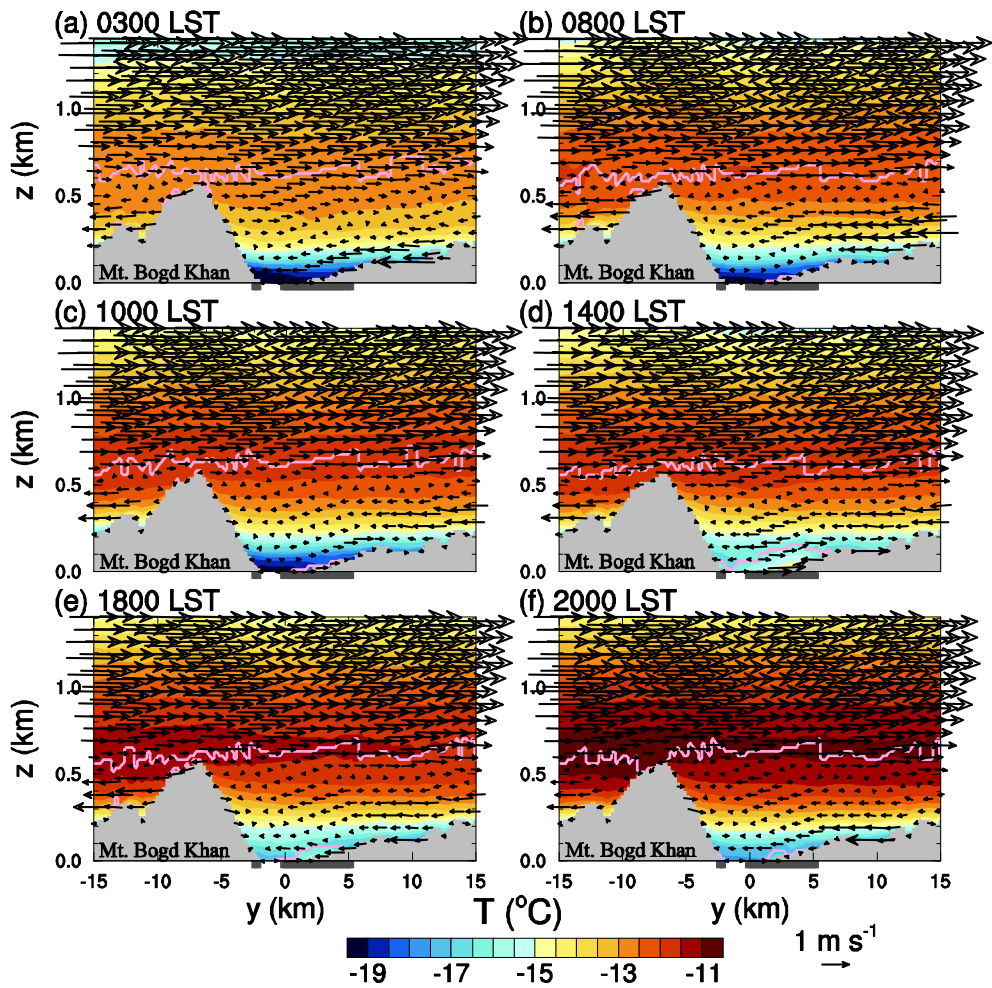


Figure 6.9. Vertical cross-sections of temperature and wind vector along the north-south direction at $x = 0$ km at (a) 0300, (b) 0800, (c) 1000, (d) 1400, (e) 1800, and (f) 2000 LST. The gray boxes on the horizontal axis indicate the urban area, and pink lines indicate the boundary where the vertical temperature gradient changes its sign (also in Fig. 6.10).

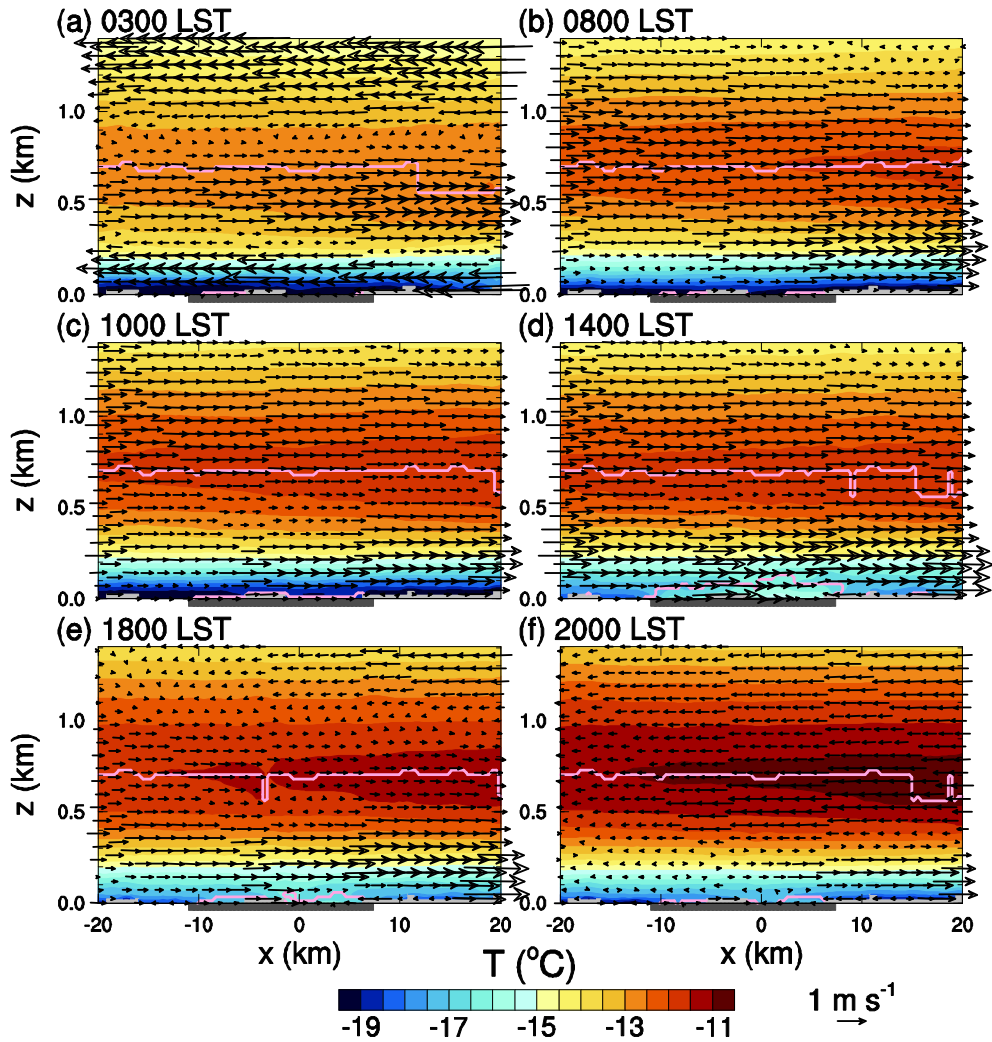


Figure 6.10. Vertical cross-sections of temperature and wind vector along the east-west direction at $y = 0$ km at (a) 0300, (b) 0800, (c) 1000, (d) 1400, (e) 1800, and (f) 2000 LST.

shows 2-m temperature and 10-m wind vector fields at 0300, 0800, 1000, 1400, 1800, and 2000 LST. Figure 6.9 (Figure 6.10) shows the vertical cross-sections of temperature and wind vector along the north-south direction (along the east-west direction) at $x = 0$ km (at $y = 0$ km) at times same as in Fig. 6.8.

At 0300 LST, the temperature in the urban area is higher than that in its surrounding valley areas, exhibiting an urban heat island phenomenon (Fig. 6.8a). Weak mountain downslope winds and weak down-valley winds are observed. Weak converging winds are present in the urban area, which is largely due to the urban heat island-induced flow, that is, the urban breeze (Fig. 6.8a). Down-valley winds up to $z \sim 250$ m above the surface blow down the valley (easterly), featuring channeling winds (Fig. 6.10a). Above $z \sim 250$ m, the daytime residual layer is lifted, exhibiting a two-layered wind structure within the temperature inversion layer in the nighttime (Fig. 6.10a). The layered structure of the nocturnal boundary layer with a low stable layer and a residual layer aloft was identified in observations and model simulations (Derbyshire 1994). Winds in the temperature inversion layer seem to be to some extent decoupled from stronger upper-level southerly winds (Fig. 6.9a). This is consistent with the results of Whiteman and McKee (1977). At 0800 LST, the temperature inversion layer is still deep in the urban area (Figs. 6.9b, 6.10b) and near-surface down-valley winds

weaken or disappear (Fig. 6.8b). The layered wind structure does not exist at 0800 LST (Fig. 6.10b). At 1000 LST, up-valley winds form (Figs. 6.8c, 6.10c). The temperature inversion bottom in the urban area slightly rises up, and winds are stronger in the urban area below the temperature inversion bottom than in the surrounding valley floor (Figs. 6.9c, 6.10c). At 1400 LST, in the urban area the temperature inversion bottom further rises up, exhibiting an elevated temperature inversion layer and up-valley winds strengthen (Figs. 6.8d, 6.9d, 6.10d). Near-surface winds weaken east of the city due to the counteracting urban breeze. At 1800 LST, mountain downslope winds develop, the temperature inversion bottom in the urban area descends, and winds below the temperature inversion bottom weaken (Figs. 6.8e, 6.9e, 6.10e). At 2000 LST, mountain downslope winds and down-valley winds become stronger (Figs. 6.8f).

To examine urban effects on local circulations in the presence of temperature inversion, an experiment is conducted in which the urban area is replaced by the grassland land-use type (called the no-urban simulation) and the results are compared to those of the simulation with the urban area (called the control simulation). Figure 6.11 shows the fields of the thickness and strength of temperature inversion layer at 1400 LST in the no-urban simulation. In Ulaanbaatar, the thickness of temperature inversion layer is

smaller and its intensity is weaker in the control simulation than in the no-urban simulation (Figs. 6.6c,g, 6.11a,b), clearly showing urban effects on

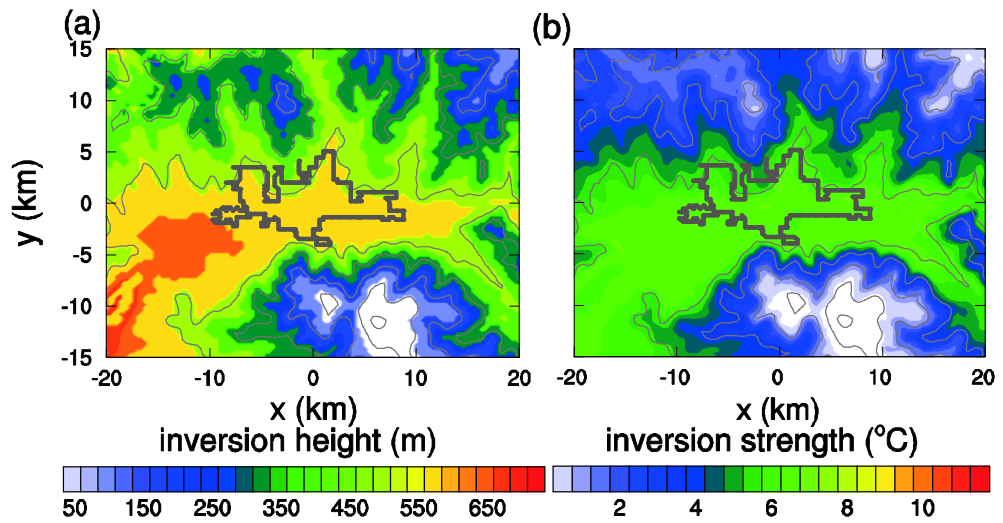


Figure 6.11. (a) Thickness and (b) strength of inversion layer at 1400 LST in the no-urban simulation.

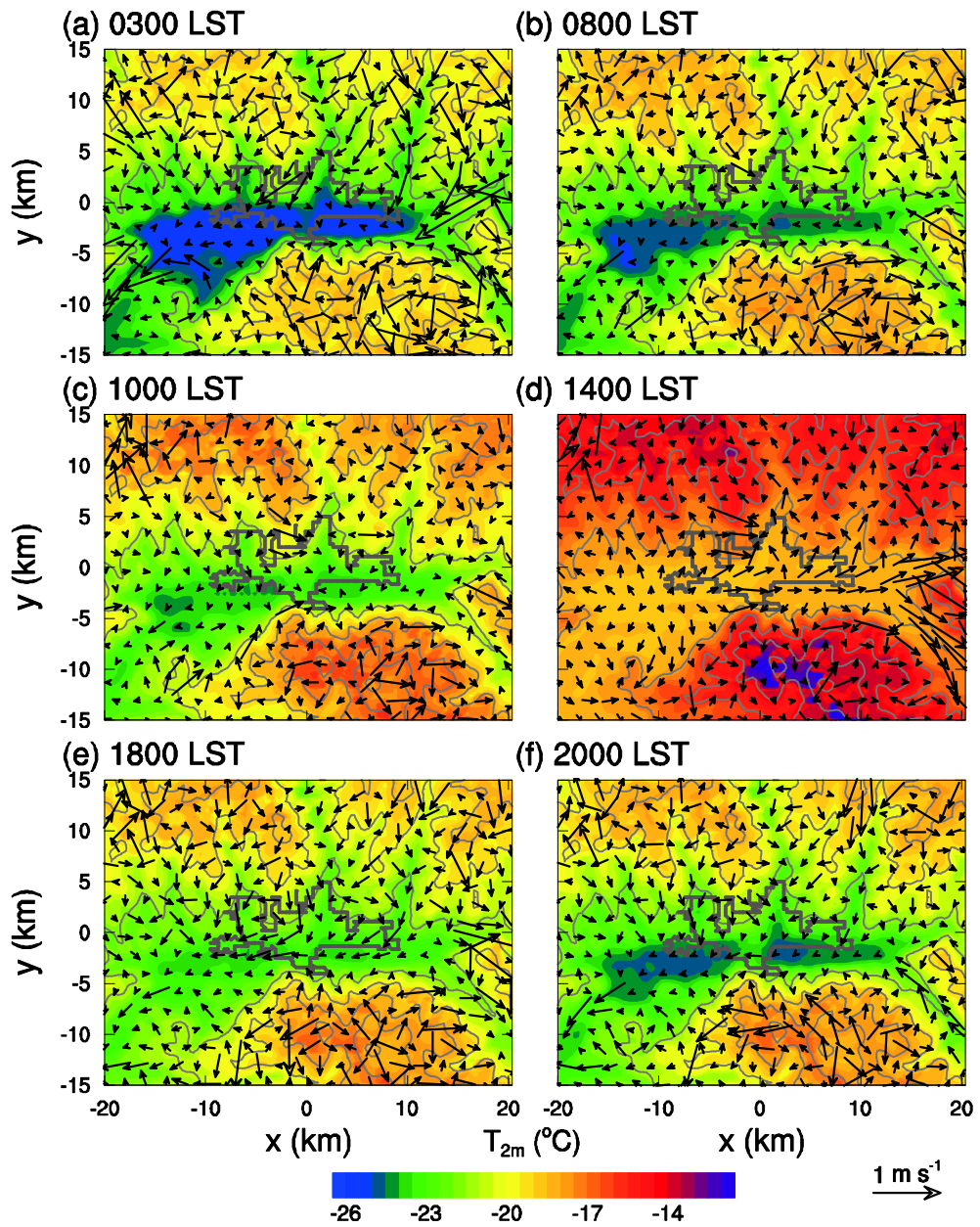


Figure 6.12. Same as in Fig. 6.8 but for the simulation with the urban area being replaced by the grassland land-use type.

temperature inversion layer. Figure 6.12 shows the fields of 2-m temperature and 10-m wind vector at 0300, 0800, 1000, 1400, 1800, and 2000 LST in the no-urban simulation. At 0300 and 0800 LST, the temperature difference between the control and no-urban simulations in the urban area is large. The temperature difference is up to 5.0°C at 0300 LST and 4.4°C at 0800 LST. At 0300 and 0800 LST, down-valley winds in the main valley region are slightly stronger in the control simulation than in the no-urban simulation (Figs. 6.8a,b, 6.12a,b). At 1000 LST, weak converging winds are present in and east of Ulaanbaatar in the control simulation (Fig. 6.8c), but these are almost absent in the no-urban simulation (Fig. 6.12c). At 1400 LST, up-valley winds in Ulaanbaatar are stronger in the control simulation than in the no-urban simulation (Figs. 6.8d, 6.12d). At 1800 LST, in Ulaanbaatar, up-valley winds are still present in the control simulation, while down-valley winds already develop in the no-urban simulation (Figs. 6.8e, 6.12e). At 2000 LST, winds in Ulaanbaatar are slightly stronger in the control simulation than in the no-urban simulation (Figs. 6.8f, 6.12f).

The simulated wintertime local circulations in and around the Ulaanbaatar metropolitan area are weaker than the summertime local circulations examined in the previous section. This is attributed to the presence of temperature inversion and smaller surface sensible heat flux. Although the simulated wintertime local winds/circulations are weaker,

urban breezes, mountain slope winds, and up-/down-valley winds develop well and the interactions of urban breezes with up-/down-valley winds occur clearly.

7 Summary and conclusions

This study employs numerical modeling and theoretical approaches to investigate the local circulations in the mountainous urban areas.

The characteristics of the Ulaanbaatar UHI were for the first time documented using surface meteorological data for the 31-year period 1980–2010. Ulaanbaatar is a high-altitude metropolitan city located in a valley. The analysis concentrated on the temporal patterns of the UHI intensity. The UHI intensity was evaluated by investigating the data from two meteorological stations. The average UHI intensity for the period was found to be 1.6°C. The UHI intensity shows seasonal variations, being strongest in winter (3.3°C) and weakest in summer (0.3°C). The average daily maximum UHI intensity was found to be 4.3°C. The strongest daily maximum UHI intensity occurs in winter with an average intensity of 6.4°C, and the weakest daily maximum UHI intensity occurs in summer with an average intensity of 2.5°C. The occurrence frequency of the daily maximum UHI intensity in the nighttime is 5.6 times that in the daytime. These UHI features for Ulaanbaatar are qualitatively similar to UHI characteristics in many other cities around the world. The Ulaanbaatar UHI in winter, however, appears to be strong compared to the UHI in other cities (e.g., Seoul). This can be attributed to the peculiar geographical features of

Ulaanbaatar, wintertime weather that is strongly influenced by Siberian high, and anthropogenic heat resulting from the burning of coal and wood.

The relative importance of meteorological parameters that affect the daily maximum UHI intensity was examined through a multiple linear regression analysis. The parameters considered are the previous-day maximum UHI intensity, wind speed, cloudiness, and relative humidity. For all data, the multiple linear regression model explains half of the variance (49.8%). The previous-day maximum UHI intensity was found to be the most important parameter, showing a positive correlation with the daily maximum UHI intensity. Cloudiness is the second most important parameter showing a negative correlation with the daily maximum UHI intensity. It was shown that the relative importance of the four meteorological parameters changes when the data are classified into daytime/nighttime and season. Cloudiness is the most important parameter in spring and summer, but the previous-day maximum UHI intensity is the most important parameter in autumn and winter.

Interactions between urban breeze circulation and mountain slope winds were examined in two dimensions using the WRF model coupled with an advanced urban canopy model. Circulation over the urban area is characterized by the weakened mountain-side urban wind owing to the opposing upslope wind and the strengthened plain-side urban wind in the

daytime. The transition from upslope wind to downslope wind on the urban-side slope starts earlier than that in a simulation that includes only an isolated mountain (1430 and 1845 LST, respectively). A hydraulic jump is observed in the late afternoon and stagnates until late evening.

Extensive experiments were conducted to examine the sensitivities of the interactions of urban breeze circulation with mountain slope winds and urban heat island intensity to mountain height and urban fraction. Through the sensitivity experiments, it was found that the transition from urban-side upslope wind to downslope wind starts earlier (from 1125 LST) and that the urban-side downslope wind persists longer (up to 85%) with decreasing mountain height and increasing urban fraction. The change in transition time from upslope wind to downslope wind affects interactions between urban breeze circulation and mountain slope winds. The horizontal wind near the urban–rural edge becomes stronger as the mountain height increases and the urban fraction increases (from 0.4 to 2.1 m s⁻¹). Urban heat island intensity was found to be more sensitive to urban fraction than to mountain height. An increase in urban fraction by every 0.1 results in average increases of 0.17 and 1.27°C in the daytime and nighttime urban heat island intensities, respectively.

A case in which a city is located in a basin between two identical mountains was examined. The urban-side downslope wind develops earlier

(around 1400 LST at the urban-side mid-slope location) and persists longer than the rural-side downslope wind and the plain-to-basin wind is stronger than in the simulation that includes a city and an isolated mountain. The hydraulic jumps also occur in this case.

Interactions of urban breeze circulation with mountain slope winds were theoretically investigated in the context of the response of the atmosphere to specified thermal forcing. Linear, theoretical calculations showed that in the daytime low-level converging flows induced by urban heating (urban breeze) and those induced by mountain heating (upslope winds) effectively interfere with each other in the region between the urban center and the mountain center. Thus, flows are weakened in the mountain-side urban area and on the urban-side mountain slope and converging flows are intensified in the plain-side urban area and on the rural-side mountain slope. An earlier transition from the upslope wind to downslope wind on the urban-side mountain slope takes place when compared with the case of mountain thermal forcing only. Thus, the occurrence frequency of downslope wind becomes larger in comparison with the case that includes mountain thermal forcing only. Linear, theoretical calculations showed that in the nighttime strong flows appear in the region between the urban center and the mountain center due to the additive interaction between the downslope wind and the urban breeze. In the nighttime, weakened

converging flows appear on the plain-side urban area and weakened downslope wind appears on the rural-side mountain slope.

Sensitivity tests were conducted to examine the dependences of the urban and mountain thermal forcing intensities on the interactions between urban breeze circulation and mountain slope winds. The results showed that the degree of the interactions of urban breeze circulation with mountain slope winds is dependent on the intensities of urban and mountain thermal forcings.

Local circulations in and around the Ulaanbaatar, Mongolia, metropolitan area were investigated for the first time through numerical simulations using a high-resolution mesoscale model coupled with the advanced urban canopy model (WRF-SNUUCM) under idealized summertime fair-weather conditions with no synoptic winds. In the daytime, local circulations are characterized by upslope and up-valley winds and urban breeze circulation. It was found that mountain upslope winds precede up-valley winds and that upslope winds change to downslope winds on the urban-side slope of Mt. Bogd Khan and the downslope winds in the afternoon strengthen due to urban breezes. In the nighttime, local circulations are characterized by mountain downslope winds and down-valley winds. Strong channeling flows appear over the city.

Experiments were conducted to examine sensitivities of the local circulations to the urban fraction, atmospheric stability, and soil water content. As urban fraction increases, daytime up-valley winds over the city and daytime downslope winds on the urban-side slope of Mt. Bogd Khan strengthen. As atmospheric stability increases, daytime up-valley winds become more consistently directed in the along-valley direction and daytime cross-valley winds tend to weaken. Near-surface up-valley winds in the city strengthen with increasing atmospheric stability. As soil water content decreases, downslope winds on the urban-side upper slope of Mt. Bogd Khan weaken while downslope winds on the urban-side lower slope of Mt. Bogd Khan strengthen. As soil water content decreases, daytime near-surface up-valley winds in the city weaken.

Wintertime local circulations in the presence of temperature inversion in and around Ulaanbaatar were studied using the WRF-SNUUCM. Simulation results were compared with observed data. The thickness and strength of temperature inversion layer were found to be associated with the terrain. The persistent temperature inversion layer is deep in the valleys and shallow over the mountain slopes. Local circulations, which include urban breezes, mountain slope winds, and up- and down-valley winds, were found to be weak in the presence of temperature inversion. In the daytime, mountain upslope winds are weak, up-valley winds strengthen in the urban

area, and near-surface winds east of the city are weak. As the temperature inversion bottom rises up in the urban area, winds below the temperature inversion bottom strengthen. In the nighttime, downslope winds and down-valley winds develop. Above the layer with down-valley winds, the daytime residual layer is lifted, featuring a two-layer wind structure.

Urban effects on local circulations in the presence of temperature inversion were examined. In the daytime, the temperature inversion layer becomes shallower and weaker in Ulaanbaatar in the control simulation than the no-urban simulation. The absence of urban breezes in the no-urban simulation results in weaker up-valley winds in the main valley and stronger up-valley winds east of the city than in the control simulation. Down-valley winds in the main valley starts earlier in the no-urban simulation.

The findings of this study would advance our understanding of local circulations in mountainous urban areas, particularly, local circulations in and around Ulaanbaatar, Mongolia.

References

- Amarsaikhan, D., M. Ganzorig, H. H. Blotevogel, B. Nergui, and R. Gantuya, 2009: Integrated method to extract information from high and very high resolution RS images for urban planning. *J. Geogr. Reg. Plann.*, **2**, 258–267.
- Arino, O., J. Ramos, V. Kalogirou, P. Defourny, and F. Achard, 2010: GlobCover 2009. *Proceeding ESA Living Planet Symp.*, Bergen, Norway, ESA, SP-686.
- Bader, D. C., and T. B. McKee, 1985: Effects of shear, stability and valley characteristics on the destruction of temperature inversions. *J. Climatol. Appl. Meteor.*, **24**, 822–832.
- Baik, J.-J. 1992: Response of a stably stratified atmosphere to low-level heating—An application to the heat island problem. *J. Appl. Meteor.*, **31**, 291–303.
- Baik, J.-J., Y.-H. Kim, J.-J. Kim, and J.-Y. Han, 2007: Effects of boundary-layer stability on urban heat island-induced circulation. *Theor. Appl. Climatol.*, **89**, 73–81.
- Banta, R. M., L. Mahrt, D. Vickers, J. Sun, B. B. Balsley, Y. Pichugina, and J. Williams, 2007: The very stable boundary layer on nights with weak low-level jets. *J. Atmos. Sci.*, **64**, 3068–3090.

- Chen, F., and J. Dudhia, 2001: Coupling an advanced land surface–hydrology model with the Penn State–NCAR MM5 modeling system. Part I: Model implementation and sensitivity. *Mon. Wea. Rev.*, **129**, 569–585.
- Chen, S.-H., and W.-Y. Sun, 2002: A one-dimensional time dependent cloud model. *J. Meteor. Soc. Japan*, **80**, 99–118.
- Chen, X., J. A. Anel, A. Su, L. de la Torre, H. Kelder, J. van Peet, and Y. Ma, 2013: The deep atmospheric boundary layer and its significance to the stratosphere and troposphere exchange over the Tibetan Plateau. *PLoS ONE* **8(2)**: e56909. doi: 10.1371/journal.pone.0056909.
- de Wekker, S. F. J., S. Zhong, J. D. Fast, and C. D. Whiteman, 1998: A numerical study of the thermally driven plain-to-basin wind over idealized basin topographies. *J. Appl. Meteor.*, **37**, 606–622.
- Defant, F., 1951: Local winds. *Compendium of meteorology*. American Meteor. Soc., 655–672.
- Derbyshire, S. H., 1995: Stable boundary layers: observations, models and variability Part II: data analysis and averaging effects. *Bound.-Layer Meteor.*, **75**, 1–24.

- Dudhia, J., 1989: Numerical study of convection observed during the winter monsoon experiment using a mesoscale two-dimensional model. *J. Atmos. Sci.*, **46**, 3077–3107.
- Fan, H., and D. J. Sailor, 2005: Modeling the impacts of anthropogenic heating on the urban climate of Philadelphia: a comparison of implementations in two PBL schemes. *Atmos. Environ.*, **39**, 73–84.
- Fernando, H. J. S., 2010: Fluid dynamics of urban atmospheres in complex terrain. *Annu. Rev. Fluid. Mech.*, **42**, 365–389.
- Figuerola, P. I., and N. A. Mazzeo, 1998: Urban–rural temperature differences in Buenos Aires. *Int. J. Climatol.*, **18**, 1709–1723.
- Friedl, M. A., D. K. McIver, J. C. F. Hodges, X. Y. Zhang, D. Muchoney, A. H. Strahler, C. E. Woodcock, S. Gopal, A. Schnieder, A. Cooper, A. Bacinni, F. Gao, and C. Schaaf, 2002: Global land cover mapping from MODIS: algorithms and early results. *Remote Sens. Environ.*, **83**, 287–302.
- Gerelchuluun, B., and J.-B. Ahn, 2014: Air temperature distribution over Mongolia using dynamical downscaling and statistical correction. *Int. J. Climatol.*, **34**, 2464–2476.
- Giovannini, L., D. Zardi, and M. De Franceschi, 2011: Analysis of the urban thermal fingerprint of the city of Trento in the Alps. *J. Appl. Meteor. Climatol.*, **50**, 1145–1162.

- Giovannini, L., D. Zardi, M. De Franceschi, and F. Chen, 2014: Numerical simulations of boundary-layer processes and urban-induced alterations in an Alpine valley. *Int. J. Climatol.*, **34**, 1111–1131.
- Goldreich, Y., 1984: Urban topoclimatology. *Prog. Phys. Geog.*, **8**, 336–364.
- Google Inc., 2011: Google Earth. <http://maps.google.com>.
- Grimmond, C. S. B., and Coauthors, 2010: The international urban energy balance models comparison project: First results from phase 1. *J. Appl. Meteor. Climatol.*, **49**, 1268–1292.
- Han, J.-Y., and J.-J. Baik, 2008: A theoretical and numerical study of urban heat island–induced circulation and convection. *J. Atmos. Sci.*, **65**, 1859–1877.
- Hidalgo, J., V. Masson, and G. Pigeon, 2008a: Urban-breeze circulation during the CAPITOUL experiment: Numerical simulations. *Meteor. Atmos. Phys.*, **102**, 243–262.
- Hidalgo, J., G. Pigeon, and V. Masson, 2008b: Urban-breeze circulation during the CAPITOUL experiment: Observational data analysis approach. *Meteor. Atmos. Phys.*, **102**, 223–241.
- Hidalgo, J., V. Masson, and L. Gimeno, 2010: Scaling the daytime urban heat island and urban breeze circulation. *J. Appl. Meteor. Climatol.*, **49**, 889–901.

- Hinkel, K. M., F. E. Nelson, A. E. Klene, and J. H. Bell, 2003: The urban heat island in winter at Barrow, Alaska. *Int. J. Climatol.*, **23**, 1889–1905.
- Hong, S.-Y., Y. Noh, and J. Dudhia, 2006: A new vertical diffusion package with an explicit treatment of entrainment processes. *Mon. Wea. Rev.*, **134**, 2318–2341.
- Jarvis, A., H. I. Reuter, A. Nelson, and E. Guevara, 2008: Hole-filled SRTM for the globe version 4. <http://srtm.csi.cgiar.org>.
- Jauregui, E., L. Godinez, and F. Cruz, 1992: Aspects of heat-island development in Guadalajara, Mexico. *Atmos. Environ.*, **26**, 391–396.
- Kim, Y.-H., and J.-J. Baik, 2002: Maximum urban heat island intensity in Seoul. *J. Appl. Meteor.*, **41**, 651–659.
- Kim, Y.-H., and J.-J. Baik, 2004: Daily maximum urban heat island intensity in large cities of Korea. *Theor. Appl. Climatol.*, **79**, 151–164.
- Kimura, F., and T. Kuwagata, 1993: Thermally induced wind passing from plain to basin over a mountain range. *J. Appl. Meteor.*, **32**, 1538–1547.
- Kimura, F., and T. Kuwagata, 1995: Horizontal heat fluxes over complex terrain computed using a simple mixed-layer model and a numerical model. *J. Appl. Meteor.*, **34**, 549–558.

- Kirshbaum, D. J., 2013: On thermally forced circulations over heated terrain. *J. Atmos. Sci.*, **70**, 1690–1709.
- Kottek, M., J. Grieser, C. Beck, B. Rudolf, and F. Rubel, 2006: World map of the Köppen-Geiger climate classification updated. *Meteor. Z.*, **15**, 259–263.
- Lee, S.-H., and H.-D. Kim, 2010: Modification of nocturnal drainage flow due to urban surface heat flux. *Asia-Pac. J. Atmos. Sci.*, **46**, 453–465.
- Lee, S.-H., and F. Kimura, 2001: Comparative studies in the local circulations induced by land-use and by topography. *Bound.-Layer Meteor.*, **101**, 157–182.
- Lee, S.-H., and J.-J. Baik, 2010: Statistical and dynamical characteristics of the urban heat island intensity in Seoul. *Theor. Appl. Climatol.*, **100**, 227–237.
- Lemonsu, A., and V. Masson, 2002: Simulation of a summer urban-breeze over Paris. *Bound.-Layer Meteor.*, **104**, 463–490.
- Lin, Y. L., and R. B. Smith, 1986: Transient dynamics of airflow near a local heat source. *J. Atmos. Sci.*, **43**, 40–49.
- Liu, W., C. Ji, J. Zhong, X. Jiang, and Z. Zheng, 2007: Temporal characteristics of the Beijing urban heat island. *Theor. Appl. Climatol.*, **87**, 213–221.

- Ma, M., Z. Pu, S. Wang, and Q. Zhang, 2011: Characteristics and numerical simulations of extremely large atmospheric boundary-layer heights over an arid region in north-west China. *Bound.-Layer Meteor.*, **140**, 163–176.
- Magee, N., J. Curtis, and G. Wendler, 1999: The urban heat island effect at Fairbanks, Alaska. *Theor. Appl. Climatol.*, **64**, 39–47.
- Mahrt, L., and D. Vickers, 2006: Contrasting vertical structures of nocturnal boundary layers. *Bound.-Layer Meteor.*, **105**, 351–365.
- Martilli, A., 2003: A two-dimensional numerical study of the impact of a city on atmospheric circulation and pollutant dispersion in a coastal environment. *Bound.-Layer Meteor.*, **108**, 91–119.
- Mlawer, E. J., S. J. Taubman, P. D. Brown, M. J. Iacono, and S. A. Clough, 1997: Radiative transfer for inhomogeneous atmospheres: RRTM, a validated correlated-k model for the longwave. *J. Geophys. Res.*, **102**, 16663–16683.
- Montávez, J. P., A. Rodríguez, and J. I. Jiménez, 2000: A study of the urban heat island of Granada. *Int. J. Climatol.*, **20**, 899–911.
- Morris, C. J. G., I. Simmonds, and N. Plummer, 2001: Quantification of the influences of wind and cloud on the nocturnal urban heat island of a large city. *J. Appl. Meteor.*, **40**, 169–182.

- Ohashi, Y., and H. Kida, 2002: Effects of mountains and urban areas on daytime local-circulations in the Osaka and Kyoto regions. *J. Meteor. Soc. Japan*, **80**, 539–560.
- Oke, T. R., 1982: The energetic basis of the urban heat island. *Quart. J. Roy. Meteor. Soc.*, **108**, 1–24.
- Oke, T. R., 1987: *Boundary Layer Climates*. 2nd ed. Routledge, 435 pp.
- Olfe, D. B., and R. L. Lee, 1971: Linearized calculations of urban heat island convection effects. *J. Atmos. Sci.*, **28**, 1374–1388.
- Palfy, E., 1995: Temperature inversion in the Csik basin. *Acta Climatol.*, **28–29**, 41–45.
- Pielke, R. A., 2002: *Mesoscale meteorological modeling*. 2nd ed. Academic Press, San Diego, 676 pp.
- Richiardone, R., and G. Brusasca, 1989: Numerical experiments on urban heat island intensity. *Quart. J. Roy. Meteor. Soc.*, **115**, 983–995.
- Ryu, Y.-H., J.-J. Baik, and S.-H. Lee, 2011: A new single-layer urban canopy model for use in mesoscale atmospheric models. *J. Appl. Meteor. Climatol.*, **50**, 1773–1794.
- Ryu, Y.-H., and J.-J. Baik, 2012: Quantitative analysis of factors contributing to urban heat island intensity. *J. Appl. Meteor. Climatol.*, **51**, 842–854.

- Ryu, Y.-H., and J.-J. Baik, 2013a: Daytime local circulations and their interactions in the Seoul metropolitan area. *J. Appl. Meteor. Climatol.*, **52**, 784–801.
- Ryu, Y.-H., J.-J. Baik, and J.-Y. Han, 2013b: Daytime urban breeze circulation and its interaction with convective cells. *Quart. J. Roy. Meteor. Soc.*, **139**, 401–413.
- Savijarvi, H., and J. Liya, 2001: Local winds in a valley city. *Bound.-Layer Meteor.*, **100**, 301–319.
- Simpson, J. E., 1994: *Sea breeze and local winds*. Cambridge University Press, New York, 234 pp.
- Skamarock, W. C., J. B. Klemp, J. Dudhia, D.O. Gill, D. M. Barker, M. G. Duda, X. Y. Huang, W. Wang, and J. G. Powers, 2008: A description of the advanced research WRF version 3. NCAR, Boulder.
- Taha, H., 1997: Urban climates and heat islands: albedo, evapotranspiration, and anthropogenic heat. *Energ. Build.*, **25**, 99–103.
- Unger, J., 1996: Heat island intensity with different meteorological conditions in a medium-sized town: Szeged, Hungary. *Theor. Appl. Climatol.*, **54**, 147–151.
- Unwin, D. J., 1980: The synoptic climatology of Birmingham's urban heat island, 1965–74. *Weather*, **35**, 43–50.

- Vukovich, F. M., and J. W. Dunn, 1978: A theoretical study of the St. Louis heat island: Some parameter variations. *J. Appl. Meteor.*, **17**, 1585–1594.
- Whiteman, C. D., 1990: Observations of thermally developed wind systems in mountainous terrain. Atmospheric processes over complex terrain. *Meteor. Monogr.* **45**, 5–42.
- Whiteman, C. D., 2000: *Mountain Meteorology: Fundamentals and applications*. Oxford, 376 pp.
- Whiteman, C. D., 1982: Breakup of temperature inversions in deep mountain valleys. Part I: observations. *J. Appl. Meteor.*, **21**, 270–289.
- Wong, K. K., and R. A. Dirks, 1978: Mesoscale perturbations on airflow in the urban mixing layer. *J. Appl. Meteor.*, **17**, 677–688.
- Zhang, N., X. Wang, and Z. Peng, 2014: Large-eddy simulation of mesoscale circulations forced in inhomogeneous urban heat island. *Bound.-Layer Meteor.*, **151**, 179–194.

초 록

산악 도시 지역의 국지 순환, 국지 순환간의 상호작용, 몇 가지 환경 요소에의 의존성을 수치적, 이론적인 접근을 통해 연구하였다. 또한 산악 도시 지역의 대기오염에 중요한 고려 요소인 온도 역전층의 존재에 따른 국지 순환을 연구하였다.

몽골 울란바토르 지역의 도시열섬 강도 특성을 1980-2010 년의 31 년 간 도시와 교외 두 지점에서 측정된 자료를 이용하여 분석하였다. 도시열섬 강도와 그 최대값을 연구했으며, 도시열섬 강도의 일간, 월간, 계절간, 연간 특성을 조사하였다. 분석 결과에 따르면 도시열섬 강도는 겨울철(야간)에 강하고 여름철(주간)에 약한 큰 계절적 의존성을 보였다. 일 최대 도시열섬 강도는 여름철에 비해 겨울철에 강했으며 주로 야간에 나타났다. 다중 회기 분석을 통해 일 최대 도시열섬 강도에 미치는 다양한 대기 요소(전일 최대 도시열섬 강도, 풍속, 운량, 상대 습도)의 상대적 중요도를 밝혔다. 그 결과, 전일 최대 도시열섬 강도가 가장 중요한 요소였으며 일 최대 도시열섬 강도와 양의 상관관계를 가졌다.

서울대학교 도시 캐노피 모형(SNUUCM)이 결합된 중규모 기상 모형(WRF 모형)을 이용하여 2 차원 상에서 도시풍 순환과 산곡풍간의 상호작용을 연구하였다. 배경류가 없으며 고립된 산악 근처에 위치한 도시를 고려하였다. 도시 지역의 순환은 비대칭적이며 주간(주간)의 산악 활승류에 의해 산악측 도시풍이 약화되며 평지측 도시풍이 강화되는 특징을 보였다. 도시측 산사면 위에서 활승류에서 활강류로의 전이는 고립된 산악만을 고려한 실험에 비해 일찍 나타났다. 늦은 오후 강한 활강류가 약한 산악측 도시풍을 만나며 물뿔 현상이 나타났으며 이 현상은 늦은 저녁까지 정체되었다. 산악의 높이와 도시 비율에 따른 도시풍과 산곡풍의 상호작용과 도시열섬 강도의 민감도 실험을 수행하였다. 산악의 높이가 낮고 도시 비율이 클수록 도시측 산사면 위에서 활승류에서 활강류로의 전이가 일찍 일어났으며 도시측 활강류가 오랜 시간 지속되었다. 도시측 산사면 위에서 활승류에서 활강류로의 전이 시각의 변화는 도시풍 순환과 산곡풍의 상호작용 변화를 야기한다. 도시열섬 강도는 산악의 높이보다 도시 비율에 더 민감하였다. 주간(야간) 도시열섬 강도는 도시 비율이 0.1 증가할 때마다 0.17°C (1.27°C) 상승하였다. 도시가 분지에 위치할 때의 실험을 수행하였으며, 그 결과 고립된 산악을 고려한 실험에 비해 도시측 산사면의 활강류가 일찍 나타나

오래 지속되며 평지에서 분지로의 바람이 강하게 나타남을 확인하였다.

열적 강제에 의한 대기의 반응을 통하여 도시풍 순환과 산곡풍의 상호작용을 이론적으로 분석하였다. 선형화된 2 차원 지배 방정식에서 출발하여 섭동 연직속도, 수평속도, 부력, 운동학적 압력을 해석적으로 구하였으며 구한 해석해를 이용하여 상호작용을 분석했다. 도시풍 순환과 산곡풍은 각각 시간에 따라 일정하거나 일 주기로 변화하는 열적 강제에 의해 발달하며 서로 선형적 상호작용을 한다. 그 결과 비대칭적 흐름이 도시 및 산악 지역에 발달하였다. 주간에는 도시 및 산악 가열에 의해 유도된 하층 수렴류(도시풍 및 활승류)가 서로 효과적으로 간섭하여 산악측 도시 및 도시측 산사면의 바람을 약화시켰다. 산악의 열적 강제만이 존재하는 경우에 비해 도시측 산사면 위에서 활승류에서 활강류로의 전이가 일찍 일어났으며 활강류가 오래 지속되었다. 야간에는 도시풍과 활강류의 상호작용에 의해 강한 도시와 산악 중심 사이의 흐름이 유도되었으나 야간에 도시열섬이 약화됨에 따라 그 강도는 시간에 따라 약해졌다. 야간에 교외측 산사면의 활강류와 평지측 도시면의 수렴류는 약화됨을 확인하였다. 도시 및 산악의 열적 강도에 따른 도시풍 순환과 산곡풍의 상호작용의 민감도 실험을 수행하였다. 그 결과

주간 및 야간 모두 도시풍 순환과 산곡풍의 상호작용 정도가 두 열적 강제에 강도에 의존함을 확인하였다.

서울대학교 도시 캐노피 모형(SNUUCM)이 결합된 중규모 기상 모형(WRF 모형)을 이용하여 몽골 울란바토르 주변의 국지 순환을 수치적으로 분석하였다. 종관적 흐름이 없는 이상적인 여름철 맑은 날씨 조건을 사용하여 3 차원 모의 실험을 수행하였다. 주간에는 산악 활승류, 곡풍, 도시풍 순환이 나타나 서로 상호작용하였다. 산악 활승류가 곡풍에 비해 먼저 나타남을 확인하였다. 오후에는 도시측 북드항 산사면 위에서 활승류에서 활강류로의 전이가 일어나며 도시풍에 의해 활강류가 강화됨을 알 수 있었다. 야간에는 산악 활강류와 산풍이 두드러지며 도시 지역에서 강한 채널링 흐름이 생성되었다. 도시 비율, 대기 안정도, 토양 수분 함량에 따른 국지 순환의 민감도 실험을 수행하였다. 도시 비율이 증가하면 주간의 도시 지역 곡풍과 도시측 북드항 산사면 위의 활강류가 강화되었다. 대기 안정도가 증가할수록 주간에 도시 지역의 지표면 근처 곡풍이 강화되었다. 반면 토양 수분 함량이 감소함에 따라 주간에 도시 지역의 지표면 근처 곡풍이 약화되었다. 주간 도시 대기 경계층 높이는 대기 안정도와 토양 수분 함량에 민감함을 알 수

있었다. 본 연구는 울란바토르와 주변의 국지 순환 및 도시가 산곡풍 및 산사면 활승/활강류에 미치는 영향을 처음으로 분석하였다.

WRF-SNUUCM 모형을 이용하여 온도 역전층이 존재할 때 울란바토르 주변의 겨울철 국지 순환을 분석하였다. 수치 모의된 지표면 근처 기온과 바람을 관측 결과를 이용하여 검증하였다. 시베리아 고기압의 영향을 받아 약한 종관풍이 불며 온도 역전층이 존재하는 맑은 겨울철 날씨를 고려하였다. 온도 역전층의 깊이와 강도가 지형과 밀접한 관련이 있음을 밝혔다. 산사면에 비해 골짜기에서 온도 역전층이 깊고 강하였으며 대체로 역전층 꼭대기 고도는 주변 최대 산마루 고도보다 낮았으나 경계층 꼭대기 고도 보다는 높게 나타났다. 온도 역전층이 존재할 때 약한 국지 순환이 발달되었다. 주간에는 약한 산악 활승류가 발달하며 곡풍이 주변 지역보다 도시 지역에서 강하게 발달하였다. 또한 채널링 흐름이 좁은 골짜기에서 발달하였다. 온도 역전층 바닥면이 도시 지역에서 점차 상승하며 온도 역전층 바닥면 아래의 바람이 점차 강하게 나타났다. 야간에는 상승한 주간 잔여층의 존재하에 산악 활강류와 산풍이 발달하였다. 도시의 유무에 따른 두 실험을 통해 온도 역전층이 존재할 때의 도시 효과를 알아보았다. 그 결과 도시가 주간에 온도 역전층 바닥면을 상승시키며 역전층 강도를 약화하는

역할을 함을 알 수 있었다. 도시가 없는 실험에 비해 도시를 고려한 실험에서 오후에 도시 동쪽의 바람이 약화되며 산풍이 늦게 발달하였으며 이는 도시풍과 곡풍의 상호작용에 의한 결과이다.

주요어: 국지 순환, 도시열섬, 도시풍 순환, 산곡풍, 대기 모델링, 도시 캐노피 모형, 울란바토르, 몽골

학번: 2010-30765